Master's thesis

NTNU
Norwegian University of Science and Technology
Faculty of Natural Sciences
Department of Physics

Even Aksnes Tønseth

Antiferromagnetic Neuromorphic Computing

Master's thesis in Applied Physics and Mathematics
Supervisor: Alireza Qaiumzadeh
June 2022

NTNU
Norwegian University of
Science and Technology

Even Aksnes Tønseth

Antiferromagnetic Neuromorphic Computing

Master's thesis in Applied Physics and Mathematics
Supervisor: Alireza Qaiumzadeh
June 2022

Norwegian University of Science and Technology
Faculty of Natural Sciences
Department of Physics

NTNU
Norwegian University of
Science and Technology

Abstract

Neuromorphic computing is a field within computer science that uses brain-inspired components for computation and storage. When making these structures, one faces severe power and area limitations when using conventional computer technology. Therefore the field makes for an ideal arena for spintronics, spin-governed electronics with very low power usage. This thesis investigates how antiferromagnetic spintronics can be utilized in neuromorphic systems.

Currently, theoretical works implement such structures for ferromagnets, but the antiferromagnetic equivalent is less developed. A numerical and theoretical basis for such components is derived based on recent progress in the ferromagnetic counterpart. The derivation of the Landau-Lifshitz-Gilbert equation(LLG) is presented and used to calculate magnetization dynamics in antiferromagnetic systems numerically.

The structure incorporates temporal dependence of incoming signals, the synaptic region is tunable, and the neuronal structure holds the leaky integrate and fire property, all vital properties for building blocks in neuromorphic systems. All of these are found to be present in the numerical simulations of this thesis.

Synaptic plasticity is first modified with anisotropic effects before the possibility of tuning plasticity with magnetic fields, and STT is tested numerically. Magnetic field and anisotropic tuning seems most prudent after numerical tests.

It is also found that in biaxial antiferromagnets with homogeneous Dzyaloshinskii-Moriya interaction(DMI), when the interaction vector is along the hard-axis anisotropy, DMI severely alters the critical current where spiking occurs. Depending on the relative direction of polarization in the spin injector with the interaction vector, it either eases or staggers the critical current.

Antiferromagnetic nanoconstrictions proved to be possible building blocks for low-power neuromorphic computing. They show the underlying fundamental principles, and the spiking signals are tunable with multiple methods. It shows that these structures are possible for realizing neuromorphic computing experimentally.

Sammendrag

Nevromorf prosessering er et felt innen datavitenskap som har som mål å designe prosesseringsenheter med inspirasjon fra hjernedynamikk. Når en lager slike prosessorer med tradisjonell halvleder teknologi møter en store begrensinger innen strømforbruk og areal. Derfor er feltet en ideell arena for spintronikk, der logiske kretser bruker spinnet til elektronet fremfor ladningen. I denne masteroppgaven var målet å utforske hvordan antiferromagnetisk spintronikk kan inkorporeres i nevromorfe systemer.

Det finnes allerede teoretiske verker som implementerer slike komponenter i det ferromagnetiske tilfellet. Den antiferromagnetiske varianten er derimot mindre utviklet. Utledningen av Landau-Lifshitz-Gilbert likningen(LLG) er presentert før den blir tatt i bruk i to forskjellige systemer for antiferromagnetisk nevromorfe komponenter.

Dersom en skal lage en nevromorf struktur ved hjelp av antiferromagneter er det noen viktige grunnprinsipper som trenger å være til stede. Strukturen må inkorporere temporal avhengighet av innkommende signaler, den synaptiske plastisiteten må være justerbar, og det kunstige nevronet er nødt til å holde en lekkende integrerende effekt. Alle disse er funnet numerisk i strukturene som er undersøkt her.

Synaptisk plastisitet er først modifisert ved hjelp av anisotropiske effekter, før muligheten til å justere kunstig plastisitet ved magnetiske felt og spinn-dreiemoment er testet. Justering av synaptisk plastisitet virker å være mulig med disse teknikkene.

Disse effektene er undersøkt i biaksiale antiferromagneter med Dzyalishinskii-Moriya interaksjon (DMI), hvor interaksjonsvektoren er langs den harde aksen. Det ble funnet at DMI påvirker signalpropagering i stor grad når interaksjonsvektoren ligger langs den harde aksen. Dette vil enten senke eller heve terskelen for signal propagasjon når en induserer et spinn-dreiemoment i materialet.

Antiferromagnetiske nanoinnsnevringer ble funnet som mulige grunn komponenter i lav energi nevromorf prosessering. De innehar de underliggende prinsippene som trengs, og signal propagasjon er justerbar ved flere metoder. Disse komponentene kan være mulige kandidater for å realisere spintronisk nevromorf prosessering eksperimentelt.

Preface

This thesis is the final part of the five-year "sivilingeniør" program Applied Physics and Mathematics at the Norwegian University of Science and Technology written in the spring of 2022. It is a continuation of the specialization project written in the fall of 2021.

It presents a deep dive into the field of neuromorphic computing with antiferromagnetic spintronics, which is a complex and diverse field. It is in many ways a crossing of multiple genres of physics, from brain biology and network calculations to quantum mechanics. The work has, therefore, not only focused on quantum mechanics but also on discovering new fields in natural sciences.

I want to thank my supervisor Alireza Qaiumzadeh for his excellent support, despite a busy schedule. In addition, NTNU Nano fund for funding the making of the software program used in this thesis made by Viroshaan Uthayamoorthy and me from the fall of 2020 to the fall of 2021. I would also like to thank my parents, especially my mother, who passed away during the Christmas of 2021. Remembering her positivity and grit, even when she was terminally ill, was a true source of determination.

Even Aksnes Tønseth
Trondheim, Norway
June, 2022

Contents

Figures

Tables

1 Introduction

As early as 1965, Gordon Moore predicted that the number of transistors in computing devices would double every two years [1]. He predicted the observation to last for at least ten years. It proved, however, to last much longer. In recent years, the length scales of transistors have become so small that the observation by Moore is under content. The energy density and the fact that the length scale is nearing the small nm scale proves to be a problem. Therefore, the world of computer components needs innovation and more effective technologies. Spintronics could be the answer, as spintronic systems, in theory, can run at smaller power than regular semiconductor devices.

Antiferromagnets are materials where the net magnetization of the ground state is 0 and where spins are opposing in the lattice. Antiferromagnetism was viewed as an interesting theoretical concept without significant technological promise for a long time. They were viewed as hard to realize and manipulate. Louis Néel, Nobel Prize winner in physics and one of the people behind the discovery of antiferromagnets, even stated in his Nobel lecture that antiferromagnets "do not seem to have any applications" in 1970 [2]. Recent progress within the field of antiferromagnetic spintronics, where electronic components are built with antiferromagnetic components and the carrier of information is spin have been able to switch that perspective [3].

Antiferromagnetic spintronics has several advantages over ferromagnetic spintronics(where magnetic moments align). As mentioned, magnetic moments are aligned in regular patterns of opposing spins. The net magnetization is therefore 0. This means that antiferromagnets have no internal magnetic fields, which can give better stability and control when manipulating the material. Antiferromagnetic materials are also often insensitive to external fields [4]. In addition to the mentioned advantages, the resonance frequency of antiferromagnets is usually higher than that of their ferromagnetic counterparts. This could mean that antiferromagnet-based spintronics could exhibit faster clock frequencies than ferromagnet-based spintronics [5].

In this master thesis, the goal was to investigate how antiferromagnetic materials can be used within a field of computer science, neuromorphic computing. Neuromorphic computing represents a possible new architecture paradigm within computer hardware. The field attempts to do so by utilizing concepts from the most powerful computer we know, the brain. Using a brain-inspired computational paradigm, both the contention of Moore's law and the conventional computer's main bottleneck, the Von Neumann bottleneck, can be adressed by coalescing the location of memory and processing and reimagining how we do

computation entirely. It is, however, a complex challenge to overcome with conventional computer components, as they are inherently designed for binary computation. Therefore, new unconventional technologies such as spintronics might be more suited.

1.1 Outline

The master thesis first introduces the basis of antiferromagnetic spintronics in section 2 before neuromorphic computing is introduced in section 3. A concept for antiferromagnetic neuromorphic computation is introduced in section 4 based on a previous theoretical work. A second neuromorphic concept is introduced in section 6. Part I is a case study and based on the specialization project by myself in the fall of 2021, with some modifications for the thesis work.

Part I

Neuromorphic Computing with Topological Charges

2 Antiferromagnetic materials

As mentioned in the introduction, this thesis' primary focus is on the field of antiferromagnets. Understanding the dynamics of antiferromagnetic systems is needed to understand how they can be utilized in neuromorphic computing schemes. This section describes the free energy contributions of antiferromagnets and how the subsequent dynamics arise.

2.1 Free energy in antiferromagnets

Louis Néel first described antiferromagnetic dynamics in 1952 [6]. The initial description of the spin dynamics in the material was made by considering two sub-lattices, A and B, containing opposing spins. Different interaction terms in the Hamiltonian of the system described the dynamics of the two sublattices in a set of coupled equations. Here a brief overview of those terms is presented, and the Landau Lifziths Gilbert (LLG) equation is used to describe dynamics in an antiferromagnet. The equation of motion is found both from a phenomenological approach and the Lagrange formalism.

The energy interaction must first be understood to find the equations of motion in the antiferromagnetic material. The free energy functional enters the equation of motion in both approaches. This subsection presents the dominant energy contributions to the free energy before showing how those terms enter the equations of motion.

2.1.1 Exchange interaction

The exchange interaction is the Hamiltonian contribution which determines the magnetic ordering of the system(antiferromagnetic or ferromagnetic). It arises from the fermionic symmetry of the many-electron wave function in the material, $\Psi(\vec{r}_1, .., \vec{r}_n, s_1, ..., s_n)$ where $\vec{r}_i$ is the position of electron with spin s_i. To see why fermionic symmetry causes different types of magnetic ordering, it is prudent to look at a two-particle system of interacting hydrogen atoms, as it is the simplest form imaginable where this effect can occur. The following derivation is based on PC Hemmer's "Kvantemekanikk" [7].

If, for now, the electron-electron interaction of the two-particle system is ignored, the gathered Hamiltonian can be expressed as

$$\hat{\mathcal{H}} = \hat{\mathcal{H}}_1 + \hat{\mathcal{H}}_2 + \hat{\mathcal{H}}_C. \tag{2.1}$$

The subscript 1, 2 and C here denotes particle 1, particle 2 and their Coulomb interaction. The spatial wave function of this system can either be symmetric ψ_s or antisymmetric ψ_a when building the total wave function from the single-particle bases ψ_1 and ψ_2 [7]. This

produces either a symmetric function ψ_s or an antisymmetric function ψ_a. When ignoring the Coulomb correction to the spatial wave functions, ψ_1 and ψ_2, the total spatial functions can be written as [7]

$$\begin{aligned}\psi_a &= \frac{1}{\sqrt{2}}\Big(\psi_1(\vec{r}_1)\psi_2(\vec{r}_2) - \psi_1(\vec{r}_1)\psi_2(\vec{r}_2)\Big)\\ \psi_s &= \frac{1}{\sqrt{2}}\Big(\psi_1(\vec{r}_1)\psi_2(\vec{r}_2) + \psi_1(\vec{r}_1)\psi_2(\vec{r}_2)\Big).\end{aligned} \tag{2.2}$$

From the fermionic symmetry requirement that the total wave function, $\Psi(\vec{r}_1, \vec{r}_2, s_1, s_2) = \psi(\vec{r}_1, \vec{r}_2)\chi(s_1, s_2)$ has to be antisymmetric in terms of switching particle indices, the spin state of the wave function has to be either antisymmetric or symmetric to ensure total antisymmetry. When combining two half-integer spins, the resulting spin state has either total spin $s = 1$ or total spin $s = 0$. These are called a triplet and a singlet state, respectively. These two states can be found by using quantum mechanical spin addition properties. They become [7]

$$\chi_s = \frac{1}{\sqrt{2}}(\chi_{\uparrow\downarrow} - \chi_{\downarrow\uparrow}) \quad \chi_t = \begin{cases} \chi_{\uparrow\uparrow} \\ \frac{1}{\sqrt{2}}\left(\chi_{\uparrow\downarrow} + \chi_{\downarrow\uparrow}\right) \\ \chi_{\downarrow\downarrow} \end{cases} \tag{2.3}$$

The arrows denote the direction of spin particle 1 or 2. From equation 2.3 the singlet state gives spin in opposing directions. Therefore, it is clear that the singlet state is associated with antiferromagnetism, while the triplet state is associated with the triplet state. The effect of opposing and non-opposing spins arises from a demand for total antisymmetry, essentially the Pauli principle.

The previous consideration of fermionic symmetry gives an explanation of how antiferromagnetism and ferromagnetism arise. However, it is possible to rewrite the Hamiltonian in equation 2.1 to the exchange energy in the well-known Heisenberg model for interacting spins, $E = J\vec{S}_1 \cdot \vec{S}_2$. The following aims to show how. Starting with the fact that the total wave function of the triplet state and singlet state both have to be antisymmetric, the only possible combination of spatial and spin states become

$$\Psi_t = \psi_a\chi_t \quad \Psi_s = \psi_s\chi_s. \tag{2.4}$$

The energy of the triplet and singlet state E_t and E_s can be evaluated from the expected value of the Hamiltonian in equation 2.1

$$E_{t/s} = \int \psi^*_{t/s}(\vec{r}_1, \vec{r}_2)\hat{\mathcal{H}}\psi_{t/s}(\vec{r}_1, \vec{r}_2) \tag{2.5}$$

with the difference $E_t - E_s$ can be written as

$$E_t - E_s = 2\int \psi_1^*\psi_2^*\hat{\mathcal{H}}\psi_2\psi_1. \tag{2.6}$$

The total spin operator $\hat{S} = \hat{S}_1 + \hat{S}_2$, with $\hat{S}^2 = \hat{S}_1^2 + \hat{S}_2^2 + 2\hat{S}_1 \cdot \hat{S}_2$ can help to rewrite 2.1, by observing that

$$\begin{aligned} \hat{S}^2\Psi_s &= 0 \\ \hat{S}^2\Psi_t &= 2\hbar^2\Psi_t. \end{aligned} \tag{2.7}$$

Where the eigenvalues can be found more carefully in source [7]. The Hamiltonian of equation 2.1 can then be rewritten to

$$\begin{aligned} \hat{\mathcal{H}} &= E_s + \frac{E_t - E_s}{2\hbar^2}\hat{S}^2 \\ &= E_s + \frac{E_t - E_s}{2\hbar^2}(\hat{S}_1^2 + \hat{S}_2^2 + 2\hat{S}_1 \cdot \hat{S}_2) \\ &= \frac{1}{4}(E_s + 3E_t) + \frac{E_t - E_s}{\hbar^2}\hat{S}_1 \cdot \hat{S}_2 \end{aligned} \tag{2.8}$$

Where the eigenvalue of $\hat{S}_i = \hbar s = \pm\frac{\hbar}{2}$. Equation 2.8 comes with some interesting insight. Foremost, apart from the constant term, the two-particle energy is fully determined by the spin-spin interaction of 1 and 2. The effective field of such a free energy contribution is fully determined by the $S_1 \cdot S_2$ term, so the dynamics of the two-particle system are governed by the spin-spin exchange interaction. This result also generalizes to multiple particles. Secondly, the term $E_t - E_s$ fully determines when the free energy is minimized when the spins are parallel or antiparallel, that is if the ground state is ferromagnetic($S_i \parallel S_j$, $E_t - E_s < 0$) or antiferromagnetic($S_i \parallel -S_j$, $E_t - E_s > 0$). Finding the actual many-particle interaction function is very complicated and not a part of this thesis. However, the common way to include the interaction function is the interacting term that was found in equation 2.8

$$\hat{\mathcal{H}} = \sum_{i,j} J\vec{S}_i \cdot \vec{S}_j. \tag{2.9}$$

Where $J = (E_t - E_s)/\hbar^2$, and the summation is done over lattice spins at position i and j. Equation 2.9 is the interacting term of the Heisenberg model. This contribution to the Hamiltonian is often the dominant term in the spin-spin exchange interaction. It is also the term that will be used later.

2.1.2 Magnetic dipole interaction

In addition to the Heisenberg-like exchange found above, dipole-dipole interaction between the atoms in the material also contribute to the exchange interaction. The magnetic field due to a dipole moment $\vec{m}$ can be expressed as the following B field [8]

$$\vec{B}_{dip}(\vec{r}) = \frac{\mu_0}{4\pi}\frac{1}{r^3}[3(\vec{m} \cdot \hat{r})\hat{r} - \vec{m}]. \tag{2.10}$$

Where μ_0 is the magnetic permeability in a vacuum. The inner energy of a magnetic moment in a magnetic field is given as [8]

$$U = -\vec{m} \cdot \vec{B}. \tag{2.11}$$

Consider now such a field arising from a dipole ($\vec{m}_1$) interacting with another dipole ($\vec{m}_2$). By inserting into the potential energy formula in equation 2.11 one arrives at the following term for the Hamiltonian contribution of a dipole-dipole interaction

$$U = \frac{\mu_0}{4\pi}\frac{1}{r^3}[\vec{m}_1 \cdot \vec{m}_2 - 3(\vec{m}_1 \cdot \hat{r})(\vec{m}_2 \cdot \hat{r})]. \tag{2.12}$$

Here $\vec{m}_1$ and $\vec{m}_2$ are magnetic moments and r is the separation distance and $\hat{r}$ is the normalized direction vector between $\vec{m}_1$ and $\vec{m}_2$. By ignoring the angular dependence, it is possible to estimate the energy of equation 2.12 by using a typical magnetic moment of an electron $|\vec{m}| \approx g_s\mu_B \approx 2\mu_B$ and a typical lattice spacing which is usually a couple of Angstroms $\sim 10^{-10}$. Inserting this into equation 2.12 the result is of order $\sim 10^{-4}eV$, which is much less than the usual energy split caused by the Heisenberg exchange interaction in equation 2.9. Thus it is possible to omit the dipole interaction in further analysis.

2.1.3 Anisotropic interaction

Anisotropy is an effect caused mainly by the geometry of the system. Usually, it gives rise to a preferable direction in the ground state of the magnetization vector. In terms of energy, the effect causes it to be more challenging to magnetize materials in some directions than others. Magneto crystalline anisotropy is the most important form of anisotropy in magnetic systems. The orbital motion of electrons coupling to the electric field causes the effect in the material. The anisotropic interaction is usually much smaller than the exchange interaction. However, it still usually decides the direction of the ground state energy of a magnetic system since the exchange interaction only gives energy minima in parallel or antiparallel states (it is isotropic regarding the crystalline axis) [9]. By viewing the normalized magnetization vector's $\vec{m} = \frac{\vec{M}}{|M|}$ deviation from the crystalline axis, a contribution to the free energy can be found. By using spherical coordinates, the magnetization vector can be expressed as

$$\begin{aligned} \alpha_1 &= \sin\theta\cos\phi \\ \alpha_2 &= \sin\theta\sin\phi \\ \alpha_3 &= \cos\theta \\ \vec{m} &= (\alpha_1, \alpha_2, \alpha_3). \end{aligned} \tag{2.13}$$

By introducing the identities in equation 2.13 it is possible to expand the anisotropic energy as a power series of α_i,

$$E_{ani} = E_0 + \sum_i b_i\alpha_i + \sum_{ij} bij\alpha_i\alpha_j + \sum_{ijk} b_{ijk}\alpha_i\alpha_j\alpha_k + \mathcal{O}(\alpha^4). \tag{2.14}$$

Where b is the anisotropic interaction strength. Here orders over α^3 have been ignored. There is no energetic difference for opposing systems, meaning that there can only be even terms in the power series since it is required that $E(M) = E(-M)$. That is, E has to be an even function. Therefore, the anisotropic energy shortens to the following by adjusting the zero-point energy

$$E_{ani} = \sum_{ij} bij\alpha_i\alpha_j. \tag{2.15}$$

By generalizing equation 2.15 into a matrix-vector product this can be rewritten into a more convenient shape

$$E_{ani} = \omega\vec{m}^2. \tag{2.16}$$

Here ω is a 3×3 matrix of both direction vectors and the strength of the anisotropic interaction of the system.

2.1.4 Dzyaloshinskii-Moriya Interaction

Dzyaloshinskii-Moriya Interaction or DMI is an antisymmetric contribution to the spin-spin exchange energy. The interaction is a form of superexchange interaction, meaning that it is a next to nearest neighbour interaction instead of nearest-neighbour interaction. It was generalized by Anderson in 1950 [10]. Moriya showed later by using second order perturbative theory that the origin of the interaction is spin-orbit coupling [11]. It can also be viewed as a phenomenon due to a lack of inversion symmetry. It is not within the grasp of this thesis to show the derivation.

DMI gives rise to a spin canting of neighbouring magnetic moments. It can modify the ground state by breaking the uniform linear state, leading to magnetization in antiferromagnets and a finite Néel vector in ferromagnets. The most common way to introduce DMI in the lattice Heisenberg model is through the following term,

$$E = -\sum_{ij} \vec{D}_{ij} \cdot [\vec{S}_i \times \vec{S}_j]. \tag{2.17}$$

In general, $\vec{D}$ is called the DMI vector and determines the direction and strength of the interaction. It can, in principle be, vary across the material. For a ground state in the xz plane and a DMI vector in the y direction, the energy in equation 2.17 is minimized if $\vec{S}_i$ and $\vec{S}_j$ are perpendicular within the plane. Therefore, the DMI term can give some canting affinity in the ground state as it modifies the energy through a term minimizing on perpendicular spin vectors if $\vec{D}$ is perpendicular to the ground state. This then combats the direct exchange interaction, which in equation 2.9 was shown to minimize at parallel or antiparallel $\vec{S}_i$ and $\vec{S}_j$. However, DMI is usually of much smaller amplitude [11].

2.1.5 Zeeman coupling

The coupling of the spin-lattice with a magnetic field is called Zeeman coupling after Pieter Zeeman observed the effect in the 19th century. In order to derive the effect, it is possible to use perturbation theory. However, it is not included here. It can be found in detail in Hemmer's "Kvantemekanikk" [7]. The essence is that when assuming that the nucleus part to the total magnetic moment is negligible, the energy coupling to the external magnetic field is entirely spin-related and can be expressed as [7]

$$E = -\sum_i \mu \vec{h} \cdot \vec{S}_i. \tag{2.18}$$

Where μ is the magnetic permeability, $\vec{h}$ is the magnetic field, and $\vec{S}_i$ is the spin at lattice position i. The energy minimizes when the spin is parallel or antiparallel with $\vec{h}$, depending on the sign of $\vec{h}$. However, in antiferromagnetic, the ground state shows different behaviour. There are regimes in the antiferromagnetic case where the direction of the ground state is perpendicular to the magnetic field.

2.1.6 Spin Transfer Torque

In addition to the above internal contributions to the free energy (meaning it arises from the system itself), it is possible to excite dynamics by external torque addition in ferromagnetic and antiferromagnetic materials. The effect was first found by Slonczewski in 1996 and is therefore often referred to as Slonczewski torque [12]. The torque is found in magnetic bilayers where a heavy metal layer is placed above or below a ferro/antiferromagnetic layer. Many heavy metals have a high spin-orbit coupling, which causes a current in the material to be polarized. When passing a polarized current in the heavy metal, spins are perturbed in the ferro/antiferromagnetic material, and spin-wave dynamics can appear. A typical choice of heavy metal is Platinum.

When this torque enters the LLG equation, which is the equation of motion found later, the equation is often referred to as the LLGS equation. The derivation of the torque terms is not within the scope of this thesis, but they can be found to be [13]

$$\tau = a(j)(\vec{m} \times (\vec{m} \times \hat{p})) + b(j)(\vec{m} \times \hat{p}). \tag{2.19}$$

Where $a(j)$ and $b(j)$ are current density dependant in-plane and out of plane prefactors. $\hat{p}$ denotes the spin polarization in the Columb current in the adjacent material. From Slonczewski, these prefactors are

$$\begin{aligned} a(j) &= -\frac{2\mu_B J}{dM_s^3 e} g(\vec{m}, \hat{p}) \\ b(j) &= \frac{2\mu_B \alpha J}{dM_s^2 e} g(\vec{m}, \hat{p}). \end{aligned} \tag{2.20}$$

Here, μ_B is the Bohr magneton, J is the current density, d is the thickness of the free layer, and e is the electron charge. The scalar function $g(\vec{m}, \hat{p})$ was derived by Slonczewski [12], and is

$$g(\vec{m}, \hat{p}) = \left(-4 + (1+\eta)^3 \frac{3 + \vec{m} \cdot \hat{p})}{4\eta^{3/2}} \right)^{-1}. \tag{2.21}$$

Where η is the spin polarizing factor, and $\vec{m}$ is the normalized magnetization vector [14]. This thesis focuses on systems where the ground state $\vec{m}$ is perpendicular to $\hat{p}$, meaning $\vec{m} \cdot \hat{p} = 0$. In addition, the second term of equation 2.19 is assumed small such that the only term contributing is $\sim \tau \vec{m} \times \vec{m} \times \hat{p}$, where τ contains the prefactor in equation 2.20.

2.2 The continuum limit of the lattice model

It is often helpful to write the Hamiltonian in terms of continuous variables. This subsection shows the procedure for the terms presented in the free energy above.

2.2.1 Exchange Interaction

To get the Hamiltonian from equation 2.9 into a continuum model, only the nearest neighbour interaction is considered. Which is a fair assumption, as the exchange coupling constant J_{ij} is expected to drop with distance. Writing out equation 2.9 for two neighbouring spins S_i and S_{i+1}

$$H = -\sum_i J_{ij} S_i \cdot S_{i+1} = -\sum_i J_{ij} (S_i^x S_{i+1}^x + S_i^y S_{i+1}^y + S_i^z S_{i+1}^z). \tag{2.22}$$

Now rewriting the inner sum $S_i^x S_{i+1}^x + S_i^y S_{i+1}^y + S_i^z S_{i+1}^z$ by using $(S_i^q - S_{i+1}^q)^2 = (S_i^q)^2 - 2S_i^q S_{i+1}^q + (S_{i+1}^q)^2$ and isolating the $S_i^q S_{i+1}^q$ terms, equation 2.22 becomes

$$H = -\sum_i J_{ij} \left((S_{i+1}^x - S_i^x)^2 + (S_{i+1}^y - S_i^y)^2 + (S_{i+1}^z - S_i^z)^2 \right) + \frac{1}{2}(|S_i|^2 + |S_{i+1}|^2) \tag{2.23}$$

The spins are of constant length, $|S_i|^2 = S^2$ and therefore, the two last terms in equation 2.23 can be omitted from further consideration by adjusting the zero-point energy. By doing so, H becomes

$$H = -\sum_i J_{ij} h S \left(\frac{(s_{i+1}^x - s_i^x)^2}{h} + \frac{(s_{i+1}^y - s_i^y)^2}{h} + \frac{(s_{i+1}^z - s_i^z)^2}{h} \right). \tag{2.24}$$

Here h is a lattice spacing, and $\vec{S} = \vec{s}/S$ where $\vec{s}$ is a unit length vector. Now let h go to 0 to arrive at the continuum version of the direct exchange, assuming that the coupling constant is equal for all points on the lattice

$$H = \int d^3 r J (\nabla m)^2. \tag{2.25}$$

The spin variable was transformed to its macroscopic equivalent, magnetization $\vec{m}$, and the J variable was renormalized in the process. The procedure to find the exchange energy in the macroscopic approximation is also useful for antiferromagnets, even though the method was used on a ferromagnetic basis. It is primarily used when describing an antiferromagnet in terms of sublattice magnetization, which is the preferred method for later numerical work in this thesis. However, it is also prudent to show the antiferromagnetic free energy in terms of the Néel vector ($\vec{n}$ in equation 2.26) as it is often easier to work with in analytical calculations.

In order to find a term for the free energy containing both $\vec{m}$ and $\vec{n}$, it is beneficial to define a new set of variables $\vec{m}_i$ and $\vec{n}_i$. These can be defined in the following manner,

$$\begin{aligned} \vec{m}_i &= (\vec{S}_i + \vec{S}_j)/(2S) \\ \vec{n}_i &= (\vec{S}_i - \vec{S}_j)/(2S). \end{aligned} \tag{2.26}$$

Here S denotes the spin's absolute value. By inserting the expressions in equation 2.26 the two following identities can be found $\vec{m}_i^2 + \vec{n}_i^2 = 1$ and $\vec{m} \cdot \vec{n} = 0$. Rewriting $\vec{S}_i$ and $\vec{S}_j$ in terms of $\vec{n}_i$ and $\vec{m}_i$ gives

$$\begin{aligned} \vec{m}_i + \vec{n}_i &= \vec{S}_i/S \\ S_i &= S(\vec{m}_i + \vec{n}_i) \\ \vec{m}_i - \vec{n}_i &= \vec{S}_j/S \\ \vec{S}_j &= S(\vec{m}_i - \vec{n}_i). \end{aligned} \tag{2.27}$$

The new parameters can then be introduced back into the Heisenberg Hamiltonian

$$H = -\sum_{\langle ij \rangle} J_{ij} \vec{S}_i \cdot \vec{S}_j. \tag{2.28}$$

Using the identities in equation 2.27 in equation 2.28 the Heisenberg Hamiltonian becomes the following in terms of $\vec{n}$ and $\vec{m}$ [15]

$$H = -\sum_{j=1}^{N-1} J_{ij}(S^2(\vec{m}_i - \vec{n}_i)[(\vec{m}_i + \vec{n}_i) + (\vec{m}_{i+1} + \vec{n}_{i+1})]) + JS^2(\vec{m}_n^2 + \vec{n}_n^2). \tag{2.29}$$

Writing the products out and assuming once again that nearest neighbour interactions dominate the energy,

$$\begin{aligned} H = -JS^2 \sum_i (\vec{m}_i^2 + \vec{m}_i \cdot \vec{m}_{i+1} + \vec{m}_i \vec{n}_{i+1} - \vec{n}_i^2 - \vec{n}_i \cdot \vec{m}_{i+1} - \vec{n}_i \cdot \vec{n}_{i+1}) \\ + JS^2(\vec{m}_N^2 - \vec{n}_N^2). \end{aligned} \tag{2.30}$$

This is not yet a convenient expression to use to get to a continuum limit so it is beneficial to introduce the following two identities

$$\begin{aligned} \vec{m}_i^2 + \vec{m}_{i+1}^2 &= 2\vec{m}_i \cdot \vec{m}_{i+1} + (\vec{m}_{i+1} - \vec{m}_i)^2 \\ \vec{m}_i \cdot \vec{n}_{i+1} - \vec{n}_i \cdot \vec{m}_{i+1} &= \vec{m}_i(\vec{n}_{i+1} - \vec{n}_i) - \vec{n}_i(\vec{m}_{i+1} - \vec{m}_i). \end{aligned} \tag{2.31}$$

Now inserting these two identities into the Heisenberg Hamiltonian in equation 2.30 the free energy can be rewritten as

$$\begin{aligned} H = 2JS^2 \sum_i (\vec{m}_i^2 - \vec{n}_i^2) + \frac{JS^2}{2} \sum_i [(\vec{n}_{i+1} - \vec{n}_i)^2 - (\vec{m}_{i+1} - \vec{m}_i)^2] \\ + JS^2 \sum_i [\vec{m}_i(\vec{n}_{i+1} - \vec{n}_i) - \vec{n}_i(\vec{m}_{i+1} - \vec{m}_i)] + JS^2(\vec{m}_N^2 - \vec{n}_N^2). \end{aligned} \tag{2.32}$$

The terms $\vec{m}_1^2 + \vec{m}_N^2 - \vec{n}_1^2 - \vec{n}_N^2$ are constant and are as before omitted from further calculations. Now going to the continuum limit with the same method as for the ferromagnetic case (equation 2.24), it is possible to rewrite the sum in equation 2.32 to a continuum limit with integrals

$$\begin{aligned} F &= \int \frac{d_i}{\Delta} f(\vec{n}, \dot{\vec{n}}, \vec{m}, \dot{\vec{m}}) \\ f &= JS^2 \Big[4\vec{m}^2 + (\nabla \vec{n})^2 - (\nabla \vec{m})^2 + (\vec{m} \cdot \nabla \vec{n} - \vec{n} \cdot \nabla \vec{m}) \Big]. \end{aligned} \tag{2.33}$$

Considering that this is an antiferromagnetic system, $\vec{m}$ is small and expected to vary slowly across the one-dimensional chain $\nabla m \sim 0$ and hence the third and fifth terms of equation 2.33 can be dropped. Then the final integral becomes

$$F[\vec{m}, \vec{n}] = \int d^3r \left(\frac{1}{2\chi} |\vec{m}|^2 + \frac{A}{2} |\nabla \vec{n}|^2 + L\vec{m} \cdot \nabla \vec{n} \right). \tag{2.34}$$

Here $\chi = \frac{a}{4|J|S^2}$, $A = a^2|J|S^2$ and $L = 2a|J|S^2$ [16].

2.2.2 DMI

To get a semiclassical expression for equation 2.17 a summation over all the spins in the chain is performed,

$$\begin{aligned} E &= \sum_i \vec{D}_{ij} [S_i^y S_z^{i+1} - S_z^i S_y^{i+1} + S_x^i S_z^{i+1} - S_z^i S_x^{i+1} + S_i^x S_{i+1}^y - S_i^y S_x^{i+1}] \\ &= \sum_i \vec{D}_{ij} [S_i^x \left(\frac{S_{i+1}^y - S_i^y}{h} \right) - S_i^y \left(\frac{S_{i+1}^x - Si^x}{h} \right) + S_i^z \left(\frac{S_{i+1}^x - S_i^x}{h} \right)] h. \end{aligned} \tag{2.35}$$

Here h is the lattice constant. By letting h approach zero, the sum can be rewritten as an integral

$$E_{DMI} = \int d^3r D\vec{m} \cdot (\nabla \times \vec{m}). \tag{2.36}$$

This yields the ferromagnetic expression for DMI energy. In the antiferromagnetic model, the results differ slightly

For the antiferromagnetic model, the starting point is again the Heisenberg Hamiltonian for the DMI,

$$H = -\sum_{i=1}^{2N}(-1)^i \vec{D}_{ij} \cdot (\vec{S}_{i-1} \times \vec{S}_i). \tag{2.37}$$

Here an alternating sign was added to model the opposing nature of neighbouring $\vec{S}_i$. By again introducing the variables in equation 2.26, this sum can be written as

$$\begin{aligned} H = S^2 \sum_{i=1}^{N-1} \vec{D} \cdot [\vec{m}_i \times (\vec{n}_i + \vec{n}_{i+1}) - \vec{n}_i \times (\vec{m}_i + \vec{m}_{i+1})] \\ + S^2 \sum_{i=1}^{N-1} \vec{D} \cdot [\vec{m}_i \times (\vec{m}_{i+1} - \vec{m}_i) - \vec{n}_i \times (\vec{n}_{i+1} - \vec{n}_i)] \end{aligned} \tag{2.38}$$

Going to the continuum limit then yields the following integral

$$E = \int d^3r \frac{2S^2}{h} \vec{D} \cdot (\vec{m} \times \vec{n}) - S^2 \vec{D} \vec{n} \cdot (\nabla \times \vec{n}). \tag{2.39}$$

Here a term on the form $\vec{m} \times \nabla m$ has been omitted due to the spatial derivative of $\vec{m}$ being close to zero when there is antiferromagnetic ordering, i.e. $\nabla \vec{m} \sim 0$. In addition, higher-order terms of the order parameters have been omitted.

2.2.3 Zeeman interaction and anisotropy

The rest of the effects are, as mentioned previously, local in the spin chain, which means that they can be expanded into the continuum case without any spin-spin exchange consideration. Therefore, no terms on the form $\nabla \vec{m}$ enters the continuum limit. The method for approaching the continuum limit is the same for both the Zeeman term and the anisotropy. Therefore, just the continuum limit for the Zeeman term is shown here. Again, the spin chain Hamiltonian interaction with the magnetic field is

$$\begin{aligned} H_i &= -\mu \vec{h}_i \cdot \vec{S}_i \\ H &= -\sum_{i}^{2N} \mu \vec{h}_i \cdot \vec{S}_i. \end{aligned} \tag{2.40}$$

The h_i variable is here the magnetic field in lattice position i at time t. To go to the continuum model, one only needs to change variables from $\vec{S}_i$ to $\vec{m}_i$ using the previous definition. At the same time introducing a small lattice spacing a, the energy in terms of the magnetization

becomes

$$H = -\sum_{i}^{2N} \mu \vec{h}_i \cdot \vec{S}_i = -\sum_{i}^{N} 2Sa\left(\frac{\mu \vec{h}_i \cdot \vec{m}_i}{a}\right). \tag{2.41}$$

Letting a go towards zero in equation 2.41, similarly to the exchange continuum limit, the sum can be approximated with an integral

$$E_{Zeeman} = \int d^3 r \omega_h \vec{h}(r,t) \cdot \vec{m}. \tag{2.42}$$

ω_h has here absorbed μ, $|B|$, and $2S$. A similar method is used to find the anisotropic exchange in the continuum limit. It is not included here.

Now that the terms of the free energy are established, the next step is to investigate how they enter the equations of motion in antiferromagnets. First, a description of antiferromagnetic dynamics is done by examining sublattice magnetization. The equation of motion is expressed using a combination of magnetization and Néel order parameter before a purely Néel vector description is used.

2.3 Equation of motion for antiferromagnets

The LLG equation can be derived phenomenologically by starting with the spin angular momentum operator's interaction with the magnetic field given by the hamiltonian $H_z = -\frac{g\mu_B}{\hbar}\vec{S} \cdot \vec{B}(t)$ in a ferromagnet. The expectation value of the quantum mechanical spin operator $\vec{S}$ can be found to be [7]

$$\frac{d}{dt}\langle \vec{S}(t) \rangle = -\frac{g\mu_B}{\hbar}\langle \vec{S}(t) \rangle \times \vec{B}(t) \rangle. \tag{2.43}$$

Working with a larger non-atomistic scale, it is prudent to look at magnetization and not individual spins, where using the same notation as above (equation 2.26) for the magnetization vector

$$\vec{M} = \langle \vec{S} \rangle. \tag{2.44}$$

Inserting the definition of the magnetization in equation 2.44 into equation 2.43

$$\frac{d\vec{M}}{dt} = -\gamma_0 \mu_0 [\vec{M}(t) \times \vec{H}(t)]. \tag{2.45}$$

Where, γ_0 is defined as $\gamma_0 = \frac{g\mu_B}{\hbar}$, $\vec{B} = \mu_0 \vec{H}$. This yields the basic precessing nature of the magnetization around a magnetic field. This can be seen by observing that the time derivative of $\vec{M}$ is the cross product of $\vec{M}$ and $\vec{B}$, meaning that the length of $\vec{M}$ is conserved as the derivative is perpendicular to $\vec{M}$. Since the derivative is perpendicular at all times, this causes rotation. However, it has been shown that the precessing vector dampens over

time [17]. To incorporate the dampening effect into the equation of motion, a term of the form $\vec{m} \times \dot{\vec{m}}$ can be included

$$\frac{d\vec{m}(t)}{dt} = -\gamma \vec{m} \times \vec{B} + \alpha \vec{m} \times \dot{\vec{m}} \tag{2.46}$$

Where α is a damping parameter, referred to as Gilbert damping and $\gamma = \gamma_0 \mu_0$. The magnetization vector length remains conserved, but it now relaxes into the direction of the B field. The conservation of length is as before, due to the time derivative of $\vec{M}$ always being a function of the cross product containing $\vec{M}$ itself.

For now, the derivation was made using a magnetic field $\vec{B}$. However, multiple interactions can be included in the field term. It is usually written as $\vec{H}_{eff}$. $\vec{H}_{eff}$, the effective field can consist of, for example, exchange field, anisotropic field and DMI field contributions. To include other interactions in the effective field, the free energies from subsection 2.1 needs to be computed to field contributions. These field terms $\vec{H}_{eff}$ can be found through the following functional,

$$\vec{H}_{eff} = \frac{-\delta F[\vec{m}, \nabla \vec{m}]}{\delta \vec{m}}. \tag{2.47}$$

Equation 2.46 when containing effective field contributions is often referred to as the Landau-Lifshitz-Gilbert equation(LLG equation). It is also possible to arrive at the LLG equation using Lagrange formalism. This is shown later, in section 2.3.2. Before that, the result from equation 2.46 is utilized to describe antiferromagnet dynamics through a sublattice description. This is the preferred form of the LLG equation for simulations performed in this thesis.

2.3.1 The equation of motion for an antiferromagnet in terms of magnetization in sublattices

In order to transform equation 2.46 into an antiferromagnet equation. One can expand the previous description by assuming antiferromagnetic ordering. That is, by assuming that the material contains two sublattices of opposing local magnetization, $\vec{M}_a$ and $\vec{M}_B$. Furthermore, assuming that both $\vec{M}_A$ and $\vec{M}_B$ follows the LLG equation, the sublattice i dynamics can be written as

$$\dot{\vec{M}}_i(\vec{r}, t) = -\gamma \vec{M}_i \times \vec{H}^i_{eff} + \alpha \vec{M}_i \times \dot{\vec{M}}_i + \vec{M}_i \times \vec{M}_i \times \vec{\tau}_i. \tag{2.48}$$

Where i here denotes either sublattice A or B, H^i_{eff} the effective field in sublattice A or B, and τ the external torque on the system which is an external addition to the derivative of $\vec{M}$. It is often prudent to work with the normalized magnetization $\vec{m} = \vec{M}/M_s$, where M_s is the saturation magnetization. Normalized quantities often behave better under numerical

integration. In order to do so, first divide equation 2.48 by the factor $\gamma_0\mu_0 M_s^2$. This yields

$$\frac{1}{\gamma_0\mu_0 M_s^2}\frac{d\vec{M}_i}{dt} = -\frac{1}{M_s^2}\vec{M}_i \times \vec{H}_{eff} + \frac{\alpha}{\gamma_0\mu_0 M_s^3}\left(\vec{M}_i \times \frac{d\vec{M}_i}{dt}\right) + \frac{1}{\gamma_0\mu_0 M_s^2}\vec{M}_i \times \vec{M}_i \times \vec{\tau} \quad (2.49)$$

Inserting the normalized magnetization vector equation 2.49 becomes,

$$\frac{1}{\gamma_0\mu_0 M_s}\frac{d\vec{m}_i}{dt} = -\vec{m}_i \times \vec{h}_{eff} + \frac{\alpha}{\gamma_0\mu_0 M_s}\left(\vec{m}_i \times \frac{d\vec{m}_i}{dt}\right) + \frac{1}{\gamma_0\mu_0}\vec{m}_i \times \vec{m}_i \times \vec{\tau}. \quad (2.50)$$

Where $h_{eff} = H_{eff}/M_s$. Now by rescaling the time axis by a factor of $\gamma_0\mu_0 M_s$ such that $t' = (\gamma_0\mu_0 M_s)t$ and $dt' = (\gamma_0\mu_0 M_s)dt$ an equation for the normalized magnetization vector can be found

$$\dot{\vec{m}}_i = -\vec{m} \times \vec{h}_{eff} + \alpha\vec{m}_i \times \dot{\vec{m}}_i + \vec{m} \times \vec{m} \times \vec{\tilde{\tau}}. \quad (2.51)$$

Where $\vec{\tilde{\tau}}$ has absorbed the torque prefactor in equation 2.50. Working with the implicit equation in equation 2.51 numerically is quite complicated. Therefore it is often useful to use the explicit variant. Firstly, by taking the cross product of the equation with $\vec{m}_i$

$$\vec{m}_i \times \dot{\vec{m}}_i = -\vec{m}_i \times \vec{m} \times \vec{h}_{eff} + \alpha\vec{m}_i \times \vec{m}_i \times \dot{\vec{m}}_i + \vec{m}_i \times \vec{m}_i \times \vec{m} \times \vec{\tilde{\tau}}. \quad (2.52)$$

By vector identities the term with prefactor α can be rewritten as

$$\vec{m}_i \times \vec{m}_i \times \vec{m}_i = \vec{m}_i(\vec{m}_i \cdot \dot{\vec{m}}_i) - \dot{\vec{m}}_i(\vec{m}_i \cdot \vec{m}_i). \quad (2.53)$$

In the new normalized variables, $\vec{m}_i \cdot \vec{m}_i = 1$ which in addition to simplifying the second term gives the following insight to the first $\frac{d}{dt}(\vec{m}_i \cdot \vec{m}_i) = \frac{d}{dt}1 = 0$. The torque term can also be simplified by the same vector identity. The result becomes

$$\vec{m}_i \times \vec{m}_i \times \vec{m} \times \vec{\tilde{\tau}} = -\vec{m}_i \times \vec{\tilde{\tau}}. \quad (2.54)$$

Equation 2.52 then simplifies to

$$\vec{m}_i \times \dot{\vec{m}}_i = -\vec{m}_i \times \vec{m} \times \vec{h}_{eff} - \alpha\dot{\vec{m}}_i - \vec{m}_i \times \vec{\tilde{\tau}}. \quad (2.55)$$

Going back to equation 2.51 and substituting in $\vec{m}_i \times \dot{\vec{m}}_i$ into 2.55 and isolating the terms for $\dot{\vec{m}}_i$ on the left-hand side then finally gives an explicit expression for $\dot{\vec{m}}_i$.

$$\dot{\vec{m}}_i = -\frac{1}{1+\alpha^2}\left(\vec{m}_i \times \left[\vec{h}_i^{eff} + \alpha\vec{m}_i \times \vec{h}_i^{eff} + \vec{\tau}_i - \alpha \times \vec{m}_i \times \vec{\tau}_i\right]\right) \quad (2.56)$$

Finding the effective field remains an unsolved problem for now. As mentioned in equation 2.47 the effective field can be written as a functional derivative of the free energy. The free energy contains to reiterate the following terms

$$F = \frac{1}{V}\int d^3\vec{r}(f_{ex} + f_{ani} + f_Z + f_{DMI}). \quad (2.57)$$

Equation 2.57 has four contributions, exchange energy, anisotropic exchange, magnetic field interaction(f_Z) and Dzyaloshinskii-Moriya(DMI) interactions. The free energy densities written out becomes (when writing the previous expression for f with $\vec{m}$ and $\vec{n}$ in terms of $\vec{m}_A$ and $\vec{m}_B$)

$$\begin{aligned} f_{ex} &= -\omega_{ex}\vec{m}_A(\vec{r},t)\cdot\vec{m}_B(\vec{r},t) + \frac{A^{(1)}}{2}[(\nabla\vec{m}_A)^2 + (\nabla\vec{m}_B)^2] + A^{(2)}(\nabla\vec{m}_A\cdot\nabla\vec{m}_B) \\ f_{ani} &= \sum_{\hat{e}_i}\frac{\omega_i^{(1)}}{2}[(\vec{m}_A\cdot\hat{e})^2 + (\vec{m}_B\cdot\hat{e})^2] + \omega_i^{(2)}(\vec{m}_A\cdot\hat{e})(\vec{m}_B\cdot\hat{e}) \\ f_Z &= \omega_h\vec{h}(\vec{r},t)\cdot(\vec{m}_A+\vec{m}_B) \\ f_{DMI} &= \vec{d}\cdot\vec{m}_A\times\vec{m}_B + D\vec{m}_A(\nabla\times\vec{m}_A) + D\vec{m}_B(\nabla\times\vec{m}_B). \end{aligned} \tag{2.58}$$

Some new variables have been introduced, w_{ex} denotes the intra-lattice interaction, i.e., it gives energetic stability when $\vec{m}_A$ is antiparallel to $\vec{m}_B$. $A^{(1)}$ and $A^{(2)}$ denotes inter-lattice exchange and is given as $A = A^{(1)} - A^{(2)}$. Similarly, the anisotropic constant ω_i is expanded as $\omega_i = \omega_i^{(1)} - \omega_i^{(2)}$ and contains the strength of the anisotropic interaction in direction $\hat{e}_i$. ω_h is the magnetic strength. It has here absorbed the field strength of $\vec{h}$, the normalized magnetic field. $\vec{d}$ is the homogeneous DMI strength and direction, while D denotes the inhomogeneous DMI prefactor. All of these can be computed into terms of the effective hamiltonian density by taking the aforementioned functional derivative (equation 2.47)

$$\begin{aligned} \vec{H}_{ex}^{A/B} &= [\omega_{ex}\vec{m}_{B/A} - A^{(1)}\nabla^2\vec{m}_{A/B} - A^{(2)}\nabla^2\vec{m}_{B/A}] \\ \vec{H}_{ani}^{A/B} &= \omega^{(1)}\vec{m}_{A/B}\hat{e} + \omega^{(2)}\vec{m}_{B/A}\hat{e} \\ \vec{H}_Z^{A/B} &= -\omega_h\vec{h} \\ \vec{H}_{DMI}^{A/B} &= -\vec{d}\times\vec{m}_{B/A} + 2D\nabla\times\vec{m}_{A/B}. \end{aligned} \tag{2.59}$$

Dividing the prefactors with M_s renormalizes the effective field contributions into the normalized $\vec{h}_{eff}$. Using the effective field contributions of equation 2.59 the magnetization dynamics in an antiferromagnet under the influence of exchange interaction, anisotropic interaction, Zeeman interaction and DMI can be found. Usually through a numerical integration scheme. In this thesis, a program developed by Viroshaaan Uthayamoorthy and me in collaboration with Alireza Qaiumzadeh is used. It can be found on GitHub [18]. This method of describing the dynamics through sublattice magnetization from the phenomenological LLG equation is not the only method to arrive at the results in equation 2.56. The following subsection shows how to do so from a Lagrangian mechanics approach.

2.3.2 Lagrangian approach to the LLG equation

It is possible to arrive at the LLG equation through a Lagrangian formalism using the previously found free energy. This subsection shows how to arrive at such an equation of

motion for an antiferromagnet using both the Néel vector $\vec{n}$ and the magnetization vector $\vec{m}$ that was introduced in section 2.1. The kinetic contribution to the energy can be found through a consideration of Berry phase in the lattice and is not included here. The result is however $L_B = -\rho\dot{\vec{n}} \cdot (\vec{n} \times \vec{m})$ [19]. To summarize, the free energy and kinetic energy terms are

$$\begin{aligned} L_B[\vec{m}, \vec{n}] &= -\rho\dot{\vec{n}} \cdot (\vec{n} \times \vec{m}) \\ F[\vec{m}, \vec{n}] &= \frac{\vec{m}^2}{2\chi} + \frac{A}{2}|\nabla\vec{n}|^2 + L\vec{m}\nabla\vec{n} - \frac{K}{2}(\vec{n} \cdot \hat{r})^2 \\ &+\vec{d} \cdot (\vec{m} \times \vec{n}) - \vec{H} \cdot \vec{m} + D\vec{n} \cdot (\nabla \times \vec{n}) \end{aligned} \tag{2.60}$$

Here the anisotropic interaction strength has been absorbed into K. $\hat{r}$ denotes the direction of the anisotropy. As mentioned earlier, when the Heisenberg Hamiltonian was expanded into a continuum limit, there are two main constraints on the system

$$\begin{aligned} \vec{n} \cdot \vec{m} &= 0 \\ |\vec{n}|^2 + |\vec{m}|^2 &= 1. \end{aligned} \tag{2.61}$$

That is $\vec{n}$ and $\vec{m}$ are perpendicular and the total length of $\vec{m}$ and $\vec{n}$ are conserved. These can be included as Lagrangian multipliers in the Lagrangian, they are however imposed differently here. The total Lagrangian becomes

$$\mathcal{L}_{tot} = \int d^3\vec{r}\mathcal{L} = \int d^3\vec{r}(L_B - F). \tag{2.62}$$

By the principle of least action both $\frac{\delta\mathcal{L}}{\delta\vec{n}} = 0$ and $\frac{\delta\mathcal{L}}{\delta\vec{m}} = 0$. Performing this derivative on $\mathcal{L}$ from equation 2.62 yields the two following equations of motion

$$\begin{aligned} \frac{\partial\mathcal{L}}{\partial\vec{m}} + \partial_t\frac{\partial\mathcal{L}}{\partial\vec{m}} &= 0 \\ \frac{\partial\mathcal{L}}{\partial\vec{n}} + \partial_t\frac{\partial\mathcal{L}}{\partial\vec{n}} &= 0 \end{aligned} \tag{2.63}$$

Inserting L_B and F from equation 2.60 this becomes

$$\begin{aligned} -\rho\dot{\vec{n}} \times \vec{n} &= \frac{\delta F}{\delta m} \\ -2\rho(\vec{m} \times \dot{\vec{n}}) - \rho(\dot{\vec{m}} \times \vec{n}) &= \frac{\delta F}{\delta\vec{n}}. \end{aligned} \tag{2.64}$$

By taking the cross product with $\vec{n}$ from the left they become

$$\begin{aligned} -\rho\vec{n} \times \dot{\vec{n}} \times \vec{n} &= \vec{n} \times \frac{\delta F}{\delta\vec{m}} \\ -2\rho\vec{n} \times (\vec{m} \times \dot{\vec{n}}) - \rho\vec{n} \times (\dot{\vec{m}} \times \vec{n}) &= \vec{n} \times \frac{\delta F}{\delta\vec{n}}. \end{aligned} \tag{2.65}$$

The constraints $|\vec{n}|^2 = 1$ and $\vec{m} \cdot \vec{n} = 0$ can give two more useful definitions

$$\begin{aligned} \dot{\vec{m}} \cdot \vec{n} &= -\vec{m} \cdot \dot{\vec{n}} \\ \frac{d}{dt}(|\vec{n}|^2) &= 2\vec{n} \cdot \dot{\vec{n}} = 0. \end{aligned} \tag{2.66}$$

Inserting the previously used definition for triple cross products and rewriting equation 2.65

$$\begin{aligned} -\rho((\vec{n} \cdot \vec{n})\dot{\vec{n}} - (\vec{n} \cdot \dot{\vec{n}})\vec{n}) &= \vec{n} \times \frac{\delta F}{\delta \vec{m}} \\ -2\rho((\vec{n} \cdot \dot{\vec{n}})\vec{m} - (\vec{n} \cdot \vec{m})\dot{\vec{n}}) - \rho((\vec{n} \cdot \vec{n})\dot{\vec{m}} - (\vec{n} \cdot \dot{\vec{m}})\vec{n}) &= \vec{n} \times \frac{\delta F}{\delta \vec{n}}. \end{aligned} \tag{2.67}$$

Imposing the constraints and it's derivatives from equation 2.66 this reduces to

$$\begin{aligned} -\rho\dot{\vec{n}} &= \vec{n} \times \frac{\delta F}{\delta \vec{m}} \\ -\rho\dot{\vec{m}} - \rho(\dot{\vec{n}} \cdot \vec{m})\vec{n} &= \vec{n} \times \frac{\delta F}{\delta \vec{n}}. \end{aligned} \tag{2.68}$$

Imposing the previously used vector identity again backwards and inserting $\dot{\vec{n}} \times \vec{n} = -\frac{1}{\rho}\frac{\delta F}{\delta \vec{m}}$ equation 2.68 becomes

$$\begin{aligned} \rho\dot{\vec{n}} &= -\vec{n} \times \frac{\delta F}{\delta \vec{m}} \\ \rho\dot{\vec{m}} &= -\vec{n} \times \frac{\delta F}{\delta \vec{n}} - \vec{m} \times \frac{\delta F}{\delta m}. \end{aligned} \tag{2.69}$$

The free energy functional of $\vec{m}$ and $\vec{n}$ can be found from the Free energy in equation 2.60 and becomes

$$\begin{aligned} \frac{\delta F}{\delta \vec{m}} &= \frac{\vec{m}}{\chi} + \vec{d} \times \vec{n} - \vec{H} + L\nabla\vec{n} \\ \frac{\delta F}{\delta \vec{n}} &= K(\vec{n} \cdot \hat{r})\hat{r} + A\nabla^2\vec{n} + L\nabla\vec{m} + \vec{d} \times \vec{m} + 2D\nabla \times \vec{n}. \end{aligned} \tag{2.70}$$

Now that the free energy density has been found an equation of motion can be retrieved from equation 2.69. This is not however the full picture, as $\vec{m}$ can be fully excluded from the equations of motion. This can be shown by taking the cross product of the first line in equation 2.69

$$\rho\vec{n} \times \dot{\vec{n}} = -\vec{n} \times (\vec{n} \times \frac{\delta F}{\delta \vec{m}}) = \chi^{-1}\vec{m} + L\nabla\vec{n} + \vec{n} \times \vec{d} - \vec{n} \times (\vec{n} \times \vec{H}). \tag{2.71}$$

This can be used to find an expression for the magnetization $\vec{m}$ purely dependent on the Néel vector,

$$\chi^{-1}\vec{m} = \rho\vec{n} \times \dot{\vec{n}} - L\nabla\vec{n} - \vec{d} \times \vec{n} + \vec{n} \times (\vec{n} \times \vec{H}). \tag{2.72}$$

From equation 2.72 it is possible to draw some conclusions regarding the magnetization in the antiferromagnetic material. The first term of equation 2.72 expresses that in the absence

of DMI and an external field, there is no magnetization present when there are no dynamics in the Néel vector since $\dot{\vec{n}} = 0$. The DMI term $\vec{d} \times \vec{n}$ ensures a net magnetization of the system given that $\vec{d} \nparallel \vec{n}$. The third term can sometimes give a non-zero magnetization if the field is strong enough. Then it is possible to get what is known as a spin-flip transition when the spins align with the field direction, even when there is antiferromagnetic ordering at lower magnetic fields. At low fields, the exchange energy is dominant, so the material consists of opposing magnetization vectors, giving 0 or close to 0 magnetization.

The $L\nabla\vec{n}$ term might seem strange, as it states that the Néel order parameter induces a finite magnetization, even at equilibrium. It can be shown, however through the method of Hamilton's equations that the gradient of the magnetization can be written as

$$\nabla\vec{m} = -L\nabla^2\vec{n}. \tag{2.73}$$

When this enters the functional derivative of F with respect to $\vec{n}$, it leads to a rescaling of the exchange coupling, $A \to A - L^2$. In addition, it can be shown that the term interacts with the magnetic field on the form $F = -LH\nabla\vec{n}$. However, this gives a non-zero contribution in the equations of motion only when there is texture or time dependence in the magnetic field. It is, therefore, possible to omit L terms in further calculations, but note that the exchange coupling is rescaled. More on the details of this can be found in source [20].

By observing, equation 2.72 gives an explicit expression of the magnetization in terms of the Néel vector. This means that the Néel vector dynamics directly determine the dynamics of magnetization. This can be used to find a purely Néel vector expression for the dynamics of an antiferromagnet.

2.3.3 Purely Néel vector equation for dynamics

Going back to equation 2.60 and rewriting L_B and F with the expression found in equation 2.72 it is possible to reduce the Lagrangian density to expressions purely dependent on the Néel vector $\vec{n}$ and its time derivative $\dot{\vec{n}}$. By inserting the relation and doing some algebraic work, one can arrive at

$$\begin{aligned} L_B[\vec{n}] &= \frac{\chi\rho^2}{2}\dot{\vec{n}}^2 - \chi\rho\dot{\vec{n}} \cdot \vec{H} \times \vec{n} \\ F[\vec{n}] &= -\frac{\tilde{K}}{2}(\vec{n} \cdot \hat{r})^2 + \frac{A}{2}|\nabla\vec{n}|^2 + \frac{\chi}{2}(\vec{H} \cdot \vec{n})^2 - d\chi \cdot (\hat{r} \times \vec{n}) + D\vec{n} \cdot (\nabla \times \vec{n}). \end{aligned} \tag{2.74}$$

Here the amplitude of the DMI vector $\vec{d}$ has been pulled out to yield a term on the form $d_\chi \cdot (\hat{r} \times \vec{n})$. d_χ is then the homogeneous DMI amplitude. Once again, the equations of motion can be found by minimizing the total Lagrangian. By imposing the constraint that the length

of $\vec{n}$ is conserved ($|\vec{n}|^2 = 1$) the Lagrange equation takes on a Lagrangian multiplier term and changes from $L - F$ in equation 2.74 to $L - F - \lambda(|\vec{n}|^2 - 1)$. Where λ is a Lagrangian multiplier, which is not of interest here. The Lagrangian yields the following equation,

$$\frac{\partial \mathcal{L}}{\partial \vec{n}} + \frac{\partial(\lambda(|\vec{n}|^2 - 1))}{\partial \vec{n}} - \left(\nabla \frac{\partial \mathcal{L}}{\partial \nabla \vec{n}} - \partial_t \frac{\partial \mathcal{L}}{\partial \dot{\vec{n}}}\right) = 0. \tag{2.75}$$

The derivative of the constraint is a function of the vector $\vec{n}$. Therefore, by taking the cross product of the equation with $\vec{n}$ the constraint term vanishes since $\vec{n} \times \vec{n} = 0$ and a new way to determine the dynamical equations is recovered without the constraint

$$\vec{n} \times \left(\frac{\partial \mathcal{L}}{\partial \vec{n}} - \partial_t \frac{\partial \mathcal{L}}{\partial \dot{\vec{n}}}\right) = 0. \tag{2.76}$$

Using L_B and F from equation 2.74 and performing the derivatives yield

$$\begin{aligned} \vec{n} \times \Bigg[& \ddot{\vec{n}} + \frac{A}{\chi \rho^2} \nabla^2 \vec{n} + \frac{2}{\rho} \dot{\vec{n}} \times \vec{H} - \frac{\tilde{K}}{2\chi\rho^2} (\vec{n} \cdot \hat{r}) \hat{r} \\ & + \frac{1}{2\rho^2} (\vec{H} \cdot \vec{n}) - \frac{d_\chi}{\chi \rho^2} \vec{n} \times \hat{r} + \frac{2D}{\chi \rho^2} \nabla \times \vec{n} \Bigg] = 0. \end{aligned} \tag{2.77}$$

Then an equation for the Néel vector order parameter was recovered. It is useful to note that the equation holds $\ddot{\vec{n}}$. As mentioned in the introduction, one of the main advantages of antiferromagnetic spintronics is the possibility of fast switching. One of the reasons behind this is the $\ddot{n}$ term in the equation of motion. Since there is effectively an acceleration present, it is possible to draw links to Newton's equations of motion and to define some form of inertial effect in antiferromagnetic systems. This term is believed to lead to a higher resonance frequency and possibly faster switching and are unique to antiferromagnetic systems, as opposed to other magnetic systems. Equation 2.77 is used in section 5 later in the text.

2.3.4 Temperature

Now that the basics of an antiferromagnet and the LLG(S) equation have been found, a brief derivation to the inclusion of temperature in the model is included. This derivation follows source [21] and [22]. Temperature enters the effective field through a random isotropic field $\vec{h}(T)$ with a variance ν^2. The details of this assumption are not within this thesis's scope, but details can be found in source [23]. Since $\vec{h}(T)$ is a random thermal field, it can be expressed in terms of a Wiener process,

$$\vec{h}(T)dt = \nu d\vec{W}(t). \tag{2.78}$$

Where $\vec{W}(t)$ is the isotropic Wiener vector. Following a stochastic calculus derivation and by the fluctuation-dissipation theorem, it is possible to arrive at the value for ν at thermal

equilibrium,

$$\nu = \sqrt{\frac{2\alpha K_b T}{\mu_0 M_s^2 V}}. \tag{2.79}$$

Where K_bT is the thermal energy, α is the Gilbert damping, μ_0 is the magnetic permetivity, M_s is the saturation magnetization and V is the volume. The statistical properties of this field can be found from Brown and Kubos analysis [23] [24] and can be expressed,

$$\begin{aligned} \langle \vec{H}_{T,i}(t) \rangle &= 0 \\ \langle \vec{H}_{T,i}(t) \vec{H}_{T,i}(t+\tau) \rangle &= \frac{2K_b T\alpha}{\gamma \mu_0^2 M_s V} \delta_{ij} \delta(\tau). \end{aligned} \tag{2.80}$$

That is, the thermal noise is uncorrelated in both space and time. In order to use this model for temperature numerically, it has to be discretized in time. Following the normalization used later, $t' = \gamma \mu_0 M_s t$, the standard deviation becomes [22]

$$\sigma = \sqrt{\frac{2\alpha K_b T}{\mu_0 M_s^2 V}} \sqrt{\frac{\Delta t'}{\gamma \mu_0 M_s}}. \tag{2.81}$$

Here $\Delta t'$ is the time step of the numerical method. Then the normalized thermal field can be expressed as

$$\vec{h}_T \Delta t' = \sigma \xi_t. \tag{2.82}$$

Where $\xi_t = N(0,1)$ a normalized Gaussian draw. Therefore, the effective thermal field can be viewed as a Gaussian draw at each time step with a mean of zero and variance of one multiplied to a factor σ.

To summarize, the free energy of an antiferromagnet was found. Given that the equations of motion produce six different equations (1 for each direction for both $\vec{m}$ and $\vec{n}$) and that the Néel vector and magnetization essentially describe the same phenomena, one has quite a lot of freedom in how you describe the dynamics in the material. Each method is in itself valuable and will come in handy later.

2.4 Topological Charge

Topological charges are a phenomenon that appears in magnetics. They are excellent candidates for transport in, for example, neuromorphic computing as they are very insensitive to perturbations. Topological charges will be highly relevant later in this text, so in order to understand them, a brief overview of topological charges is presented here.

Two states are topologically invariant if it is impossible to continuously deform them into each other without passing an infinite energy barrier. Another way to view this is that an excitation in the local order parameter $\vec{n}$ is a particle-like state. Now there are two kinds of such excitations or quasi-particles. Those who are deformable to the system's ground state and those who are not. A topological charge is a number classifying this deformability. In this subsection, the intuition behind this phenomenon is explained, before a brief dive into the governing mathematics is presented.

In order to concretize the above point, consider a 1D antiferromagnet parameterized by the Néel vector angle to the x axis ϕ. An easy-axis anisotropy is present in the system, so the Néel vector has minimized energy at either $\phi = 0$ or $\phi = \pi$. Further, consider two magnetic structures a and b, one with the borders in the same ground state and one with the borders at different ground states.

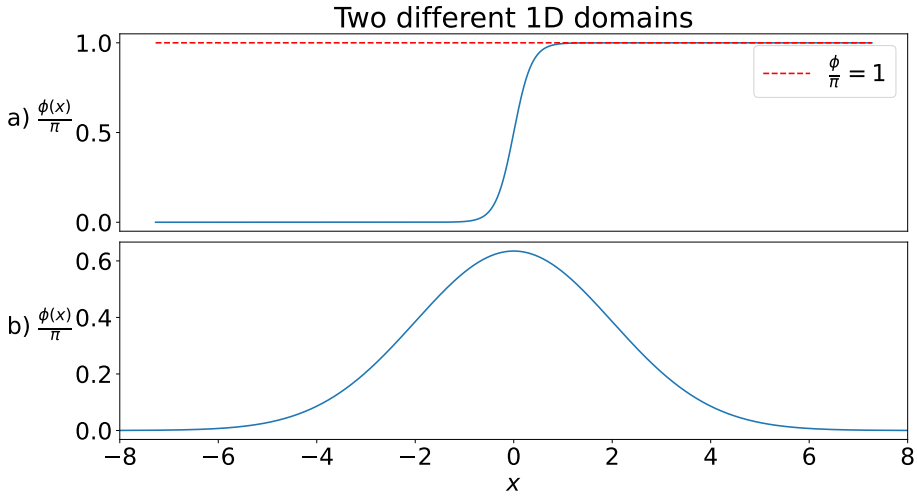

Figure 2.1: The figure shows two different 1D domains normalized by a factor of π. a has borders fixed at $x = \pm\infty$ as $\phi = 0$ and b has borders $x = \pm\infty$ at $\phi(-\infty) = 0$ and $\phi(\infty) = \pi$.

State a in figure 2.1 can not be changed to the ground state by locally and slowly turning the Néel vector. However much you change the Néel vector direction ϕ state a will never

be transformable to the ground state by a finite operation. Locally flipping spins in state a only widens, narrows or moves the magnetic structure. State b, however, can locally turn the Néel vector direction so that $\phi = 0$ everywhere by a finite operation. Therefore state a and b are inherently different. A number can be found to classify the difference(more on finding the number later). This is the concept of topological charge(also referred to as topological number or winding number). State a is said to be a topological domain with a non-zero topological charge, and state b is a non-topological domain with zero topological charge. This can also be seen when mapping the two states onto a Bloch sphere. b forms a closed loop since it starts and ends at $\phi = 0$ and a does not form a loop.

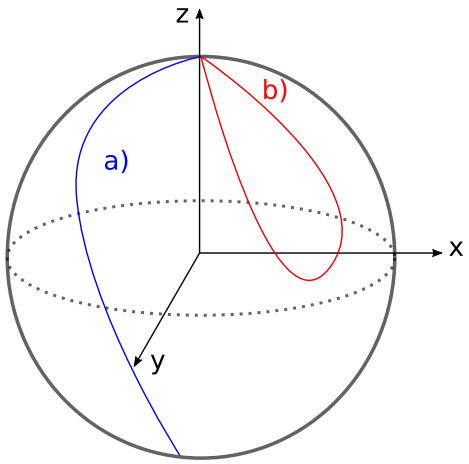

Figure 2.2: The figure shows the same states as in figure 2.1 mapped onto a Bloch sphere. The topological state is a) and the non-topological state is b).

It is impossible to perform a continuous deformation of an open loop down to a point, and thus domain a in figure 2.2 is topologically "protected". This is mathematically equivalent to stating that state a has a non-zero topological charge where state b topological charge number of zero [25]. It is possible to see from figure 2.2 that there is no finite way to deform the path a onto the point $(x, y) = (0, 0)$.

So qualitatively, a topological charge is a topological number classifying topologically stable domains of a magnetic system. It is a quasi-particle, and is not to be confused with an electrostatic charge. In reality, it is a stable winding of the order parameter and not a charge. It can lead to stable structures which are not necessarily energy minima, for example, state a in figure 2.1 will have finite exchange energy. They are stable under perturbation and need infinite energy barriers to deform them to the ground state, at least in the ideal continuous approximation of a real system. Topological charges are defined more mathematical as well, which is shown below.

2.4.1 Mathematical Description of Topological Charge

This part is meant to give a more rigorous description of the topological charge of a magnetic structure. It follows the method of source [26]. However, it is attempted to do so without going deep into quantum mechanics or topology. A more thorough description can be found in "Introduction to Topological Quantum Numbers" by D.J. Thouless [27] or in "Topology for Physicists" by Albert S. Scwarz [28].

The general idea behind the magnetic structure mapped onto a sphere in figure 2.2 can be defined with a more general mathematical mapping

$$f : S^n \to S^m. \tag{2.83}$$

That is the mapping from the real space n onto an m sphere, known as the "target" manifold. A topological "defect" exists when the mapping in equation 2.83 can not be contracted to a single point. This is known as the concept of homotopy. Two mappings, f and g, are homotopically equal if they can be contracted continuously into each other. Every f and g that are homotopically equal (i.e. every mapping that can be deformed into each other) form a group denoted as

$$\pi_n(S^m). \tag{2.84}$$

A topological defect exists when this mapping is non-zero. This is equivalent to the mapping being different from identity, which in the antiferromagnetic case is the uniform Néel vector state

$$\pi_n(S^m) \neq 0. \tag{2.85}$$

Now that it has been defined what a topological defect is, it useful to define a number or characteristic that can be used to classify the defect or group. Here is where the winding number or topological charge comes in handy. The winding number essentially counts how often m is wrapped around n during f. For a point P, that number can be found by counting how many times points x_k maps onto themselves under the transformation. This weighted sum can then be written as

$$\deg f = \sum_{x_k \in f^{-1}(P)} \operatorname{sgn} D(x_k). \tag{2.86}$$

Where D is the Jacobian of the mapping and sgn is the signum function, which returns the sign of a real number. It is not proven here, but it can be shown that this degree is invariant under the choice of point P. Since equation 2.86 is an integer, it is invariant under continuous deformation of f. This is then the wanted topological number to classify the homotopy.

Consider now the mapping from n to n, $f : \mathbb{R}^n \to \mathbb{R}^n$. This is specifically relevant for the magnetization structures in question here. Rewriting the sum of equation 2.86 to an integral with a δ function allows for a further simplification of equation 2.86

$$\deg f = \int d^n x D(x) \delta(f(x) - P). \tag{2.87}$$

The above result can be expressed in a coordinate free form as [26]

$$\deg f = \frac{\int_M f^* \Omega}{\int_N \Omega}. \tag{2.88}$$

Ω is just a metric making the integral 2.88 equivalent to the sum above. This can finally be used to classify some real magnetization systems. Starting from a soliton (one dimensional domain wall with topological charge ± 1), which is important later in this text. When going to the Néel vector angle description, which can be used in an easy plane 1D antiferromagnet. df^i can then be replaced by $\partial_x \phi dx$. The assumption here is that the magnetization is a smooth function without any singularity. One can define a map from the infinite 1D chain onto a sphere (via stereographical projection [26]). Then it is finally possible to obtain the topological charge number or the soliton winding number,

$$w = \frac{1}{2\pi} \int_{-\infty}^{\infty} dx \partial_x \phi. \tag{2.89}$$

In essence this counts the number of windings in the easy plane from $x = -\infty$ to $x = \infty$. Note that the derivation above holds for mappings from n spheres to n spheres. Similarly, the 2D topological charge (skyrmion number) can be defined as

$$Q = \frac{1}{4\pi} \int dx dy \vec{M} \cdot \left(\frac{\partial \vec{M}}{\partial x} \times \frac{\partial \vec{M}}{\partial y} \right). \tag{2.90}$$

Skyrmions are two-dimensional stable topological structures. Now the topological number Q is conserved and takes integers or half integer values. If Q is to take a whole constant number no matter the fine structure of the magnetic system then the integrand has to have a conservation law [29].

$$\partial_t \rho - \nabla j = 0 \tag{2.91}$$

Using the normalized Néel order parameter for a one dimensional antiferromagnet ($\vec{n} = (\cos\phi, \sin\phi)$), the following relation holds

$$\begin{aligned} \rho &= -\partial_x \phi / \pi \\ j &= \partial_t \phi / \pi. \end{aligned} \tag{2.92}$$

There is no mathematical need for a topological stability to have energetic stability, and they are two different animals. In topological terms, the energy needed to lift such a barrier

is infinite. This is analogous to the fact that it is not possible to deform a torus to a sphere without rupturing the torus. In a real physical system, there is always finite energy, not infinite, needed to lift such a domain wall barrier since realistic systems are neither infinite nor genuinely continuous. The discretization of the lattice break the infinite energy barrier [28]. Secondly, experimental setups are, in reality, always finite, so the topological charge of, for example, a 1D nanowire can always propagate out of the system. Lastly, the anisotropy constraining the system is always finite. So if one were to, for example, look at domain walls in a 1d wire and find the topological charge of a domain wall it is always only stable under the restriction of the anisotropic constant that constrains the order parameter to the easy plane. Such a constraint can always be broken by heating the material, inserting a strong external field, or other energetic contributions. The concept of topological charge still possesses interesting aspects since it leads to states that are not necessarily energetically stable, but stable nevertheless. Therefore, they make ideal candidates for magnetic signal propagators.

3 The basics of Neuromorphic Computing

The fastest supercomputer in the world is Fugako in Japan operating at 442 petaflops(floating point operations per second) at around 30000 kW. The human brain is however estimated to operate at around 1 exaflop, with a mere 15 watts [30]. That means the flop to watt ratio for the most powerful supercomputer in the world is $14.7e9\frac{\text{flops}}{W}$ compared to the human brain that has an estimated rate of $6.67e16\frac{\text{flops}}{W}$. Neuromorphic computing is a concept within computer science to take advantage of the massive flop to power ratio advantage the brain has through designing brain inspired computer components.

The most used computer architecture in use in the world today is known as the Von Neumann architecture. It is credited to John Von Neumann in the paper "First Draft of a Report on the EDVAC" from 1945 [31]. It proposes a basis in logical computer based on a separation of memory and processing and uses a so called stored programming basis. Although the ideas of Von Neumann has proven very successful in the years since, there are limitations to the Von Neumann architecture which severely limits the speed of calculations. The key bottleneck being that in this architecture paradigm, the processing and memory are separated. The speed of a computer built on the Von Neumann architecture will therefore always be limited by the speed of which memory transfer is possible. This is known as the Von Neumann bottleneck. Often, the speed of such a computer is limited to this transfer speed, rather than the actual computation. In the brain, the structure differs to that of a conventional computer. Rather than the processing and memory separation, it has a nodal structure where the memory and processing are located at the same place. Therefore, the brain essentially bypasses the Von Neumann bottleneck. Therefore, designing neuromorphic chips may lead to an increase in speed and efficiency in computers.

In addition to the possibility of raw speed-up that was discussed in the previous paragraph, there are other advantages. Machine learning and artificial intelligence are becoming more important as each day passes. For now, these computations uses conventional architecture to run brain inspired algorithms. By having the architecture closer and more compatible it is believed that neuromorphic computing can cause significant speed up in cognitive tasks, such as image classification or word recognition [32]. Therefore, by designing neuromorphic chips, one could possibly outperform both the energy consumption and speed of conventional computers.

It is however quite difficult to incorporate these ideas into conventional computer components and CMOS logic. In order to do so, one needs dozens of transistors for each neuron, in addition to extra memory to mimic the synapses of the brain. Therefore, the area of regular

CMOS based neuromorphic chips are too large and inefficient [33]. Using alternative technologies might be the answer, spintronics for example. In order to incorporate neuromorphic systems using spintronics, an understanding of neuromorphic computing is needed. In this section, a brief introduction to the topic, an introduction to regular neural networks and the spiking neural network is presented, which will be used later when looking at schemes for implementing spintronic neuromorphic systems.

3.1 Conventional vs. Neuromorphic computation

Before expanding on neuromorphic systems, a brief explanation of the differences of the concepts is presented, to further clarify the difference of the two.

3.1.1 Processing and data

Firstly, the general processing and data structure differs in the differing types of systems. The data in a regular computers are stored as bytes. 0s and 1s are passed into the CPU, where code is run through binary instructions. The output is also a binary signal. The processing runs in a global clock. Meaning that operations happen at a specified frequency, the clock frequency. In neuromorphic systems, the firing of neurons happen asynchronously without a global clock frequency. The data in neuromorphic systems are spiking signals, for example time dependant current spikes. The resulting output are also time dependant signals.

3.1.2 Operational differences

In addition to the above mentioned points, there are fundamental operational differences. Firstly, neuromorphic systems are highly parallel by design. In a conventional computer, processing happens sequentially, while in theory all neurons and synapses can fire simultaneously in a neuromorphic system. The single operation complexity of a neuron is however of a simpler nature than in a parallelized Von Neumann architecture. Secondly, neuromorphic chips are inherently scalable in theory. Meaning, it is possible to view multiple neuromorphic chips as just a larger collection of synapses and neurons. This means it is possible to run larger and larger networks. This has been shown in some large-scale neuromorphic chips that have been made with conventional technology to date, such as SpiNNaker [34] or Loihi [35]. Neuromorphic chips also use event-driven asynchronous computation, opposed to the sequentially synchronous computation in a regular computer. That is, the neurons and synapses are essentially idle when there are no signal incoming and only "turn on" when there is an incident signal. This leads to sparsity in active neurons and possibly energy efficiency.

3.2 Neurons and synapses

In order to make artificial neuromorphic components, it is first important to understand how the basic signal propagation and calculation work in an actual brain. The key components to understand for neuromorphic applications are neurons and synapses. In essence, the neurons act as storage and processing devices and synapses as weight and signal transfer. In order to

gain some insight in to how these can be exploited in neuromorphic computing architectures, they are briefly explained here.

The neuron can be divided into three parts, called dendrites, soma and axon. For now, they can be thought of as input, processing and output. The dendrites, shown schematically in figure 3.1 collect signals from other neurons. In some cases, over 1000 interconnections can be present in a single neuron. After the signal has passed through each individual dendrite, they are individually passed to the soma. If the soma receives a significant enough input within a given timeframe, the soma spikes, producing a small voltage pulse at $\sim 100\,\text{mV}$ with a duration of $\sim 1-2\text{ms}$ [36]. An essential point here is that the incoming signals need to be close in time in order for a spike to be produced. If the neuron spikes, the signal is passed to the axon and through to neighbouring neuron's dendrites. The form of the incident pulse does not matter, it is rather the frequency and amplitude in the incoming signals which determines spike probability. At each neuron interconnect, synapses either down-scale or up-scale the signal amplitude with some weight Δw. Often, in two neuron structures, the first neuron is called the presynaptic neuron and the latter the postsynaptic neuron. The neuronal and synaptic structure can be seen in figure 3.1.

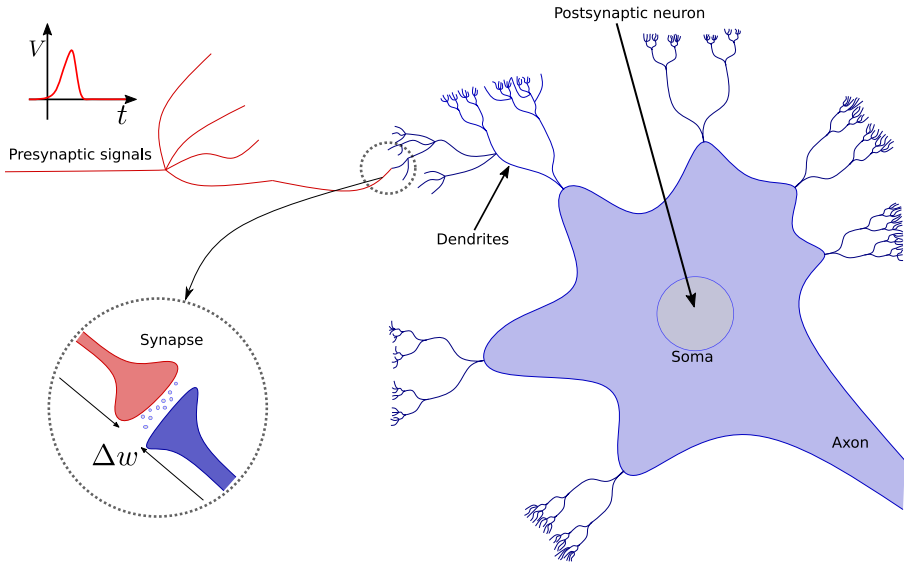

Figure 3.1: The figure shows the general structure of the neuron and synapse. The signals arrive at the synapse from the presynaptic branches. Signals are passed through the synapses and into the postsynaptic neuron. Δw denotes the weighting of the synapse. The presynaptic signals carry a spiking electric potential.

The interconnects between different neurons are known as synapses. A synapse can send signals either as a chemical messenger or as an electrical messenger. As mentioned, a synapse is able to either scale up or down the signal it gets from a neuron through adjusting the amount of neurotransmitter it releases. This makes it essential for learning and memory purposes, as adjustability of weight is necessary to train networks, both artificial and natural. The phenomenon that a synapse can strengthen or weaken the incoming signal is known as synaptic plasticity. In artificial neuromorphic components, the synaptic weight can be adjusted manually. In the actual brain, however, the method for adjustability is still under debate. One of the most general theories is that casual firing increases the synaptic weight. That is, if the presynaptic neuron fires, and the post synaptic neuron fires as a consequence it causes an increase in the synaptic weight Δw [37]. The dynamics of the brain are similar to those of a neural network, which is important for neuromorphic applications. Under a brief introduction to such networks are presented.

3.3 The basics of neural networks

Neural networks are mathematical structures that function quite similarly as biological neurons and synapses. In the basic neural network, nodes (neurons) are arranged in layers and are adjustable with some weight (synapses) w. To encapsulate the spiking potential the incoming signals are usually activated through some function, for example, the ReLu function (rectified linear units $f(x) = x^+ = \max(0, x)$) or the Sigmoid function ($S(x) = \frac{1}{1+e^{-x}}$). There are however some differences between the biological neurons and synapses and conventional neural networks. Conventional neural networks have no time dependence, and the nodes do not contain the leaky integrate and fire dynamic that biological neurons have.

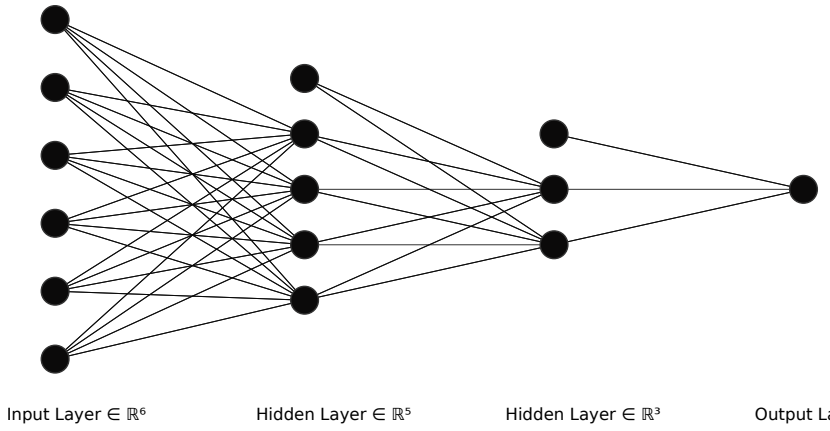

Figure 3.2: The figure shows a basic feed forward neural network with 6 input nodes that performs classification with one output node and bias layers in each of the two hidden layers.

The basic principle is to take some input, shown in the input layer in figure 3.2. Each node connects to every node in the next layer with a weight which classifies the input "strength" of the next layer. Additionally, a bias node is passed to each layer (shown as the upmost node of each layer in figure 3.2). The weights are random at first, but are trained through optimizing a cost function through a training procedure, for example gradient descent. What it does is to find the specific combination of weights that minimizes the cost function(at least locally). Then each set of inputs can give a classification or value for the output by passing the input values through the network. There are many methods of distributing nodes and procedures within the field of neural networks. To name a few, feed forward networks and recurrent neural networks. Figure 3.2 is a basic feed forward network. They are the easiest to understand directly. They can be analytically as well as shown below.

3.3.1 Function description of a four layer neural network

Mathematically speaking it is possible to define the three layer network shown in figure 3.2 as

$$\hat{y}_o = \phi_0(\gamma_{h_2} + \sum_{m=1}^{2} \gamma_{mh_2}\phi_{h2}(\beta_{0h_1} + \sum_{j=1}^{4} \beta_{jh_1}\phi_{h1}(\alpha_{i0} + \sum_{i=1}^{5} \alpha_{ih_1}x_i))). \tag{3.1}$$

Here each ϕ (for example ReLu or Sigmoid functions) is the activation function of each layer, x_i are the inputs, β, γ and α are the adjustable weights, and $\hat{y}_o$ is the predicted output. Equation 3.1 shows how the neural network $\hat{y}_o$ from the original input signals/layer x_i. The network is of course not precise in its predictions at first, and the error can be quantified in a so-called loss function. There are multiple ways of defining a loss function. The simplest way is to define the function as the mean squared deviation from the real values in the predicted results, for the regression problem it becomes

$$J(w) = \frac{1}{n}\sum_{i=1}^{n}(y_i - \hat{y}_i(x_i))^2. \tag{3.2}$$

Here, y_i is the real observed value. Now the goal is to minimize the function in equation 3.2 by adjusting the set of weights w defined by the setup, and by doing so “training” the network to properly predict on data. One of the most used methods in neural networks is what is known as gradient descent.

The algorithm is shown here to give an example of a training procedure,

1. Let $t = 0$ and denote the current weights as $w^{(t)}$.
2. Do the following until the finding a minima:
   (a) Calculate the predictions $\hat{y}_0(x_i)$
   (b) Find the loss function(equation 3.2) $J(w^t)$
   (c) Find the gradient of the loss function for the current weights and evaluate at the weights w^t, $\nabla J(w) = \frac{\partial}{\partial w}(w^{(t)})$
   (d) Go in the direction of the negative gradient with some step length λ
   $$w^{t+1} = w^t - \lambda \nabla J(w^t). \tag{3.3}$$
   (e) Set $t \to t + 1$.
3. The final values are the ones used for new predictions.

Now of course this algorithm does not ensure that the point in the loss function that is found is the global minima. It might also be a local minima. Therefore, the learning rate λ can be quite important in the accuracy of the prediction and becomes an important tuning parameter often chosen to minimize the test error. It is also evident that it is very heavy computationally speaking, as finding gradients of a function of multiple variables (sometimes thousands of weights) is tedious. This does not however mimic the brain perfectly as the brain uses time dependant signals to decide when to fire, not static as the regular neural network does. This is where spiking neural networks come in. In addition, time dependant neural networks can use different training rules, for example spike time dependant plasticity(more on this later) that extensively reduces the computational complexity of minimizing the loss.

3.4 Extension to time dependant spiking neural networks

A spiking neural network is a network using the ideas from a regular neural network, but incorporating time dependence. SNNs(spiking neural networks) operate using spikes which are discrete events in time, differing largely from the regular neural network structure as that uses static values. The difference is that when the nodes reach a certain threshold, it spikes rather than giving a specific continuous output [38]. The nodes in the next layers then receive a series of time dependant spikes and send out their own spikes accordingly. Referencing figure 3.3 the nodes or neurons Σ can be thought of as a leaky integrate and

fire unit that takes inputs x_i multiplied with weights w_i, sums them if they are close enough in time and fires if the summation reaches some threshold resulting in a spiking output y_i. The use of these networks are specifically useful when for example analysing time dependant sensory data. It also gets the artificial neural network closer to the actual brain. There exists several classical computer concepts incorporating this into hardware, for example the true north chip made by IBM. The problem with these types of structures is that they are too energy dense and take too large of an area. Figure 3.3 shows a general structure of a single spiking neuron with n inputs.

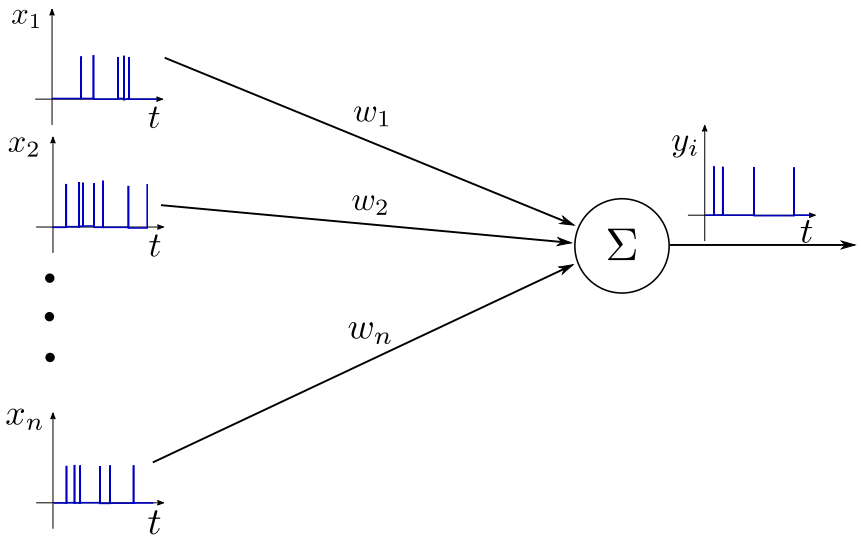

Figure 3.3: The figure shows a spiking neural network with n input nodes and one output node. The incoming spiking signals x_i are amplified by some weight w_i and enter the leaky integrate and fire unit Σ which produces a time dependant signal y_i.

3.4.1 Advantages and Disadvantages of spiking neural networks

There are two main challenges with spiking neural networks. Firstly, there is no particularly good way of training the networks, as many of the highly optimized training methods of regular neural networks are unsuitable for time dependant signals. The aforementioned gradient descent for example is not particularly useful for SNNs. The other challenge is mostly within hardware implementations of SNNs. It is as of now very energy costly to build SNNs, with the usual transistor based components. There are also quite a few advantages, it is believed that SNNs might prove to be faster than a regular network, it is useful since it is able to continue training when it is in use, and they are believed to reach good accuracy for fewer neurons than the traditional neural net.

3.4.2 Training spiking neural networks with a STDP scheme

As mentioned previously, one of the difficult challenges when it comes to spiking neural networks is the training of the network itself. There are some methods in use today, but none as optimized as the regular neural network models are. Later in this text, when a spintronic spiking neural network is presented, a method called Spike-timing-dependant-plasticity (STDP) is used. STDP is a form of Hebbian learning, which means that connections are strengthened when stimulus is repeated and casual [37]. This is an essential idea when modelling the brain in neuroscience as well. Although the actual training of biological neurons is highly debated, this is still one of the largest theories in use. There are other methods as well in use to train spiking neural networks, but the STDP model gives an example of a possible solution.

Denoting the weight change at synapse j as Δw_j and the time for each presynaptic spike as t_j^f. In the same manner, denote the postsynaptic neuron firing times as t_i^n. The general idea in STDP learning model is that the weight is adjusted as some function of the relative time, $\delta t = t_i^n - t_j^f$

$$\Delta w_j = \sum_{f=1}^{N} \sum_{n=1}^{N} W(t_i^n - t_j^f). \tag{3.4}$$

Here $W(\delta t)$ denotes a STDP weighting function. There are several choices for W, but this is one of the most common ones [39]

$$\begin{aligned} W(t) &= A_+ e^{-\frac{t}{\tau_+}}, t > 0 \\ W(t) &= A_- e^{\frac{t}{\tau_-}}, t < 0. \end{aligned} \tag{3.5}$$

Here A_+ and A_- can be a function of the current synaptic weight(A_- is usually negative). $\tau_{+/-}$ is usually in the order of 10 ms. If a spike arrives after the neuron has fired at the current level of the weight will be reduced causing lowering of the weight, and if the spike arriving at the neuron before the relative firing, the synaptic weight will increase. In artificial systems, there is a possibility of actually choosing the activation functions at will by tuning parameters.

So to summarize, neurons and synapses are the main interest when implementing neuromorphic hardware. They can be thought of as a processing unit and an adjustable weight. In this project, the main interest of neuromorphic computing is hardware implementations of spiking neural networks(SNNs). Spiking neural networks work similarly to a conventional neural network, but incorporates, like the brain, time dependant signals.

4 Topological charge based neuromorphics with antiferromagnets

A possible scheme incorporating artificial neurons and synapses are proposed by Shu Zhang and Yaroslav Tserkovnyak in "Antiferromagnet-Based Neuromorphics Using Dynamics of Topological Charges" [40]. The paper proposes a possible scheme for an artificial spiking neural network using antiferromagnets and the dynamics of topological charges. Now that the basis for such a network has been established in the previous sections, it is finally possible to explore an implementation of one. Previous papers in antiferromagnet neuromorphics have implemented artificial neurons, but the entire network is a new step in the right direction of realising an antiferromagnet SNN experimentally [41]. The article aims to do so through previously established antiferromagnetic concepts such as spin valves and spin wave dynamics. In this section, a re-derivation of the results of the article is presented and the theoretical antiferromagnetic spiking neural network is explored.

4.1 Setup of antiferromagnetic neuromorphic components

In order to mimic a spiking neural network there are a few components that need to be present. Firstly there needs to be some method for transporting signals, similar to the purpose of dendrites in the brain. In this scheme this is envisioned with one dimensional wires transporting topological charges through the network. There is also a need for a neuron type structure incorporating a leaky integrate and fire scheme in order for the network to function properly as a spiking neural network. Here a one domain antiferromagnet with a slower relaxation time than the incoming rate of topological charges is believed to incorporate the leaky integrate and fire property. The synapse proposed is a one dimensional nanostrip containing a large number of topological charges that releases when they are perturbed by a passing signal. So to summarize signals propagate along one dimensional wires, perturb the synapse so that it amplifies the signal and then the phase flip of the local order parameter in the neuron determines whether the signal continues to propagate. This setup is shown in figure 4.1.

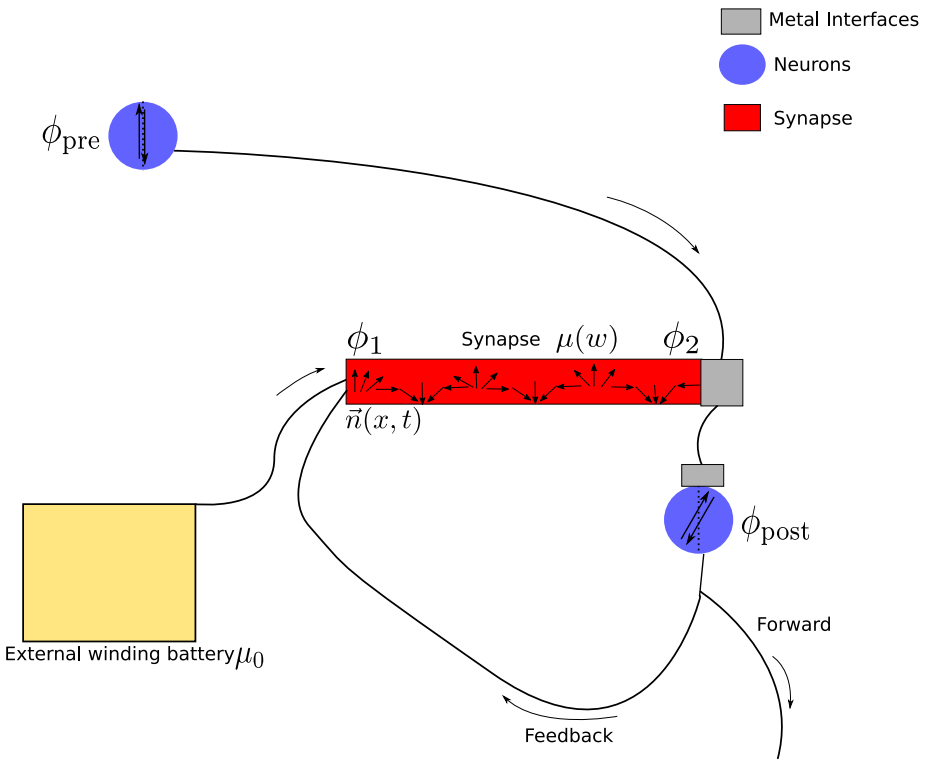

Figure 4.1: The figure shows a simple two neuron structure with the synaptic structure included. The external winding battery holds a chemical potential μ_0, the order parameters $\phi_{1,2}$ denote the chemical potential at each end of the synaptic strip, $\phi_{pre/post}$ denotes the order parameters of the neuron before and after the synapse. The synapse shows the winding order parameter and contains a chemical potential $\mu < \mu_0$ dependent on the density of topological charge w. The feedback and forward loops are also included, to show the structure needed to train the network. An external winding battery is connected to the synapse to provide a source of topological charge. The order parameter of the synapse $\vec{n}(x,t)$ is shown winding in the synapse.

Since the neuronal order parameter $\phi_{pre/post}$ is a one domain antiferromagnet the order parameter varies collectively across the state. As mentioned the synapse can be thought of as a "storage" of topological charge. In order to adjust the synaptic weight a loop is connected from the postsynaptic neuron to allow for insertion of winding, in addition an external winding "battery" is connected to the left end of the synapse in figure 4.1. Metal spacers separate charge carriers, neurons and synapses. In order to understand how this setup works more than schematically, an investigation into the governing physics is presented in the following subsections.

4.2 Antiferromagnetic topological charge carriers

In order to transport topological charge along the one dimensional wire, it is first necessary to figure out how a possible topological texture will look in this specific system. In the system proposed, there is a hard axis anisotropy imposed out of the xy plane. When the anisotropic z component K_z becomes significantly larger than other anisotropic constants, $K_z \gg K$ the Néel vector can be viewed as an effective 2d vector. The Néel vector dynamics in the z direction are so small that the system can be viewed as two-dimensional. The normalized Néel order parameter is to reiterate $(\vec{m}_a - \vec{m}_b)/M_s$ where M_s is the saturation magnetization. Since the order parameter has been constrained to a two-dimensional plane, the Néel vector can be written as $\vec{n} = (\cos\phi, \sin\phi)$. Here, the angle ϕ is the angle between the x axis and the Néel vector. The dynamics of the Néel vector is then fully parameterized by the in plane angle ϕ. ϕ is a function of both the position in the one dimensional wire x and the current time t, $\phi \to \phi(x,t)$. It is already possible to recognize a topological conservation law for the winding number, as the order parameter is a function with fixed borders and no discontinuities. This law takes the form of equation 2.91

$$\partial_t \rho + \partial_x j = 0. \tag{4.1}$$

This is possible to do even before accounting for the free energy of the system as it is due to the fact that the Néel vector is a smooth function, and the geometry of the system. For further clarification, see section 2.4.

From equation 2.60 the free energy density f is made up of DMI, exchange interactions and anisotropic interactions. In this section, DMI and external magnetic field terms are ignored. Rewriting the free energy density in terms of the angle ϕ and simplifying it becomes

$$\begin{aligned} f[\vec{m},\vec{n}] &= \frac{\vec{m}^2}{2\chi} - \frac{K}{2}(\vec{n}\cdot\hat{r})^2 + \frac{A}{2}|\nabla\vec{n}|^2 + \vec{d}\cdot(\vec{m}\times\vec{n}) - \vec{H}\cdot\vec{m} - 2Dm\cdot(\nabla\times\vec{m}) \\ f[\vec{m},\vec{n}] &= \frac{\vec{m}^2}{2\chi} + \frac{A}{2}(\partial_x\phi)^2 + \frac{\kappa}{2}\sin^2(\phi). \end{aligned} \tag{4.2}$$

Here the ∇ term has been written out for the x direction, the direction of the one dimensional wire. The $\vec{m}^2$ term arises from the exchange energy, and the $\frac{\kappa}{2}$ term represents an in plane axial anisotropy with $\kappa > 0$ along the y axis. The free energy is minimized when there is perfect antiferromagnetic order, i.e. $\vec{m}^2 = 0$, $\partial_x\phi = 0$ and the azimuthal angle lies in the easy axis ($\sin\phi = 0$). This leaves the ground state as either a uniform angle $\phi = 0$ or $\phi = N\pi$.

As mentioned previously, the goal here is to propagate topologically stable domain walls along the artificial dendrites in the system. A topologically stable domain wall is as in figure 2.1 a state interpolating between two different ground state domains, i.e. from $\phi = N\pi$ to

$\phi = 0$ or vice versa. As a simplification, the domain wall is thought of as a singly interpolating domain wall (from zero to π or opposite). This type of domain wall possesses a topological charge carrying of either 1 or -1. This charge is found from the following integral

$$\zeta = \int dx\rho = \pm 1. \tag{4.3}$$

Where $\rho = -\partial_x\phi/\pi$. Writing equation 4.3 out it is possible to show that a domain wall interpolating 0 and π has a topological charge of ± 1

$$\zeta = \int dx\rho = \int dx - \partial_x\phi/\pi = -(\phi(\infty) - \phi(-\infty))/\pi = \pm 1. \tag{4.4}$$

Where the boundary values of ϕ are $\phi = \pi$ or $\phi = 0$. The integral in equation 4.3 would change borders for an experimental system, however, the result stands if there exists a domain wall between 0 and L, the length of the realized system. The sign in the answer designates the chirality, which way the order parameter winds around the x axis. The topological charge of a domain wall is a conserved quantity, therefore a domain wall moving through x_0 has to wind $\phi = \pi$, which is important later. The magnetic structure of topological charges are very stable and can be good signal carriers due to that stability. It is however important to understand their dynamical behaviour. In subsection 4.3, the static description used here is expanded to include dynamics.

4.3 Dynamics of propagating topological charges

As mentioned previously, the main interest now is to find an equation of motion for the topological charges. Before that, a brief explanation of how topological charges are inserted in the 1D wire is needed. The neuronal order parameter is as mentioned one domain antiferromagnet. Now a topological charge is created in the axom if the neuronal order parameter goes through a phase transition, i.e. φ, the neuronal order parameter winds by π. The effect of such a winding is to create a domain wall in the axom which can propagate to the next neuron. In addition to the neuronal signals, the synaptic strip is based on propagating topological charges. Therefore, the system bases itself purely on the flow of topological charge. The dynamical equations are therefore of great importance to this spiking neural network scheme.

The starting point for describing the motion is the Hamiltonian already found in equation 4.2. It is possible to define a damping function proportional to the Gilbert damping parameter α that was mentioned in section 2. A non-conservative force can enter the Hamilton formalism through a Rayleigh dissipation function of the form

$$R = (\alpha J/2)(\partial_t\phi)^2. \tag{4.5}$$

Where α is here Gilbert damping, J is the saturated spin density. With the Hamilton's equations formalism, the two dynamical equations are

$$\begin{aligned} \partial_t \phi &= \frac{\partial H}{\partial m} \\ \partial_t m &= -\frac{\partial H}{\partial \phi} - \frac{\partial R}{\partial(\partial_t \phi)}. \end{aligned} \tag{4.6}$$

Performing the derivatives yield

$$\begin{aligned} \partial_t \phi &= \frac{\vec{m}}{\chi} \\ \partial_t \vec{m} &= A\partial_x^2 \phi - \frac{\kappa}{2}\sin(2\phi) - \alpha J \partial_t \phi. \end{aligned} \tag{4.7}$$

Taking the time derivative of the first line of equation 4.7 yields $\partial_t^2 \phi = \frac{\partial_t m}{\chi}$ which can be used to eliminate any dependance on $\vec{m}$ in the second line of equation 4.7. By doing so this turns into the damped sine-gordon equation

$$\frac{1}{u^2}\partial_t^2 \phi - \partial_x^2 \phi + \frac{1}{2\lambda^2}\sin 2\phi + \beta \partial_t \phi = 0. \tag{4.8}$$

where $u = \sqrt{A/\chi}$, $\lambda = \sqrt{A/\kappa}$ and $\beta = \alpha J/A$. Here u is the spin wave speed and λ is the spin wave length. Both u and λ are proportional to the square root of the exchange coupling, which is expected as the speed is likely to increase with higher coupling causing more "reactive" neighbouring spins. It seems likely that a strong exchange coupling increases the length of the wave as a stronger coupling will cause each spin to couple more strongly to farther away spins weakening the effect of anisotropy. The anisotropy has the opposite effect on the wavelength, which also seems reasonable since the higher κ is the more energetically efficient there is to be in either $\phi = 0$ or $\phi = \pi$ so the free energy term will minimise when the transition is sharp. β is referred to as the damping factor, proportional to the Gilbert damping and inverse proportional to the exchange coupling. For $\beta \to 0$ the solution of 4.8 simplifies to

$$\frac{1}{u^2}\partial_t^2 \phi - \partial_x^2 \phi + \frac{1}{2\lambda^2}\sin 2\phi = 0. \tag{4.9}$$

Which is a regular sine-Gordon equation. In order to proceed, the variables can be transformed by $t \to \tilde{t}$ where $\tilde{t} = \frac{u}{\lambda}t$ and $x \to \tilde{x}$ where $\tilde{x} = \frac{1}{\lambda}x$. Equation 4.9 then becomes

$$\partial_{\tilde{t}}^2 \phi - \partial_{\tilde{x}}^2 \phi + \sin 2\phi = 0. \tag{4.10}$$

Once again a variable transformation can be used, $\xi = \tilde{x} - \tilde{v}\tilde{t}$. The propagating charges can be found by looking for travelling wave solutions $u(\xi) = u(\tilde{x} - \tilde{v}\tilde{t})$. The tilde variables are used here due to the transformation of x and t. Introducing ξ into equation 4.9 gives

$$(1 - \frac{1}{\tilde{v}^2})\partial_\xi^2 \phi = \sin(2\phi). \tag{4.11}$$

Now by integrating equation 4.11 after a multiplication of $\partial_\xi \phi$ this becomes

$$(\partial_\xi \phi)^2(1-\tilde{v}^2) = -\cos(2\phi) + c1. \tag{4.12}$$

For $\xi \to \pm\infty$, ϕ is known from previous considerations, it is either π or 0 when the topological charge is $\zeta = \pm 1$. In addition, the derivative of the moving frame $\partial_\xi \phi$ has to be 0 at the boundary since the boundary is fixed. From these facts it is possible to conclude that $c1 = 1$. It is then possible to integrate equation 4.12

$$\begin{aligned} \pm\frac{1}{\sqrt{1-\tilde{v}^2}}(\xi - \xi_0) &= 2\ln(\tan\phi/2) \\ \phi(x,t) &= 2\arctan\left[\exp\left\{\pm\frac{\xi-\xi_0}{\sqrt{1-\tilde{v}^2}}\right\}\right] \end{aligned} \tag{4.13}$$

Now it is possible to restore the previous variables into 4.13, setting $\xi_0 = 0$ and taking $\zeta = \pm 1$ as the topological charge. The term in the square root simply becomes v^2/u^2. When transforming the variables back to the initial state the final equation of motion becomes

$$\phi_0(x,t) = 2\arctan\left[\exp\left(\zeta\frac{x-vt}{\lambda\sqrt{1-v^2/u^2}}\right)\right]. \tag{4.14}$$

The solution of equation 4.14 is often referred to as a soliton [25]. A soliton is a solitary domain wall wave travelling at constant speed and amplitude. In this particular case, the topological charge is $\zeta = \pm 1$. When such charges are far apart, they do not interact significantly, and can be viewed as free particles. Again, it is possible to include a weak frictional force through an addition of $dH/dt = -2R$. Looking back to the wavelength, $\lambda = \sqrt{A/\kappa}$ it is possible to tune the wavelength through the anisotropic constant κ, so that the wavelength becomes small, and the solitons behave as a spike in the timeframe of the neuron. This discussion is simplified and the validity is also important to consider, therefore the next subsection takes a brief dive into the stability of the solitons.

4.3.1 Stability of topological charges

One of the main assumptions in the previous derivation of movement of topological charges was that the conservation law holds (equation 2.91), and that the Néel order parameter could be constrained in a plane. There are however some limitations to these assumptions. A topological charge has an infinite energy barrier in 2D in the continuum case(this is in fact not a continuum case as it is an approximation of a lattice model so the other "barriers" in the system are not infinite, just large), but as we have constrained our system into two dimensions rather than actually working in a real two-dimensional material the assumption of stable topological charges are only valid when the anisotropic energy κ_z is larger than

the other energy scales in the systems. It has to be overcome in order to break the phase. For example, when heating the material to such temperatures that the incident torque is of comparable size to κ_z thermally activated breakdown can occur. Therefore, it is crucial that the temperature both stays below the Néel temperature((the thermal limit in where an antiferromagnet becomes a paramagnet) and that κ_z is large enough to keep the z dynamics thermally inactive. It is also crucial that the density of domain walls stay below the Landau criterion for stability $\rho \ll 1/\sqrt{A/\kappa_z}$ [42].

4.4 Antiferromagnetic neurons

Now that the dynamics of topological charges have been established, it is important to understand how they influence the static neuronal dynamics. The neuron needs to be able to "integrate" signals from many other neurons. In order to do so, the neuron needs to be able to turn the spatially separated windings of the incoming topological charges into time dependant stimuli of the order parameter in the neuron. This is achieved with a metal spacer between the neuron and it's dendrites. This forms a spin-valve like structure. when a series of topological charges build up on the interface of the metal, a cumulative spin injection torque is injected into the metal layer and from the metal layer into the neuron.

In source [40] the neuronal structure is achieved through a one domain antiferromagnet. It being a single domain, it assumed that there is no texture in the order parameter, i.e. $\partial_x \phi = 0$. The equations of motion are the same as in equation 4.7, but of course the ∂_x term vanishes and the incident torque on the neuron is added

$$\begin{aligned} \partial_t \phi &= \frac{M}{\tilde{\chi}} \\ \partial_t M &= -\frac{\tilde{\kappa}}{2} \sin 2\phi - \tilde{\alpha} \tilde{J} \partial_t \phi + \tau(t). \end{aligned} \tag{4.15}$$

The tilde parameters are defined exactly as before, but for the one domain system (they can be tuned differently). It is easy to see then that the energy is minimized when the magnetization is 0 and ϕ is a multiple of π. Taking the time derivative on both sides in equation 4.15 it is possible to eliminate M from the equation

$$\partial_t^2 \phi = \frac{\partial_t M}{\tilde{\chi}}. \tag{4.16}$$

Inserting this into the second term in equation 4.15 it becomes

$$\tilde{\chi} \partial_t^2 \phi = \frac{\tilde{\kappa}}{2} \sin 2\phi - \tilde{\alpha} \partial_t \phi + \tau(t). \tag{4.17}$$

This is a result much more useful for numerical calculations which is used later. The unknown part of equation 4.17 at the moment is the incident torque, τ. In order to solve 4.17 the

incident torque has to be found. So in order to proceed the theoretical basis of torque transfer in the metal interface has to be considered.

4.5 Torque transfer in interfaces

The dendrites terminate in a metal spacer, which again is connected to the neuron. Multiple dendrites need to terminate in the same metal spacer, in order for the postsynaptic neuron to receive multiple signals. Therefore, there is a need for some way of connecting multiple one-dimensional wires onto the neuron. This metal spacer separating the neuron and incoming signals is believed to do this.

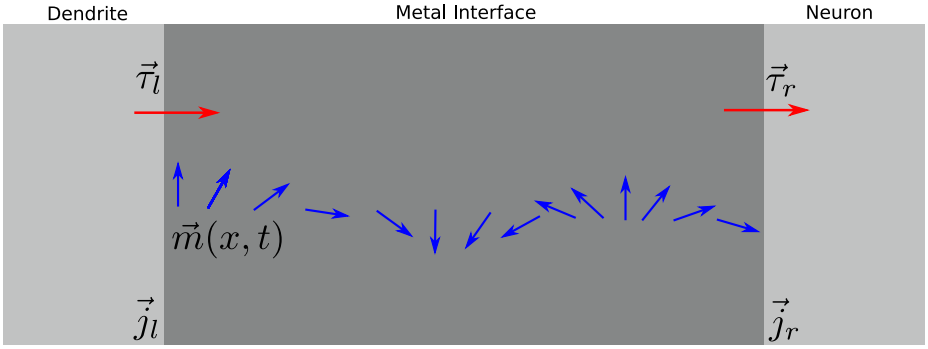

Figure 4.2: The figure shows the dendrite-metal and metal-neuron interface. $\vec{\tau}_l$ denotes the torque into the metal from the dendrite, $\vec{\tau}_r$ denotes the torque into the neuron and $\vec{j}_{l/r}$ denotes the spin current in the left and right interface. The blue vectors show the spin wave through the metal interface with order parameter $\vec{m}(x,t)$.

The unknown parameter in equation 4.17 is, as established, the incident torque τ. The torque on the interfaces between the dendrite and metal is [43]

$$j_{l,r}^{(s)} = \pm\frac{g}{4\pi}(\mu_{l,r} - \hbar\partial_t\phi). \tag{4.18}$$

Here μ is the out of easy plane spin accumulation at the interface, and g the real part of the spin mixing conductance [44]. The spin current induced at the interfaces are made of two contributions, the spin accumulation and a spin pumping term ($\sim \partial_t\phi$). Due to continuity the following border condition must hold,

$$A\partial_x\phi(x_i) = j_{r,l}^{(s)}. \tag{4.19}$$

That is, the derivative of ϕ at the border x_i has to be conserved across the boundary [45]. As explained later, the spin dynamics of the neuron is relatively slow compared to the topological charges in the dendrite that propagate along the intermediate structure. This means that

the spin pumping term of equation 4.18 can be neglected at the second interface, as the neuronal order parameter evolves at a very slow rate ($\partial_t \phi \sim 0$). It is now possible to write the current densities at both interfaces as the following,

$$\begin{aligned} j_l &= \frac{\hbar g}{4\pi}(\frac{\mu_s}{\hbar} - \partial_t \phi) \\ j_r &= \frac{\hbar g}{4\pi}\frac{\mu_s}{\hbar}. \end{aligned} \tag{4.20}$$

Here the subscript l and r denotes the left and right interfaces in figure 4.2. In source [40] they simplify equation 4.20 by stating that both interfaces have the same spin-mixing conductance. In order to generalize, it is possible to work with different spin-mixing conductances(g) to encapsulate both different interfacial impedances and possible losses of energy in the metal spacer. However, it is not done in further considerations. Applying the continuity equation over the two interfaces sequentially and assuming equal transmission/reflection rates

$$-j_l = j_r. \tag{4.21}$$

Then it is easy to see from the current equations 4.20 that the spin accumulation has to be $\mu_s = \hbar \partial_t \phi/2$ and the current becomes

$$j_l = \frac{\hbar g}{8\pi}\partial_t \phi. \tag{4.22}$$

The total momentum transfer into the neuron is thus

$$\delta M = \int dt j = \hbar g/8\pi. \tag{4.23}$$

Going back to the soliton motion, in equation 4.14. It is possible to define a speed for which topological charges can enter the metal spacer un-deformed by solving the boundary condition in equation 4.19. By some algebra the speed becomes

$$v = \frac{8\pi A}{\hbar g}. \tag{4.24}$$

That is if solitons are moving at that speed the boundary condition holds and the topological charge is transferred without loss to the metal spacer. In reality, setting solitons to a specific speed might prove to be very tedious, but it is at least possible to set them at speeds close to the limit to reduce energy loss in the system.

4.6 Neuronal dynamics and timescales

As the torque/current is now known it is possible to obtain the equations of motion for the neuron by eliminating $\vec{M}$ in equation 4.15. This is done in a similar fashion as before

$$\tilde{\chi}\partial_t^2 \phi + \frac{\tilde{\kappa}}{2}\sin 2\phi + \tilde{\alpha}\tilde{J}\partial_t \phi = \tau(t). \tag{4.25}$$

This equation describes a particle in motion in a washboard potential ($\sim \sin^2\phi$). The local minimas are as before $\phi = N\pi$. Equation 4.25 can be approximated near $\phi = N\pi$ to get some understanding about some characteristics of the neuronal system. Dropping the τ from equation 4.25 it is possible to write equation 4.25 as the following

$$\begin{gathered}\partial_t^2\phi + \frac{\tilde{\alpha}\tilde{J}}{2\sqrt{\tilde{\chi}\tilde{K}}}\sqrt{\frac{\tilde{K}}{\tilde{\chi}}}\partial_t\phi + \frac{\tilde{K}}{\tilde{\chi}}\phi = 0 \\ \partial_t^2\phi + 2\eta\omega_0\partial_t\phi + \omega_0^2\phi = 0\end{gathered} \tag{4.26}$$

Where the constants were rearranged to a known system, the damped harmonic oscillator. By having equation 4.26 on this form some conclusion can be drawn. Here η is known as the damping ratio of a harmonic oscillator and ω_0 the un-damped angular frequency of a harmonic oscillator. In this case, the damping ratio η is set to the over damping limit ($\eta > 1$). The relaxation time of such an oscillator can be quite easily be found by considering when the amplitude reaches $1/e$ of its original size, and becomes

$$t_0 = \frac{1}{(\eta - \sqrt{\eta^2 - 1})}\omega_0. \tag{4.27}$$

Which can be said to be the integration timescale for the neuron, if signals are further apart they do not sum at the neuron. The signals have to come in such a frequency that the decay does not have time to occur in order for a phase flip to happen. The incident neuron has a domain wall width of around $\lambda \sim 10nm$ [40], a domain wall velocity of $v \sim 0.01u - 0.1u$ with $u \sim 10km/s$ [40] which means the pumping of spin current into the metal spacer happens on a timescale of $t_s \sim \lambda/u \sim 0.01 - 0.1ns$. The time of propagation through the normal-metal spacer can be estimated with the Thouless time $t_d \sim l^2/D \sim 0.1ps$ [46].

The time relaxation of the neuron is for comparison in the order of $t_0 \sim 1ns$ which means that the incident spin currents on the neuron can be viewed as delta pulses in the time frame of the neuron. Now each pulse elevates the magnetization $\vec{M}$ by some constant $\delta\vec{M}$. From equation 4.15 this lifts $\partial_t\phi$ by some $\nu_0 = \delta M/\tilde{\chi}$. The incident pulse then kicks the initial state up to some δM so that it starts it's over damped decay towards 0. A series of topological charges coming in with some frequency ω slightly perturbs the state ϕ, until the phase is able to flip to $\phi = \pi$. Therefore, whether the neuron fires is dependent on the rate of incoming charges ω and ν_0. It is then clear that the neuron holds the desired leaky integrate and fire functionality mentioned previously. Only if the pulses are close enough in time, with high enough amplitude and with sufficient frequency, entails that a topological charge is passed into the axon with topological charge $\zeta = \pm 1$.

It is also possible to imitate biological bursting, the neuron firing in a repetitive matter by introudcing a constant torque into the neuron. This tilts the potential from being $\sim \sin^2\phi$

to being $\sim \sin^2\phi - \phi$. This causes the minimas to no longer be stable such that it oscillates between $\phi = 0$ and $\phi = \pi$ so that there are multiple domain walls propagating into the axon. This can be achieved by stimulating the neuron in a manner such that it oscillates through both ground states repeatedly.

4.7 One dimensional nanostrip synapse

As mentioned previously, the synaptic structure needs to hold a method for adjusting strength of signals, and it needs to be capable of storing that strength. This is achieved through an antiferromagnet nanostrip holding winding textures of topological charges. The governing Hamiltonian of such a system is equation 4.2. The density of topological charges is

$$w = N\lambda/L. \tag{4.28}$$

Where N is the total number of topological charges, λ is the length of the domain walls in equation 4.14 and L is the length of the system. L is much larger than λ, therefore it is possible to consider w as a continuous variable as each step in N becomes sufficiently small. The nanostrip behaves as an effective 1d thermodynamic system with a chemical potential $\mu(w) = \delta F/\delta N$, that is a thermodynamic "cost" of adding another topological charge into the strip.

In order to update the weight w, first denote the local order parameter ϕ at the end of the nanostrip as ϕ_2. As for the neuron the order parameter is subject to a washboard potential. In this case it is tilted with $-\mu/\pi$ as there is a chemical potential present. As a topological charge arrives at the synapse from the presynaptic neuron it perturbs the local order parameter ϕ_2, either from direct perturbation or from heat. After the perturbation the synapse is briefly activated and a current of topological charges flow out to the postsynaptic neuron as they are perturbed from the local minima caused by the tilted washboard potential. This causes a stronger signal to reach the postsynaptic neuron. The amount of topological charges released to the post synaptic neuron are directly dependant of the tilting of the "experienced" potential, and hence the chemical potential μ in the nanostrip.

The chemical potential is as mentioned previously a function of the density of topological charges w. Therefore the higher density of topological charges present in the nanostrip synapse the more topological charges are released when the order parameter in the end of the nanostrip is activated. This can be viewed as the valve of a gas cannister being open causing a burst of gas or here topological charges being released.

Since topological charges are released into the dendrite the synaptic weight w is reduced.

Therefore some process to adjust and restore the synaptic weight has to be present. This is done with connecting a reservoir of topological charges with a chemical potential μ_0 to the left end of the synaptic nanostrip where $\mu_0 > \mu$. Consider now the local order parameter ϕ_1 at the left end of the nanostrip. This ϕ_1 is similar to ϕ_2 under a tilted washboard potential with a slope proportional to the difference in chemical potential $\mu - \mu_0$. The goal is now is to be able to increase the synaptic weight w with a combination of two things, the presynaptic signal and the casual postsynaptic feedback.

One possibility to activate the synapse is described in source [41]. The goal would then be to activate the dynamics of ϕ_1 allowing topological charges to flow from the reservoir into the synapse. The dynamics can be activated as a combination of the postsynaptic feedback loop or through remnant heat from the presynaptic neuron. When new topological charges enter the synaptic nanostrip the density of topological charges increases. This caused the nanostrip to find a new equilibrium with a new chemical potential μ_1. Tuning the strength of the training function of the system can therefore be done through adjusting the chemical potential μ_0. The free energy of a thermodynamic system can be expressed as

$$\mu = \frac{\delta F}{\delta N}. \tag{4.29}$$

In this system the free energy is defined as in equation 2.74. However the DMI and external magnetic field is not included in the calculations here and the free energy reduces to the following under the assumption that the magnetisation is small so that the $\vec{m}^2$ can be ignored in equation 2.74

$$F = \int d^3r - \frac{K}{2}(\vec{n} \cdot \hat{r})^2 + \frac{A}{2}(\frac{\partial}{\partial x}\vec{n})^2. \tag{4.30}$$

Using the same parameterization as before, when ϕ was used to describe the in plane angle of the order parameter this reduces to

$$F = \int_0^L dx \frac{A}{2}(\partial_x \phi)^2 + \frac{\kappa}{2}\sin^2(\phi). \tag{4.31}$$

Previously when this free energy was minimized in order to obtain equation 4.14 it was assumed that the topological charge had a winding number of $\zeta = \pm 1$. Naturally, in a system supposed to hold a multiple of topological charges, this assumption does not hold. If one allows for higher charge numbers, the structure changes as well.

It is however possible to minimize the structure exactly. As in the supplementary material of [40] when ignoring geometric and entropic effects the solution becomes

$$\phi(x) = \pm \begin{cases} N\pi/2 + \text{am}\left(\frac{x}{k\lambda}, k^2\right), & \text{odd } N \\ (N-1)\pi/2 + \text{am}\left(\frac{x}{k\lambda} + K\left(k^2\right), k^2\right), & \text{even } N. \end{cases} \tag{4.32}$$

Where am is the Jacobi amplitude function and K is the elliptic integral of the first kind. The parameter $0 \leq k \leq 1$ can be found from solving

$$2kK(k^2) = \frac{1}{w}. \tag{4.33}$$

The solution of equation 4.32 are that of the static sine Gordon equations, i.e. $\partial_t \phi = 0$ in equation 4.14. If one were to set $k = 1$ and introduce the Lorentz boost, $x \to x - vt/\sqrt{1 - v^2/u^2}$ you arrive back at the kink/antikink soliton solution of equation 4.14 [47]. The elliptic functions might be an unknown subject to the reader. In general it is possible to think of them as generalizations of inverse trigonometric functions, allowing for variations outside the normal $0 \to \pi$, $-\pi/2 \to \pi/2$ ranges of arccos and arctan.

The derivative of the Jacobi amplitude function is again defined as another special elliptic function $\frac{d}{du}\,\mathrm{am(u,k)} = \mathrm{dn}(u, k)$. The total free energy is then

$$F = \int_0^L \left(\frac{A\,\mathrm{dn}\left(\frac{x}{k\lambda}, k^2\right)^2}{2k^2\lambda^2} + \frac{\kappa \sin\left(\frac{N\pi}{2} + \mathrm{am}\left(\frac{x}{k\lambda}, k^2\right)\right)^2}{2} \right) \mathrm{d}x \tag{4.34}$$

In order to find how the chemical potential varies with synaptic weight w the free energy is found numerically, before a numerical differentiation is performed to find the chemical potential.

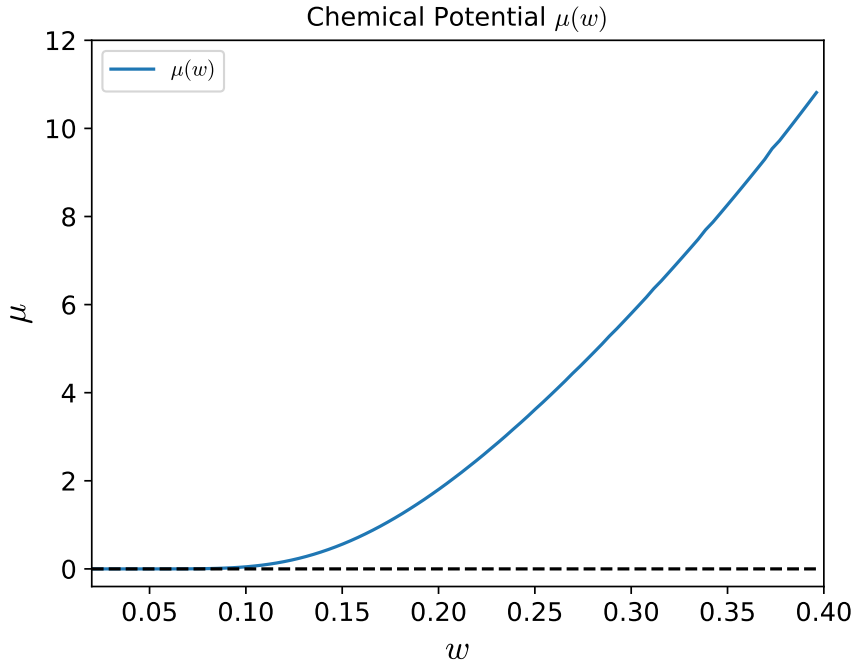

Figure 4.3: The figure shows the chemical potential as a function of the synaptic weight w. It appears to approach a linear function as w increases.

As seen in figure 4.3 the chemical potential increases exponentially for low w (above $w = 0.1$). For higher w however, the chemical potential seems to approach a linear asymptote. The result differs from source [40] as it was found there that the chemical potential starts at one, increases exponentially first and the approaches an asymptote $\pi^2 w\sqrt{A\kappa}$. Here, both the starting value and the asymptotic value seem to differ. The trend of the chemical potential is similar to that of source [40], it is only the asymptotic value and the starting value that are different. However, it might seem logical that the chemical potential should start at zero, since there is no energetic "cost" of adding a topological charge when there is nothing present in the synaptic strip.

4.8 Training the antiferromagnetic spiking neural network

For the proposed network, a STDP method can be used to train the network. The main idea is as mentioned previously that casual firing increase the synaptic weight w. The proposed network is then to be trained based on the arrival and exit time of the neurons. As mentioned previously, the only way for the synaptic increase or recovery in the synapse is that ϕ_1 is activated so that topological charges are activated in μ_0 and can flow into the synaptic strip. For ϕ_1 to still be activated, there needs to be enough reactivity left in the order parameter due to the firing of the neuron. There is therefore some time dependence on when the neuron fires and if the synaptic weight increases or decreases.

Denote first the different in time of firing from the presynaptic neuron as t_{pre} and the postsynaptic neuron firing time as t_{post}. The difference in time $\delta t = t_{post} - t_{pre}$ is then the variable that should cause a difference in the change of synaptic weight during a neuron event. Now, there are several functions that can be used to implement the synaptic change. There are however some characteristics which need to be taken into account. Firstly, if there is a negative δt, the change of synaptic weight has to be negative. If the postsynaptic neuron already fired, the synaptic weight should just decrease if the presynaptic neuron fires, since this causes release of topological charge from the synapse without causing firing. That is, if there is no causality in the postsynaptic neuron firing with the presynaptic neuron, then the synaptic wight decreases. This also makes sense in terms of Hebbian learning that was discussed earlier. Now if δt is positive and hence the firing of the presynaptic neuron and postsynaptic neuron seem to be causal, then the weight is expected to increase. However, only for a window of δt as for very large δt the causality argument does not hold.

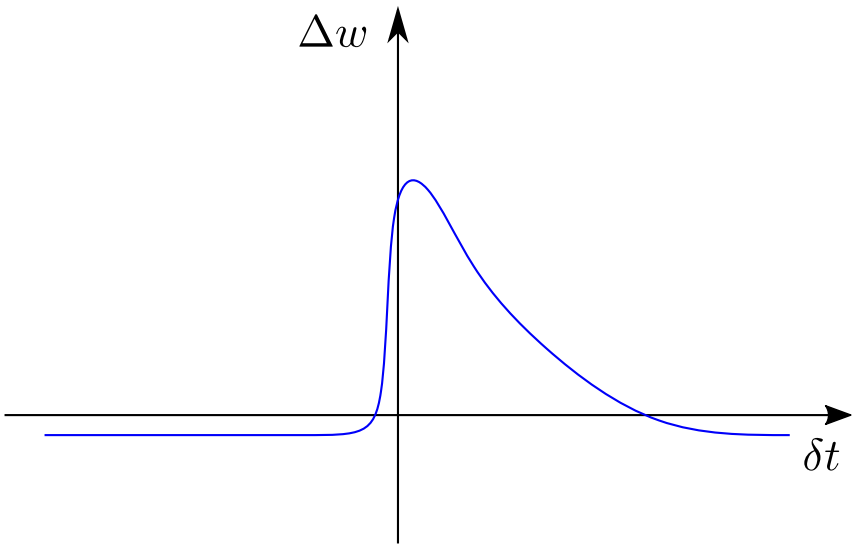

Figure 4.4: The figure shows a possible way to change the synaptic weight Δw as a function of the time difference of firing of presynaptic and postsynaptic neurons.

Figure 4.4 is just one possibility of many in terms of implementing the synaptic weight change to train the network. To be clear, this is not an analytical function that has been calculated here, it is just a sketch. Figure 4.4 does however incorporate the most important concepts described in the above paragraph. The only constraint is that the synaptic weight as mentioned previously needs to be activated through remnant heat or the feedback loop in figure 4.1, therefore if the time difference is too large there should be negative change in the synaptic weight as the topological charge cause bursting of charges into the metal spacer at the synapse as a topological charge arrives at the neuron.

4.9 Single spike energy loss

The energy effectivness is one of the most compelling elements of the proposed setup. The main benefit is that the system merely reshuffles states, without dissipating too much of the energy. This can be seen from equation 4.2 as the free energy is not altered by shifting the location of the domain wall. However this is not the full picture as the Gilbert damping term do dissipate energy as some frictional force as seen in the Rayleigh dissipation function (equation 4.5). The energy loss can then be found by integrating the Rayleigh dissipation function over a typical domain wall width λ to obtain a typical dissipation rate of $\sim \alpha J v^2/2\lambda$. Taking $\alpha \sim 10^{-4}$, $J \sim 10^3 \hbar/nm$ and $\lambda \sim 10nm$ yields a dissipation rate of around $1pJ/s$. If the system is to operate in the GHz regime the energy loss of each spike transmission is

$\sim 10^{-21} J$ which is so small it almost negligible. The network would need to operate at GHz frequencies the loss would be of order $\sim 10^{-12} J/s$, where it is considered that one transmits one billion spikes per second in a single neuron.

Of course, the dissipation rate calculated here is very simplified, and the real rate is probably a lot higher. However, it seems the rate per spike is indeed very low for the physical system that is considered here. In order to estimate it even more thoroughly, one would need to include the losses of other parts of the system than the propagation dendrites, and include control voltages in for example the chirality battery of the synapse. As mentioned earlier, it might also be need for some driving force which would decrease energy efficiency.

4.10 Numerical results

The previous discussion can be used to recalculate the phase diagram and neuron firing found in source [40]. The parameters are chosen in a similar manner and in accordance with source [40]. However the results may differ slightly as source [40] uses only approximate values for the parameters and not complete ones. The goal would then be to find for which w and ν_0 the neuron fires and to present some visualisation of how the time development of the order parameter angle ϕ develops in a firing and non-firing regime.

Variable name	Value
Anisotropic constant $\tilde{\kappa}$	1×10^{-22} J
Spin suscebility $\tilde{\chi}$	1×10^{-42} Js^2
Saturated spin density $\tilde{J}$	$1 \times 10^{5}\,\hbar$
Gilbert damping constant $\tilde{\alpha}$	1×10^{-2}

Table 1: This table shows the values chosen for the parameters in this section's numerical results.

In order to find the phase diagram 20 pulses were fired for 200 differing w and ν_0. The end order parameter in the neuron was then recorded as either fired, or non fired depending on the final phase angle.

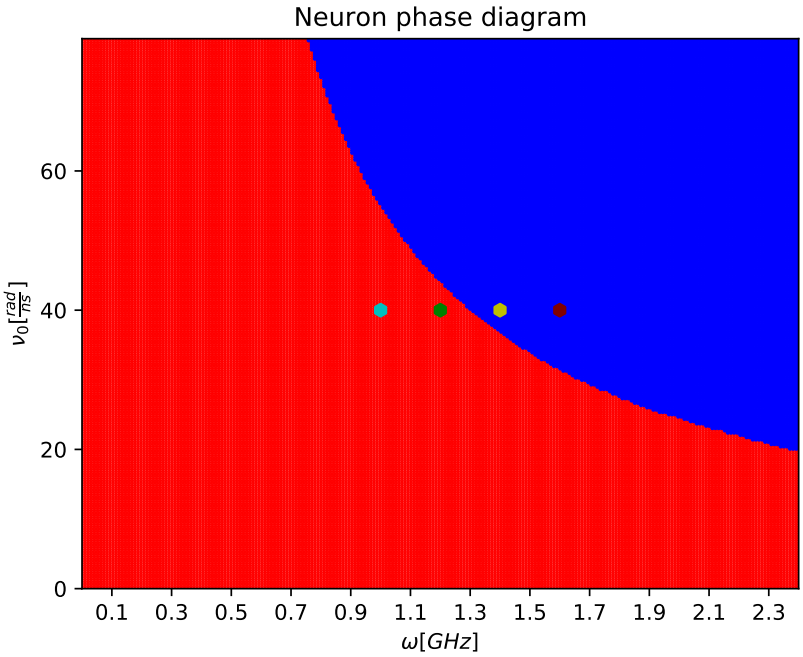

Figure 4.5: The figure shows the phase diagram of the neuron firing in terms of ν_0 and ω. The non firing states are denoted in red and firing values in blue, in addition the four neuron values shown in figure 4.6 are added in the phase plot as well.

As seen from figure 4.5 the phase angle of the neuron (ϕ) seems to vary in the expected manner. The firing is a function of the incoming frequency w and the instant momentum change $\delta\nu_0$. This result was achieved by integrating equation 4.17 by a RK4 method. The goal is to see at which frequencies and amplitudes the neuron fires in order to get an idea of whether it shows the desired phase transition from firing to non-firing. In addition to the phase, there are 4 different neuron outputs plotted as a response to 20 pulses from the dendrite. As mentioned before, these are simply modelled as delta pulses and are cut off once the neuron reaches its firing regime.

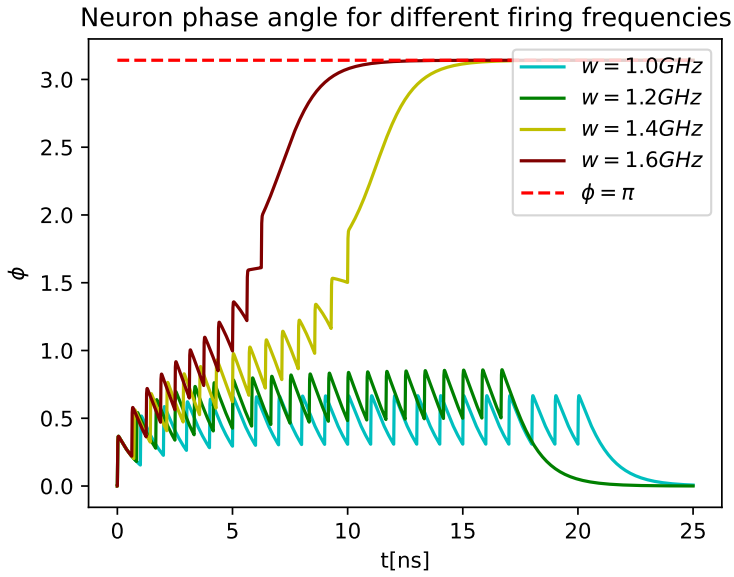

Figure 4.6: The figure shows the time evolution of the neuron phase angle (equation 4.8) for different frequencies of incoming topological charges. 20 pulses are fired until the neuron fires. The frequencies used are marked in the phase diagram in figure 4.5.

The aforementioned points are also plotted in figure 4.6 to see that they behave in the expected manner. It is evident from figure 4.6 that the desired behaviour is present. The response of the order parameter seems to be in accordance with the expected result from the phase diagram in figure 4.5. The neuronal phase transition seems to be in accordance with source [40], which shows a similar phase transition between the non-firing and firing regime.

5 Effect of finite temperature on domain wall velocity in antiferromagnets

In order to repeat the calculation with a more complex Hamiltonian it is useful to remind oneself of the original free energy in equation 4.2. The free energy is a function of the exchange energy, anisotropic energy, magnetic field, temperature and DMI. It is not however so easy to find an analytic solution to such an equation without any approximation. Starting at equation 2.74 and including a Rayleigh dissipation function density of the form $R = \frac{\alpha J}{2}\dot{\vec{n}}$ and writing the equation of motion in terms of the free energy field $\vec{f}(\vec{n})$, the equations of motion in terms of the Néel vector $\vec{n}$ becomes

$$\vec{n} \times \left(\ddot{\vec{n}} - \vec{f} + \frac{\alpha J}{2} \dot{\vec{n}} \right) = 0. \tag{5.1}$$

Note here that the purely Néel vector description of section 2 is used. $\vec{f}$ can be seen from equation 2.77. The inclusion of a finite temperature can be done through adding a stochastic field $\vec{f}^{th}$ to the effective field in equation 5.1, $\vec{f} \to \vec{f} + \vec{f}^{th}$ [48]

$$\vec{n} \times \left(\ddot{\vec{n}} - (\vec{f} + \vec{f}^{th}) + \frac{\alpha J}{2} \dot{\vec{n}} \right) = 0. \tag{5.2}$$

The dissipation fluctuation theorem relates the thermal field to the damping parameter α in the system. The thermal field is further defined through the following two correlators [22]

$$\begin{gathered} \langle \vec{f}^{th}_{\alpha} \vec{f}^{th}_{\beta} \rangle = 2\xi \delta_{\alpha\beta} \delta(\vec{r} - \vec{r}') \delta(t - t') \\ \langle \vec{f}^{th} \rangle = 0. \end{gathered} \tag{5.3}$$

That is the noise from the thermal field is uncorrelated in time and space. So essentially, the noise at each point in time and space is a random number with some amplitude ξ. ξ is here defined as $\xi = \alpha k_B T(\vec{r})$ and is a function of the temperature over the structure in question. Also note again that this is a function of α, the dampening constant. Doing these means that the previous LLG equation turns into a stochastic equation, the stochastic Landau Lifzitzh Gilbert equation, or sLLG equation. Stochastic equations are harder to solve than a regular partial differential equation due to the intrinsic randomness and therefore need some approximation in order for it to be solvable analytically. Numerically, the solution of such an equation can be done directly by inserting the correlation and drawing random variables in each time step of the numerical solver in question and directly incorporating them in the effective field.

5.1 Linearising the Néel vector

The first simplification is to look at deviations from a slowly varying magnetic structure $\vec{n}^0$, $\delta\vec{n}$. Referencing the earlier sine Gordon structure in equation 4.14 the domain wall would be

the slowly varying magnetic texture $\vec{n}^0$ and $\delta\vec{n}$ small and fast deviation from that magnetic structure due to temperature. The Néel order parameter can then be expressed as a deviation from a 0 structure as the following

$$\vec{n} = \sqrt{1-\delta\vec{n}^2}\vec{n}^0 + \delta\vec{n}. \tag{5.4}$$

To see that this definition holds simply square it to see that the Néel order parameter is defined as $\vec{n}^2 = (1-\delta\vec{n}^2)(\vec{n}^0)^2 + \delta\vec{n}^2$. One can also note that the Néel vector length is to be conserved under the transformation of variables and therefore the 0 state has to be scaled by the length to keep the length constant. The fluctuations δn are taken as perpendicular to n^0,

$$\delta\vec{n}\cdot\vec{n}^0 = 0. \tag{5.5}$$

Now substituting the new definiton into equation 5.1

$$\begin{aligned}(\sqrt{1-\delta\vec{n}^2}\vec{n}^0 + \delta\vec{n}) \times \Bigg(\frac{\partial^2}{\partial t^2}(\sqrt{1-\delta\vec{n}^2}\vec{n}^0 + \delta\vec{n}) \\ -(\vec{f}+\vec{f}^{th}) + \frac{\alpha J}{2}\frac{\partial}{\partial t}(\sqrt{1-\delta\vec{n}^2}\vec{n}^0 + \delta\vec{n})\Bigg) = 0.\end{aligned} \tag{5.6}$$

By expanding equation 5.6 and collecting terms of 0th order in $\delta\vec{n}$, and writing the rest of the terms as a perturbative torque $\vec{\tau}$ equation 5.6 becomes

$$\vec{n}^0 \times (\ddot{\vec{n}}^0 - \vec{f}^{th} + \frac{\alpha J}{2}\dot{\vec{n}}^0) + \vec{\tau} = 0. \tag{5.7}$$

$\vec{f}$ and hence also $\vec{\tau}$ is now in terms of the new order parameter $\vec{n} = \vec{n}_0 + \delta\vec{n}$ and is defined as $\vec{f} = \frac{\delta F}{\delta n}$. Before going any further $\vec{f}$ is found in terms of the new variables. The original F in terms of the old Néel vector can be seen in equation 2.74 and is written out here to reiterate the result

$$F[\vec{n}] = -\frac{\tilde{K}}{2}(\vec{n}\cdot\hat{r})^2 + \frac{A}{2}|\nabla\vec{n}|^2 - d\chi\cdot(\hat{r}\times\vec{n}) + D\vec{n}\cdot(\nabla\times\vec{n}). \tag{5.8}$$

Here a $\hat{r}$ vector has been pulled out of the homogeneous DMI. That entails that the constant d_χ have absorbed the strength of the interaction. The term for the external magnetization and homogeneous DMI was dropped here as it is not considered in the earlier calculations, inhomogeneous DMI has been added however to see the effects on the eventual thermodynamic torque contribution. Performing the functional derivative to find f the following becomes the result

$$\vec{f} = -\frac{\kappa}{2}(\vec{n}\cdot\hat{r})\hat{r} + A\nabla^2\vec{n} + 2D\nabla\times\vec{n} \tag{5.9}$$

Inserting $\vec{n} \to \sqrt{1-\delta\vec{n}^2}\vec{n}^0 + \delta\vec{n}$ into f this becomes

$$\begin{aligned}\frac{\vec{f}_{\vec{n}^0}}{\sqrt{1-\delta\vec{n}^2}} &= A\nabla^2\vec{n}^0 - \frac{\kappa}{2}(\vec{n}^0\cdot\hat{r})\hat{r} + 2D\nabla\times\vec{n}^0 \\ \vec{f}_{\delta\vec{n}} &= A\nabla^2\delta\vec{n} - \frac{\kappa}{2}(\delta\vec{n}\cdot\hat{r})\hat{r} + 2D\nabla\times\delta\vec{n}\end{aligned} \tag{5.10}$$

Finally the torque term $\vec{\tau}$ from equation 5.7 becomes the following

$$\vec{\tau} = -\vec{n}^0 \times (\vec{f}_{\vec{n}^0} + \vec{f}_{\delta\vec{n}}) - \delta\vec{n} \times (\vec{f}_{\vec{n}^0} + \vec{f}_{\delta\vec{n}}). \tag{5.11}$$

The full $\vec{\tau}$ expression is tedious to do work on simultaneously. Therefore each interaction is accounted for individually.

5.1.1 Exchange torque

Looking first at the terms containing the exchange interactions (the terms of $\vec{f}$ containing $A\nabla^2$) the following four terms are present

$$\begin{aligned}\vec{\tau}_{ex} = -A(&\Gamma\vec{n}^0 \times \nabla^2\Gamma\vec{n}^0 + \delta\vec{n} \times \nabla^2\delta\vec{n} \\ &+\Gamma\vec{n}^0 \times \nabla^2\delta\vec{n} + \delta\vec{n} \times \nabla^2\Gamma\vec{n}^0).\end{aligned} \tag{5.12}$$

Where Γ is used as shorthand and $\Gamma = \sqrt{1-\delta\vec{n}^2}$. By using the Einstein summing convention and the Levi-Cevita tensor this becomes

$$\begin{aligned}\vec{\tau}_{ex} = -A(&\epsilon_{ijk}\sqrt{1-\delta\vec{n}^2}n_j^0\partial_k^2\sqrt{1-\delta\vec{n}^2}n_k^0 + \epsilon_{ijk}\delta n_j\partial_k^2\delta n_k \\ &+\epsilon_{ijk}\sqrt{1-\delta\vec{n}^2}n_j^0\partial_k^2\delta n_k + \epsilon_{ijk}\delta n_j\partial_k^2\sqrt{1-\delta\vec{n}^2}n_k^0)\end{aligned} \tag{5.13}$$

Defining the mean perturbation over some integrating time t, as $\langle\delta\vec{n}\rangle$ it is possible to find a course grained approximation to the torques

$$\begin{aligned}\vec{\tau}_{ex} = -A((1-\langle\delta\vec{n}^2\rangle)\epsilon_{ijk}n_j^0\partial_k^2 n_k^0 + \langle\epsilon_{ijk}\delta n_j\partial_k^2\delta n_k\rangle) \\ +\epsilon_{ijk}\sqrt{1-\langle\delta n\rangle^2}n_j^0\partial_k^2\langle\delta n_k\rangle + \epsilon_{ijk}\langle\delta n_j\rangle\partial_k^2\sqrt{1-\langle\delta n\rangle^2}n_k^0)\end{aligned} \tag{5.14}$$

However $\delta\vec{n}$ describes thermal fluctuations around a magnetic texture. Averaging over the random perturbation gives zero as the noise included in $\vec{f}^{th}$ is uncorrelated and centred at zero. Therefore the first order mean temperature noise $\langle\delta\vec{n}\rangle \to 0$. In addition it is possible to introduce the expansion

$$\sqrt{1-\langle\delta\vec{n}^2\rangle} = 1 + \langle\delta\vec{n}\rangle - \frac{1}{2}\langle\delta\vec{n}^2\rangle + O(\delta\vec{n}^3) \approx 1 - \frac{1}{2}\langle\delta\vec{n}^2\rangle. \tag{5.15}$$

Equation 5.14 then becomes

$$\vec{\tau}_{ex} = -\frac{A}{2}((\langle\delta\vec{n}^2\rangle)\epsilon_{ijk}n_j^0\partial_k^2 n_k^0 - \langle\epsilon_{ijk}\delta n_j\partial_k^2\delta n_k\rangle) \tag{5.16}$$

The squared mean values are of course not zero as you take random variables centred at 0 and square them, creating a net positive torque. Rewriting this in terms of vector identities can reduce this expression to

$$\vec{\tau}_{ex} = -A(\langle\delta\vec{n} \times \partial_k^2\delta\vec{n}\rangle + \partial_k\langle\delta\vec{n}^2\rangle\vec{n}^0 \times \partial_k\vec{n}^0). \tag{5.17}$$

5.1.2 DMI torque

Moving to the torque exerted by the bulk DMI, $\vec{\tau}_{DMI} \sim 2D\nabla \times \vec{n}$. Once again applying the small $\delta\vec{n}$ approximation in equation 5.15 in the square root of $\vec{n}^0$ and disregarding terms of $O(\delta\vec{n}^3)$ and higher gives

$$\begin{aligned}\vec{\tau}_{DMI} = -2D((1-\frac{1}{2}\langle\delta\vec{n}^2\rangle)\vec{n}^0 \times \nabla \times (1-\frac{1}{2}\langle\delta\vec{n}^2\rangle)\vec{n}^0 \\ +(1-\frac{1}{2}\langle\delta\vec{n}^2\rangle)\vec{n}^0 \times \nabla \times \langle\delta\vec{n}\rangle \\ +\langle\delta\vec{n}\rangle \times \nabla \times \Gamma\vec{n}^0 + \langle\delta\vec{n}\rangle \times \nabla \times \langle\delta\vec{n}\rangle).\end{aligned} \tag{5.18}$$

As before averaging over a random thermal perturbation gives zero and the remaining perturbative term is

$$\vec{\tau}_{DMI} = -2D(\langle\delta\vec{n}^2\rangle)\vec{n}^0 \times (\nabla \times \vec{n}^0). \tag{5.19}$$

Thus the final DMI torque term has been found. It is also is a function of the squared mean deviation in the $\delta\vec{n}$ parameter $\langle\delta\vec{n}\rangle^2$.

5.1.3 Anisotropic torque

The next torque contribution is the anisotropic contributions, denoted $\vec{\tau}_{ani}$. The anisotropic terms are here the terms proportional to κ in equation 5.9. Extracting the anisotropic terms from equation 5.11 gives the following contributions to the torque when averaging over δn and applying equation 5.15

$$\vec{\tau}_{ani} = \frac{K}{2}((1-\frac{1}{2}\langle\delta\vec{n}^2\rangle)\vec{n}^0 \cdot \hat{r})(1-\frac{1}{2}\langle\delta\vec{n}^2\rangle)\vec{n}^0 \times \hat{r} \tag{5.20}$$

Again averaging over the random component $\delta\vec{n}$ should yield zero as the noise is uncorrelated. Again, collecting torque terms from the thermal fluctuations of at most order $\delta\vec{n}^2$ yields the following final torque

$$\vec{\tau}_{ani} = -\frac{K}{2}(\langle\delta\vec{n}^2\rangle)(\vec{n}^0 \cdot \hat{r})\vec{n}^0 \times \hat{r} \tag{5.21}$$

5.1.4 Total torque

The final torque $\vec{\tau}$ is then

$$\begin{aligned}\vec{\tau} = \vec{\tau}_{ex} + \vec{\tau}_{DMI} + \vec{\tau}_{ani} \\ = -A(\langle\vec{\delta}n \times \partial_k^2\delta\vec{n}\rangle + \partial_k\langle\partial\vec{n}^2\rangle\vec{n}^0 \times \nabla\vec{n}^0) + D(\langle\delta\vec{n}^2\rangle)\vec{n}^0 \times (\nabla \times \vec{n}^0) \\ -\frac{K}{2}(\langle\delta\vec{n}^2\rangle)(\vec{n}^0 \cdot \hat{r})\vec{n}^0 \times \hat{r}.\end{aligned} \tag{5.22}$$

The exchange torque is by convention in for example source [49] denoted as a reactive torque (proportional to $\langle\vec{n} \times \nabla^2\delta\vec{n}\rangle$) and a dissipative torque (proportional to $\nabla\vec{n}^0$). Rewriting

equation 5.22 and introducing $J_i^n = \frac{A}{\hbar}\vec{n}^0 \cdot \langle \delta\vec{n} \times \nabla^2 \delta\vec{n} \rangle$ and $\rho = \langle \delta\vec{n}^2 \rangle$ as the magnon current and the number density equation 5.22 becomes

$$\begin{aligned} \vec{\tau} = -\hbar J^n \nabla \vec{n}^0 + A(\nabla\rho)\vec{n}^0 \times \nabla\vec{n}^0 - 2D(\rho)\vec{n}^0 \times (\nabla \times \vec{n}^0) \\ + \frac{K}{2}(\rho)(\vec{n}^0 \cdot \hat{r})\vec{n}^0 \times \hat{r}. \end{aligned} \tag{5.23}$$

In order to translate the first term of equation 5.17 to the first term of equation 5.23, note that the term is defined as the divergence of spin current $\vec{\tau} = \partial_i J_n^i$. The spin current can be be split to transverse and longitudunal components relative to n^0 and by writing it out according to the method in source [49].

5.2 The method of collective coordinates

Although the things done in the previous subsection where the temperature was included into the equation of motion through an uncorrelated thermal field, it is still not easy to describe the stochastic LLG equation analytically. In order to come further into the calculations, a switch to collective coordinates is made. In essence the idea is to switch from looking at the magnetic texture $\vec{n}^0(r,t)$ to look at the Néel vector centred at the magnetic structure $\vec{n}^0(r - u(t), t)$. In essence the transformation to be done here is

$$\vec{n}^0(r,t) = \vec{n}^0(r - u(t), t). \tag{5.24}$$

$u(t)$ is here the position of the magnetic structure center, meaning that the position dependant $\vec{n}^0$ is now centered at the structure(domain wall, skyrmion or other stable magnetic structures). Using the chain rule the time derivatives of $\vec{n}$ becomes

$$\begin{aligned} \dot{\vec{n}} &= -\dot{u}_\beta \partial_\beta \vec{n} \\ \ddot{\vec{n}} &= -\ddot{u}_\beta \partial_\beta \vec{n} + \dot{u}_\beta \dot{u}_\gamma \partial_\beta \partial_\gamma \vec{n}. \end{aligned} \tag{5.25}$$

Multiplying the sLLG equation by $\vec{n}^0 \cdot \partial_\alpha \vec{n}^0 \times$ on both sides and rewriting the initial torque expression for n^0 the torque term becomes

$$\begin{aligned} \vec{n}^0 \cdot \partial_\alpha \vec{n}^0 \times \vec{\tau} = -\hbar J_\beta^n \vec{n}^0 \partial_\alpha \vec{n}^0 \times \partial_\beta \vec{n}^0 + \vec{n}^0 \cdot \partial_\alpha \vec{n}^0 \times A(\partial_\beta \rho)\vec{n}^0 \times \partial_\beta \vec{n}^0 \\ -\vec{n}^0 \cdot \partial_\alpha \vec{n}^0 \times 2D\rho\vec{n}^0 \times (\partial_\beta \times \vec{n}^0) + \vec{n}^0 \cdot \partial_\alpha \vec{n}^0 \times \frac{K}{2}\rho(\vec{n}^0 \cdot \hat{r})\vec{n}^0 \times \hat{r} \end{aligned} \tag{5.26}$$

The non-torque terms in equation 5.7 also needs to be rewritten. By introducing the collective coordinates they become

$$\vec{n}^0 \times \left(-\ddot{u}_\beta \partial_\beta \vec{n}^0 + \dot{u}_\beta \dot{u}_\gamma \partial_\beta \partial_\gamma \vec{n}^0 - f^{th} - \frac{\alpha J}{2} \dot{u}_\beta \partial_\beta \vec{n}^0 \right). \tag{5.27}$$

Again, similarly to the torque $\vec{n}^0 \cdot \partial_\alpha \vec{n}^0 \times$ is multiplied from the left and gives

$$\begin{aligned} -\vec{n}^0 \cdot \partial_\alpha \vec{n}^0 \times \vec{n}^0 \ddot{u}_\beta \partial_\beta \vec{n}^0 + \vec{n}^0 \cdot \partial_\alpha \vec{n}^0 \times \dot{u}_\beta \dot{u}_\gamma \partial_\beta \partial_\gamma \vec{n}^0 \\ -\vec{n}^0 \cdot \partial_\alpha \vec{n}^0 \times f^{th} - \vec{n}^0 \cdot \partial_\alpha \vec{n}^0 \times \frac{\alpha J}{2} \dot{u}_\beta \partial_\beta \vec{n}^0. \end{aligned} \tag{5.28}$$

This can be rewritten to

$$\begin{aligned} -\ddot{u}_\beta \partial_\beta \vec{n}^0 \cdot \vec{n}^0 + \dot{u}_\beta \dot{u}_\gamma (\partial_\beta \partial_\gamma \vec{n}^0) \cdot \partial_\alpha \vec{n}^0 \\ -\partial_\alpha \vec{n}^0 \cdot f^{th} - \frac{\alpha J}{2} \dot{u}_\beta \partial_\alpha \vec{n}^0 \cdot \partial_\alpha \vec{n}^0. \end{aligned} \tag{5.29}$$

Then finally the equations of motion in the collective coordinate system has been retrieved. The total equation of motion for the magnetic strucutre center is

$$\begin{aligned} -\ddot{u}_\beta \partial_\beta \vec{n}^0 \cdot \vec{n}^0 + \dot{u}_\beta \dot{u}_\gamma (\partial_\beta \partial_\gamma \vec{n}^0) \cdot \partial_\alpha \vec{n}^0 \\ -\partial_\alpha \vec{n}^0 \cdot f^{th} - \frac{\alpha J}{2} \dot{u}_\beta \partial_\alpha \vec{n}^0 \cdot \partial_\alpha \vec{n}^0 - \hbar J^n_\beta \vec{n}^0 \partial_\alpha \vec{n}^0 \times \partial_\beta \vec{n}^0 \\ +\vec{n}^0 \cdot \partial_\alpha \vec{n}^0 \times A(\partial_\beta \rho) \vec{n}^0 \times \partial_\beta \vec{n}^0 \\ -\vec{n}^0 \cdot \partial_\alpha \vec{n}^0 \times 2D\rho \vec{n}^0 \times (\partial_\beta \times \vec{n}^0) + \vec{n}^0 \cdot \partial_\alpha \vec{n}^0 \times \frac{K}{2} \rho (\vec{n}^0 \cdot \hat{r}) \vec{n}^0 \times \hat{r} = 0. \end{aligned} \tag{5.30}$$

Now that an equation of motion has been found for the magnetic texture in the antiferromagnet the next step would be to integrate over the spatial coordinates to arrive at the stochastic Thiele equations. After doing so it is possible to use a Fokker-Planck equation to retrieve an equation of motion in terms of the probability of $\vec{n}$ at time t. This can in the end be used to find the speed of the domain wall under temperature. This is however not within the grasp of this thesis.

Part II

Easy-plane antiferromagnets as neuromorphic systems

6 The basics of ferromagnetic phase angle spiking

In the previous article discussed in this thesis, artificial neurons were modelled as one-domain antiferromagnets. This is just one example of spintronic artificial neurons and is quite hard to realize experimentally. In this section, the goal is to expand on a more realistic neuronal model. Furthermore, to see how it responds to different perturbations. Firstly, the motivation and theory of "Easy-plane spin Hall nano-oscillators as spiking neurons for neuromorphic computing" [50] are discussed. Secondly, in section 7, the model found there is expanded to use in antiferromagnets. After the expansion to antiferromagnetism is done, the effects of DMI and magnetic field perturbation in the artificial neurons and synapses are done.

6.1 Introduction

It has been shown previously that superconducting Josephson junctions can exhibit spiking behaviour [51, 52]. The spiking phase has been proven to be useful for neuromorphic computing. However, superconducting junctions lack the ease of production and temperature stability to be of any commercial use as of now. T Khymyn et al. have shown that the Josephson junction superconducting phase δ appears in easy-plane spin Hall nano oscillator's(SHNO) order parameter [53]. Therefore, the phase angle can be made to mimic the superconducting phase behaviour and thus can be suitable for neuromorphic computing. These structures can produce spiking voltages in the THz regime, compelling for fast neuromorphic architectures. The behaviour is repeated in antiferromagnetic junctions [54]. This is also shown to be extendible for multiple neurons [50]. In order to further investigate the SHNO structure, the underlying theoretical basis is first presented before these structures are tested numerically to see if they hold the desired neuromorphic properties.

6.2 Experimental setup

6.2.1 Easy-plane spin Hall nano oscillator

As the introduction mentions, the superconducting Josephson junction phase can be found in both antiferro and ferromagnets. The neuronal structure here is a biaxial antiferro/ferromagnet on top of a heavy metal, opposed. As mentioned in the introduction to antiferromagnets (section 2) this ensures spin injection into the system when the heavy metal is passed a current $\vec{j}_e$ with a strong polarization due to spin-orbit coupling.

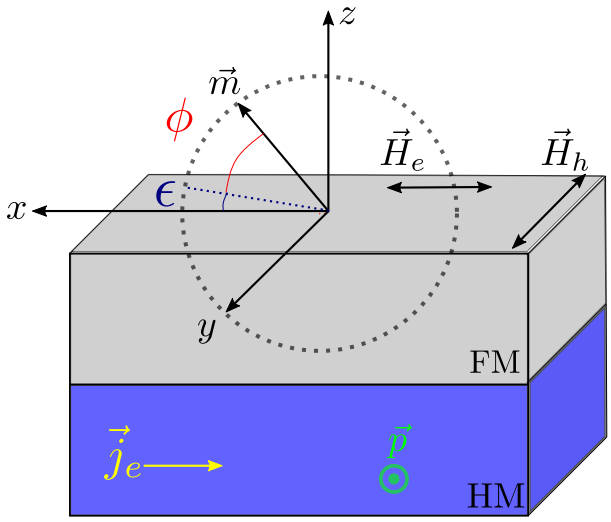

Figure 6.1: This figure is adapted from source [50]. It shows the envisioned neuron structure of source [50]. It has a heavy metal layer(with strong spin-orbit coupling) below a ferromagnetic layer. ϕ shows the magnetization angle within the easy plane, and ϵ is the deviation along the y axis. An electrical current $\vec{j}_e$ along x passes through the heavy metal layer with spin polarization perpendicular to the easy plane in the ferromagnet. H_h shows the direction of the hard axis anisotropy and H_e the direction of the easy axis anisotropy.

Figure 6.1 shows the envisioned neuronal setup in source [50]. The order parameter in the ferromagnetic layer(FM) is constrained to an easy plane through a hard axis anisotropy $\vec{H}_h$ in the y direction. There is an easy-axis anisotropy within the easy plane $\vec{H}_e$. This causes the ferromagnetic order parameter to be constrained in the easy plane, similar to source [40]. There is a slight deviation from the order in the easy plane, ϵ. When an electrical current $\vec{j}_e$ is passed through the heavy metal with a polarization $\vec{p}$ perpendicular to the easy plane, it induces dynamics in the ferromagnetic layer and can cause spiking events. These bilayers are connected to artificial synaptic regions with locally modifiable free energy terms so the spiking probability can be tuned artificially. This is crucial for the network to be trainable.

6.3 Easy plane dynamics for ferromagnetic structures

In order to understand how the physics of the SHNO works in figure 6.1, and how it relates to the phase of a Josephson junction, a thorough description of the governing physics is needed. The basis for the LLG equation was described in section 2, the reader can reference that section for the background of the LLG equation. Starting from the ferromagnetic case, the LLG equation is to reiterate,

$$\dot{\vec{m}} = -\gamma_0 \vec{m} \times \vec{H}_{\text{eff}} + \alpha \vec{m} \times \dot{\vec{m}} + \tau \vec{m} \times (\vec{m} \times \vec{p}). \tag{6.1}$$

Where $\tau = \sigma j$ is the spin torque, j is the current density, α is the Gilbert damping parameter, $\vec{p} = \hat{y}$ is the direction of the spin polarization and $\gamma_0 = \mu_0\gamma$, where μ_0 is the vacuum permeability and γ the gyromagnetic ratio. The SHNO oscillator is tuned so that there is an easy plane in the xz plane, and an easy axis in the x direction. Analogous to what was done in section 2 the anisotropic effects of the system can be modelled through the effective field

$$\vec{H}_{\text{eff}} = H_e\hat{x} - H_h\hat{y}. \tag{6.2}$$

Where H_e is the easy axis anisotropic strength, and H_h the hard axis strength. They relate to the characteristic field frequencies in the following way, $\omega_e = \gamma_0 H_e$ and $\omega_h = \gamma_0 H_h$.

The incident torque τ is polarized in the y direction, $\vec{\tau} = \tau\hat{p} = \tau\hat{y}$. The term entering the derivative $\dot{\vec{m}}$ is the cross product of $\vec{m}$ with $\vec{m} \times \hat{p}$. $\vec{m} \times \hat{p}$ lies in the xz plane, perpendicular to the $\hat{y}$ unit vector. Taking the cross product with a vector in the xz plane gives a derivative contribution in the y axis, tilting the vector slightly away (with an angle ϵ in figure 6.1) from its easy xz plane. When ϵ is non-zero, the torque yields a precessional contribution. When that precessional contribution overcomes the anisotropic easy-axis, the system rotates around the y axis. Going back to figure 6.1, the incident torque gives a precessional contribution to ϕ and spikes when ϕ rotates fully around y.

6.3.1 Relation to Josephson junctions

As in the previous paper [40] if the hard axis anisotropy ω_h is much larger than the easy axis anisotropy $\omega_e \ll \omega_h$ the easy plane precessing phase ϕ parameterizes the order parameter in linear order. Starting again from the free energy consisting of anisotropic exchange and magnetic field interaction

$$F = \int d^3\vec{r}F = \int d^3\vec{r}\left[\sum_i \frac{1}{2}H_i(\vec{m}\cdot\hat{e}_i)^2 - \mu\vec{h}\cdot\vec{m}\right]. \tag{6.3}$$

Here H_i denotes the anisotropic field strength in direction $\hat{e}_i$, μ is the permeability, and $\vec{h}$ is the normalized magnetic field analogous to equation 2.58. The magnetic field is here in the xz plane to be able to complement the anisotropic exchange for fine-tuning the system. This will be further investigated at a later time. For now, it is enough to know that it is there.

The next step is to find how the in-plane phase ϕ evolves over time. In order to do so it is prudent to introduce the rotational matrix R, defined as

$$R = R_z(-\theta)R_y(-\phi). \tag{6.4}$$

The R matrix in equation 6.4 rotates a vector in 3D space with angle $-\phi$ around the y axis and by an angle $-\theta = (\pi/2 + \epsilon)$ around z. Writing the normalized magnetization vector of

figure 6.1 through these angles, the following expression gives the magnetization.

$$\begin{aligned} \vec{m} &= (\cos\phi\sin(\pi/2+\epsilon), \cos(\pi/2+\epsilon), \sin\phi\sin(\pi/2+\epsilon)) \\ \vec{m} &= (\cos\phi\cos\epsilon, \sin\epsilon, \sin\phi\cos\epsilon). \end{aligned} \tag{6.5}$$

When acting on the magnetization vector, equation 6.5, with the rotational matrix in equation 6.4 it simply returns the $\hat{y}$ vector,

$$Rm = \hat{y}. \tag{6.6}$$

This can be seen by subsequently rotating the magnetization vector in figure 6.1 as prescribed with the matrix R. The definition in equation 6.6 can be used to simplify the LLG equation to an angular equation for the order parameter. Starting by inserting the definition of the effective field from equation 6.2. The LLG equation becomes

$$\dot{\vec{m}} = \omega_h m_y \vec{m} \times \hat{y} - \omega_e m_x \vec{m} \times \hat{x} + \alpha \vec{m} \times \dot{\vec{m}} + \tau \vec{m} \times (\vec{m} \times \hat{y}). \tag{6.7}$$

Now applying the rotational matrix R to the LLG equation

$$R\dot{\vec{m}} = \omega_h m_y \hat{y} \times R\hat{y} - \omega_e m_x \hat{y} \times R\hat{x} + \alpha \hat{y} \times R\dot{\vec{m}} + \tau \hat{y} \times (\hat{y} \times R\hat{y}). \tag{6.8}$$

By observing that the left-hand side of equation 6.8 can be written

$$R\dot{\vec{m}} = \partial_t(R\vec{m}) - \dot{R}\vec{m} = -\dot{R}R^T\hat{y}, \tag{6.9}$$

the expression in equation 6.8 can be simplified. Note that the inverse of the rotation matrix is its transpose [55] in order to get the last equality in equation 6.9. A, the matrix product of the derivative of R and R^T itself, $\dot{R}R^T = A$ is asymmetric. Since the magnetization is parameterized by two free variables, due to the fact that $|\vec{m}| = 1$, one can simplify further by choosing two equations from equation 6.8. The most convenient equations to perform further calculations on are the $\hat{z}$ and $\hat{x}$ directions from equation 6.8. These become

$$\begin{aligned} -A_{xy} &= \omega_h m_y R_{zy} - \omega_e m_x R_{zx} + \alpha A_{zy} - \tau R_{xy} \\ &= \omega_h \sin(\epsilon) R_{zy} - \omega_e \cos(\phi)\cos(\epsilon) R_{zx} + \alpha A_{zy} - \tau R_{xy} \\ -A_{zy} &= -\omega_h m_y R_{xy} + \omega_e m_x R_{xx} - \alpha A_{xy} - \tau R_{zy} \\ &= \omega_h \sin(\epsilon) R_{xy} + \omega_e \cos(\phi)\cos(\epsilon) R_{xx} - \alpha A_{xy} - \tau R_{zy}. \end{aligned} \tag{6.10}$$

The rotation matrix when rotating in the manner described above is the following in terms of ϕ and ϵ,

$$R = \begin{bmatrix} -\cos(\phi)\sin(\epsilon) & -\cos(\epsilon) & \sin(\phi)\sin(\epsilon) \\ \cos(\phi)\cos(\epsilon) & -\sin(\epsilon) & -\sin(\phi)\cos(\epsilon) \\ \sin(\phi) & 0 & \cos(\phi) \end{bmatrix}. \tag{6.11}$$

The A matrix can be found by taking $\dot{R}R^T$, and is not shown here. It is done by taking the derivatives and multiplying and the process is quite tedious. Only the matrix components in use are included here. These components are $A_{xy} = \dot{\epsilon}$ and $A_{zy} = -\dot{\phi}\cos(\epsilon)$. Inserting the elements of A and R into equation 6.10 yields

$$\begin{aligned} -\dot{\epsilon} &= -\omega_e \cos(\phi)\cos(\epsilon)\sin(\phi) - \alpha\dot{\phi}\cos(\epsilon) + \tau\cos(\epsilon) \\ \dot{\phi}\cos(\epsilon) &= -\omega_h \sin(\epsilon)\cos(\epsilon) - \omega_e \cos^2(\phi)\cos(\epsilon)\sin(\epsilon) - \alpha\dot{\epsilon} \end{aligned} \tag{6.12}$$

Finally, the equation can be linearized. Assuming small deviations $d\epsilon$ from ϵ when $\omega_e \ll \omega_h$, $\cos\epsilon \approx 1$ and $\sin\epsilon \approx \epsilon$. By doing so, equation 6.12 becomes

$$\begin{aligned} -\dot{\epsilon} &= -\omega_e \cos(\phi)\sin(\phi) - \alpha\dot{\phi} + \tau \\ \dot{\phi} &= -\omega_h\epsilon - \omega_e \cos^2(\phi)\epsilon - \alpha\dot{\epsilon}. \end{aligned} \tag{6.13}$$

Taking the time derivative of the second equation, and using the definition of $\dot{\epsilon}$ in 6.13 an equation for $\ddot{\phi}$ can be found

$$\begin{aligned} \ddot{\phi} &= -\omega_h\dot{\epsilon} + \omega_e(2\dot{\phi}\epsilon\sin(\phi)\cos(\phi) - \dot{\epsilon}\cos^2(\phi)) - \alpha\ddot{\epsilon} \\ &= \omega_h(-\omega_e\cos(\phi)\sin(\phi) - \alpha\dot{\phi} + \tau) + \omega_e(2\dot{\phi}\epsilon\sin(\phi)\cos(\phi) \\ &\quad -(-\omega_e\cos(\phi)\sin(\phi) - \alpha\dot{\phi} + \tau)\cos^2(\phi)) - \alpha\ddot{\epsilon}. \end{aligned} \tag{6.14}$$

Disregarding terms of higher order, $O(\alpha^2)$, $O(\alpha\tau)$ and also keeping terms of maximum linear order in ω_e, meaning negleting terms of $O(\alpha\omega_e)$ this simplifies to

$$\ddot{\phi} = -\omega_h(-\omega_e\cos(\phi)\sin(\phi) - \alpha\dot{\phi} + \tau) + \omega_e(2\epsilon\dot{\phi}\cos(\phi)\sin(\phi)). \tag{6.15}$$

Now from the equation for $\dot{\phi}$ above(equation 6.13), $\epsilon \approx \dot{\phi}/\omega_h$ to leading order. Inserting this into equation 6.15, it becomes

$$\ddot{\phi} = -\omega_h(-\frac{\omega_e}{2}\sin(2\phi) - \alpha\dot{\phi} + \tau) + \frac{\omega_e}{\omega_h}\dot{\phi}^2\sin(2\phi). \tag{6.16}$$

Finally, rearranging the terms of equation 6.16,

$$\frac{1}{\omega_h}\ddot{\phi} + \alpha\dot{\phi} + \frac{\omega_e}{2}\left(1 + \frac{2}{\omega_h^2}\dot{\phi}^2\right)\sin(2\phi) = \sigma j. \tag{6.17}$$

Where $\tau = \sigma j$. When changing variables under $\delta = 2\phi$ the equation for a superconducting phase angle δ can be obtained when neglecting the $\dot{\phi}^2$ term

$$\ddot{\delta} + \frac{1}{RC}\dot{\delta} + \frac{2eI_c}{\hbar C}\sin\delta = \frac{2e}{I_c}I. \tag{6.18}$$

With R, the resistance, C, the capacitance and critical current I_c. Equation 6.18 also holds for a damped and driven pendulum, although the constants in front are not of an

electrical manner. In addition, equation 6.17 is similar to the equation of motion for an antiferromagnetic oscillator under $\frac{\omega_e}{\omega_h^2}\dot{\phi}^2 \to 0$

$$\frac{1}{\omega_{ex}}\ddot{\phi} + \alpha\dot{\phi} + \frac{\omega_e}{2}\sin 2\phi = \sigma j. \tag{6.19}$$

Which is shown in detail later. The hard axis anisotropy ω_h gives a similar inertial term as the exchange coupling ω_{ex} does in the antiferromagnetic case. In the limit where $\omega_e \ll \omega_h$ the precession dynamics are dominated by the hard axis, $\dot{\phi} \sim \omega_h$ [50] so that

$$\frac{\omega_e}{\omega_h^2}\dot{\phi}^2 \sim \omega_e. \tag{6.20}$$

The restoring force contribution differs by a factor of 2 in the precessional state vs. the relaxed states. However, the spiking behaviour is not affected largely by it, as the dynamics are close to the antiferromagnetic counterpart.

6.3.2 Another approach to equation 6.17

The equation of motion in 6.17 can also be found in another manner by expanding the magnetization in the m_y parameter and inserting it into the LLG equation. $\vec{m} = (\cos(\phi), m_y, \sin(\phi))$, where it was assumed that m_y is so small that there is no need for a length renormalization of the x and z component. Then the following three equations can be found by inserting the vector definition in the LLG,

$$\begin{aligned} -\dot{\phi}\sin\phi &= -\omega_h m_y \sin\phi + \alpha(m_y\dot{\phi}\cos\phi - \dot{m}_y\sin\phi) + \tau m_y\cos\phi \\ \dot{m}_y &= -\omega_e\cos\phi\sin\phi - \alpha\dot{\phi} + \tau \\ \dot{\phi}\cos\phi &= \omega_h m_y\cos\phi + \omega_e\cos\phi m_y + \alpha(\dot{m}_y\cos\phi + m_y\dot{\phi}\sin\phi) + \tau m_y\sin\phi. \end{aligned} \tag{6.21}$$

By multiplying by $-\sin\phi$ in the first equation and by $\cos\phi$ in the third equation and summing the two contributions an equation for $\dot{\phi}$ can be found

$$\dot{\phi} = -\omega_h m_y - \omega_e\cos^2\phi m_y - \alpha\dot{m}_y \tag{6.22}$$

With the m_y component in equation 6.21 is the same set of equations as in equation 6.13 and therefore the same expansion and simplification method as previously used can be used to find equation 6.17.

6.4 Numerical verification of neuromorphic properties

In order to show that the spiking properties are present in the biaxial ferromagnetic system, a macro-spin approximation is first used before going to more realistic micromagnetic simulations. The macro-spin approximation is just a proof of concept. In order to show that

it is possible to achieve neuromorphic spiking observe from equation 6.17 that ϕ has a fixed point at $\phi^* = \arcsin(2\tau/\omega_e)/2$. This can be seen when setting $\dot{\phi}$ and $\ddot{\phi}$ to 0 in equation 6.17

$$\frac{\omega_e}{2}\sin(2\phi^*) = \tau. \tag{6.23}$$

Equation 6.23 only has a real solution when $2\tau \leq \omega_e$. It has a vertical asymptote at $\pi/4$. If one moves the phase angle beyond this point, it will generate a 2π phase shift of the order parameter. By tuning the fixed point ϕ^* as close to the asymptote as possible, the spiking dynamics can be arbitrarily sensitive to incoming torques.

However, suppose one wants to have coherent single spike events. In that case, α must be large enough so that one does not arrive at an auto-oscillation regime when a spiking torque is injected. The problem is that in a real system, one wants a small Gilbert damping parameter to ensure signal flow.

In order to show that the spiking behaviour is present, the following lattice is used. One input neuron with phase angle ϕ_0 is connected to a 3x3 synapse, which is again connected to an output neuron with a phase angle of ϕ_1. Every spin is connected to its neighbours by an exchange interaction $J\vec{S}_i \cdot \vec{S}_j$. This basic setup is shown in figure 6.2.

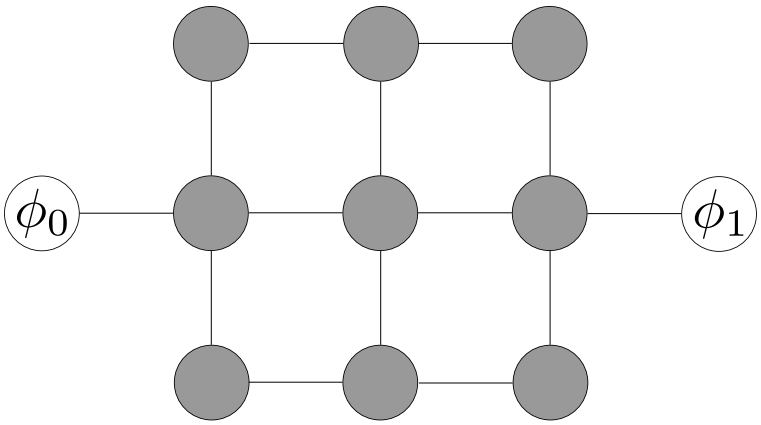

Figure 6.2: This figure is adapted from source [50]. It shows the network structure used in the simplest simulations in this chapter. An input macrospin with in plane phase angle ϕ_0 is connected to a 3×3 synaptic structure with an output macrospin with phase angle ϕ_1. Black lines show where the macrospins interact.

Now, to show spiking behaviour, the macrospin neurons, denoted ϕ_1 and ϕ_2 are under a hard y axis anisotropy and a smaller easy axis in the x direction ~ 0.05 of the hard y axis. The bulk, denoted by gray circles in figure 6.2 are under an easy axis in z and y, ~ 0.05 and

~ 0.1 respectively. The lines in figure 6.2 shows where there is a simple exchange interaction $F_{ex} = Jm_i \cdot m_j$ with $J = 0.31H_h$, where H_h is the hard axis anisotropic strength in the neuron macrospin. The first neuron can be spiked by injecting a background current under the auto-oscillation regime in the input neuron ϕ_0 and subsequently adding pulses of 10%. The spiking of the first neuron subsequently causes the second neuron to spike. This is shown through plotting the $\sin^2$ of both phase angles in figure 6.3.

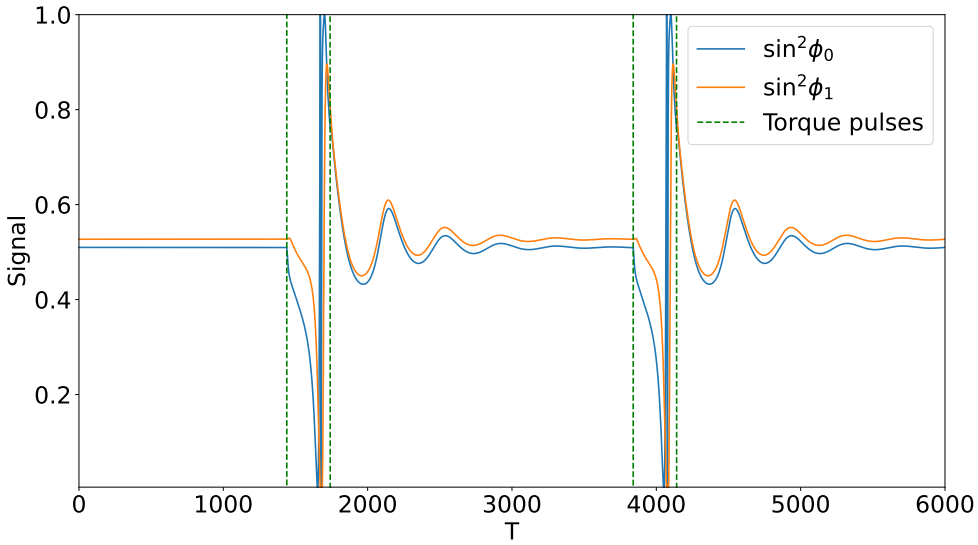

Figure 6.3: The figure shows the $\sin^2$ of both macrospin neurons under the conditions described above. It is clear that the dynamics of ϕ_0 determines the dynamics of ϕ_1 and hence the signal of ϕ_0 travels through the bulk.

Although the above model is quite simplified, it shows that injecting spin currents into the system can cause spiking behaviour, which is an essential concept for the later, more realistic models.

7 Antiferromagnetic easy plane neuromorphic systems

Now that the result of source [50] has been established for ferromagnets, an extension to the antiferromagnetic regime is needed. As mentioned in the above section, the antiferromagnetic LLG equation also follows the superconducting Josephson phase under certain conditions. To see why that is, a similar derivation to the ferromagnetic equivalent is done here, starting from the free energy density in equation 7.1.

7.1 Details of the antiferromagnetic angular equation

The free energy of an antiferromagnet in terms of two sublattices a and b is to reiterate

$$\begin{aligned} f_{ex} &= \omega_{ex}\vec{m}_a \cdot \vec{m}_b + \frac{A^{(1)}}{2}\left[(\nabla\vec{m}_a)^2 + (\nabla\vec{m}_b)^2\right] + A^{(2)}(\nabla\vec{m}_a \cdot \nabla\vec{m}_b) \\ f_{ani} &= \sum_{\hat{e}_i} \frac{\omega_i^{(1)}}{2}\left[(\vec{m}_a \cdot \hat{e}_i)^2 + (\vec{m}_b \cdot \hat{e}_i)^2\right] + \omega_i^{(2)}\vec{m}_a \cdot \hat{e}_i\vec{m}_b \cdot \hat{e}_i \\ f_Z &= -\omega_Z\vec{h} \cdot (\vec{m}_a + \vec{m}_b). \end{aligned} \tag{7.1}$$

Where ω_{ex}, $A^{(1/2)}$, $\omega_i^{(1/2)}$, ω_Z and $\vec{h}$ are the characteristic exchange frequency, the inhomogeneous exchange stiffness, the anisotropic energy strength in direction $\hat{e}_i$, the magnetic field strength, and the normalized magnetic field respectively. By introducing $\vec{n} = (\vec{m}_a - \vec{m}_b)/2$ and $\vec{m} = (\vec{m}_a + \vec{m}_b)/2$ as well as the following constraints, $|\vec{m}_i| = 1$, $\vec{m} \cdot \vec{n} = 0$ and $\vec{m}^2 + \vec{n}^2 = 1$ the free energy becomes the following in terms of $\vec{n}$ and $\vec{m}$

$$\gamma_0 f(\vec{m}, \vec{n}) = -\omega_{ex}\vec{n}^2 + A(\nabla n)^2 + \sum_{\hat{e}_i} \omega_i(\vec{n} \cdot \hat{e}_i)^2 - \omega_Z\vec{h} \cdot \vec{m}. \tag{7.2}$$

Where $A = A^{(1)} - A^{(2)}$ and $\omega_i = \omega_i^{(1)} - \omega_i^{(2)}$. The details of this is explained in section 2. To get the antiferromagnetic equation in equation 6.19 an easy and hard axis anisotropy, in addition to the sublattice exchange energy, is included in the free energy. This leads to the following simplification in the free energy density

$$\gamma_0 f(\vec{m}, \vec{n}) = -\omega_{ex}(\vec{n})^2 - \omega_e(\vec{n} \cdot \hat{x})^2 + \omega_h(\vec{n} \cdot \hat{y})^2 - \omega_Z\vec{h} \cdot \vec{m}. \tag{7.3}$$

The effective field is defined as $\vec{H}_{\vec{q}} = \frac{\delta f}{\delta \vec{q}}$, where $\vec{q}$ is either $\vec{m}$ or $\vec{n}$. The effective fields become

$$\begin{aligned} \gamma_0\vec{H}_{\vec{n}} &= \omega_{ex}\vec{n} + \omega_e\vec{n} \cdot \hat{x} - \omega_h\vec{n} \cdot \hat{y} \\ \gamma_0\vec{H}_{\vec{m}} &= \omega_Z\vec{h}. \end{aligned} \tag{7.4}$$

By adding the two coupled equations mentioned in section 2 in equation 2.48, and by subtracting them one can arrive at the LLG equation in terms of the magnetization $\vec{m}$ and Nèel

vector $\vec{n}$. The two defining equations of motion then becomes

$$\begin{aligned}\dot{\vec{m}} &= -\gamma_0(\vec{m}\times\vec{H}_{\vec{m}} + \vec{n}\times\vec{H}_{\vec{n}}) + \alpha(\vec{m}\times\dot{\vec{m}} + \vec{n}\times\dot{\vec{n}}) + \tau(\vec{m}\times\vec{m}\times\hat{p} + \vec{n}\times\vec{n}\times\hat{p}) \\ \dot{\vec{n}} &= -\gamma_0(\vec{n}\times\vec{H}_{\vec{m}} + \vec{m}\times\vec{H}_{\vec{n}}) + \alpha(\vec{m}\times\dot{\vec{n}} + \vec{n}\times\dot{\vec{m}}) + \tau(\vec{n}\times\vec{m}\times\hat{p} + \vec{m}\times\vec{n}\times\hat{p}).\end{aligned} \tag{7.5}$$

When expanding the Néel order parameter into a function of ϕ assuming high antiferromagnetic order(i.e. $|\vec{n}| = 1$) as was done to the magnetization $\vec{m}$ in the ferromagnetic case, the Néel vector can be written as

$$\vec{n} = (\sqrt{1-n_y^2}\cos\phi, n_y, \sqrt{1-n_y^2}\sin\phi). \tag{7.6}$$

As mentioned previously when there is high antiferromagnetic order the magnetization and the Néel order parameter are perpendicular, $\vec{m}\cdot\vec{n} = 0$, the magnetization parameter can be written as a $\pi/2$ phase shift of the Néel vector

$$\vec{m} = (-|m|\sin\phi, m_y, |m|\cos\phi). \tag{7.7}$$

The previous condition that $|\vec{m}| = 1$ is of course not present any longer under high antiferromagnetic order, so the magnetization carries a small length component $|m|$ in order to rescale the magnetization. There are now six defining equations of motion that can be reduced to find the Josephson like equation 6.19, one equation for each direction in equation 7.5. It will suffice to only look at the y direction in the magnetization and the x and z direction in the Néel order parameter. The equation for $\dot{m}_y$ can be found by insetting the effective field in equation 7.4 into equation 7.5 and isolating m_y terms. It becomes

$$\dot{m}_y = -\omega_Z\cos\phi - \omega_e\sin\phi\cos\phi - \alpha\dot{\phi} + \tau. \tag{7.8}$$

By the similar procedure the equations of motion in the x and z direction can be found for the Néel vector when ignoring terms of order $|m|^2$,

$$\begin{aligned}-\dot{\phi}\sin\phi &= -m_y\omega_{ex}\sin\phi + |m|\cos\phi\omega_{ex}n_y \\ +\alpha(m_y\dot{\phi}\cos\phi - |m|\cos\phi\dot{n}_y - n_y|m|\dot{\phi}\sin\phi - \sin\phi\dot{m}_y) &+ \tau(-n_y|m|\sin\phi + m_y\cos\phi)\end{aligned} \tag{7.9}$$

$$\begin{aligned}\dot{\phi}\cos\phi &= n_y\omega_Z + |m|\sin\phi\omega_{ex}n_y - |m|\sin\phi\omega_h n_y + m_y\omega_{ex}\cos\phi + m_y\omega_e\cos\phi \\ +\alpha(-|m|\sin\phi\dot{n}_y + m_y\dot{\phi}\sin\phi + \cos\phi\dot{m}_y + n_y|m|\dot{\phi}\cos\phi) &+ \tau(n_y|m|\cos\phi + m_y\sin\phi).\end{aligned}$$

With a multiplication of $-\sin\phi$ in the first term of equation 7.9, and $\cos\phi$ in the second equation and an addition of both, an equation for $\dot{\phi}$ when ignoring small terms of order $|m|n_y$ can be recovered

$$\dot{\phi} = n_y\omega_Z\cos\phi + m_y\omega_{ex} + m_y\omega_e\cos\phi + \alpha\dot{m}_y. \tag{7.10}$$

Taking the derivative of equation 7.10 yields

$$\ddot{\phi} = \dot{n}_y\omega_Z \cos\phi - n_y\omega_Z\dot{\phi}\sin\phi + \dot{m}_y\omega_{ex} + \dot{m}_y\omega_e\cos\phi - m_y\omega_e\dot{\phi}\sin\phi + \alpha\ddot{m}_y. \tag{7.11}$$

For now ignoring the magnetic field, by setting $\omega_Z = 0$ the equation simplifies to

$$\ddot{\phi} = \dot{m}_y\omega_{ex} + \dot{m}_y\omega_e\cos\phi - m_y\omega_e\dot{\phi}\sin\phi + \alpha\ddot{m}_y. \tag{7.12}$$

Now insetting $\dot{m}_y$ from equation 7.8 gives an equation for $\ddot{\phi}$ only dependent on ϕ

$$\ddot{\phi} = \omega_{ex}(-\frac{\omega_e}{2}\sin 2\phi - \alpha\dot{\phi} + \tau) + \omega_e((\frac{\omega_e}{2}\sin 2\phi - \alpha\dot{\phi} + \tau)\cos\phi - 2m_y\cos\phi\sin\phi\dot{\phi}). \tag{7.13}$$

Similarly to the ferromagnetic case the easy axis resonance ω_e is small compared to the exchange frequency ω_{ex} in the system, meaning that terms proportional to ω_e^2, $\omega_e\alpha$ and $\omega_e\tau$ can be dropped. The last term in equation 7.13 contains three terms $\sim m_y\dot{\phi}$ which all become small as they are subsequently proportional to m_y^2 and $\alpha m_y\dot{m}_y$. Rewriting the remainding part of the equation the Josephson junction like equation for an antiferromagnet can be retrieved

$$\frac{\ddot{\phi}}{\omega_{ex}} + \frac{\omega_e}{2}\sin 2\phi + \alpha\dot{\phi} = \tau. \tag{7.14}$$

Now that it has been shown that the antiferromagnetic angle follows Josephson junctions, it is possible to move over to a more comprehensive numerical analysis. The macrospin approximation in section 6 is not performed here, as the essential equation is the same. Instead, micromagnetic simulations are performed directly.

7.2 Nanoconstrictions building-blocks for spiking neural networks

The macrospin model in section 6 proved helpful in showing that spiking behaviour is possible. It being quite a simplified model, it is prudent to move to a more realistic model to see if the spiking behaviour can be reproduced. Since the main interest of this thesis is in the field of antiferromagnetic spintronics, this will be the focus of further simulations. In source [50] they use nanoconstrictions to create an easy axis within an easy plane. This is because the demagnetization field associated with the dipole interaction causes an effective hard axis in the constraining direction in ferromagnets. By constricting the geometry in, for example, the y direction, the magnetization is forced to lie in the xz plane [56].

In antiferromagnets, this demagnetization field does not manifest in the same way. However, there are materials with the desired type of anisotropy to reproduce the previous phase angle equation, Hematite being one of them [57]. Although the absence of the demagnetization field means that the structure does not need to be constricted anymore, there are reasons for using a similar structure. The main reason is that it is convenient to have a larger synaptic

region where magnetic properties can be modified locally. In addition, when connecting multiple neurons into a single synaptic region, it is prudent to have them as narrow as possible.

A discontinuity in magnetic properties can affect spin-wave propagation. Similar to wave propagation over interfaces of differing permittivity in classical electrodynamics. There are some choices in which magnetic properties to tune in the synaptic island. It has been shown that by adding an iron layer on top/bottom of thin layer NiO antiferromagnets, the magnetic anisotropy in the antiferromagnetic layer can be tuned by thickness and small magnetic fields in the Fe layer [58]. For ferromagnets, it has been shown that anisotropic effects can be modified with an application of electric fields [59] and that the dampening coefficient can be modified by ion radiation [60]. The preferred method for this thesis is to modify anisotropic effects locally. This is done artificially throughout the simulations.

From the two primary components, the artificial neurons and synapses, it is crucial that they can incorporate a few base operations. Firstly, a neuron should spike dependent on the temporal coherence of more than one incoming signal. This leads to greater control of the training process and the possibility of summing layers into fewer nodes, incorporating the leaky integrate and fire effect. Secondly, neuronal signals need to pass to more than one neuron. It is common for neural networks to have more nodes in hidden layers than input and output layers. This leads to more adjustability of the network structure.

Before moving on to the numerical results and structures, the basics of signal detection in antiferromagnets are discussed before the experimental setup is further explored. The mentioned components are numerically verified to see that the basic operating principles apply to the antiferromagnetic structures discussed here.

7.3 Signal detection in antiferromagnetic structures

7.3.1 Anisotropic magnetoresistance

In order to read the magnetization dynamics of the system, one could use the anisotropic magnetoresistance effect (AMR). It has been found that in multilayers and magnetic materials, for example, a heavy metal under an antiferromagnet, the orientation of magnetization can be measured [61].

When passing a current through the material, the orientation of magnetization with the polarization in the heavy metal leads to differing resistance. The difference to the null resistance $R(0)$ is proportional to $\sin^2$ of the phase angle [50]. This is known as anisotropic

magnetoresistance. For magnetization states that are confined to the easy plane with a phase angle, ϕ this can be written as [50]

$$R(\phi) - R(0) \sim \sin^2(\phi). \tag{7.15}$$

The measuring length is assumed to be smaller than the exchange coherence length. Therefore, a spike in a neuronal oscillator is equivalent to a phase angle rotation of the local order parameter ϕ by π, which becomes measurable in the resistance. Propagation through the system happens when a spike in neuron 1 propagates through the system to spike neuron 2, modifying the resistance locally.

There are alternatives to regular anisotropic magnetoresistance. In addition to the regular effect described above, which bases itself on that the material is conducting, an effect can also be found in insulators. This is called the spin hall anisotropic magnetoresistive effect (SH-AMR). The effect is shown schematically in figure 7.1.

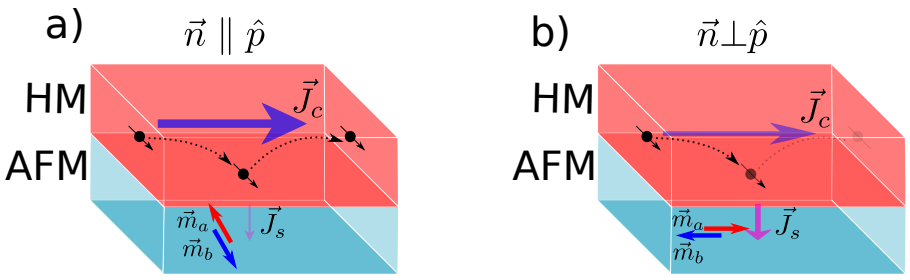

Figure 7.1: Figure a shows how the charge current $\vec{J}_c$ is strengthened when $\vec{n} \parallel \hat{p}$ through backscattering of spin hall affected polarized current. Figure b shows how the charge current is smaller due to the spin accumulation inserted in the antiferromagnetic layer when $\vec{n} \perp \hat{p}$.

SH-AMR manifests in the same way as the regular AMR, namely that the resistance is a function of the in-plane phase angle ϕ. In figure 7.1 two different orientations are shown of the sublattice magnetizations $\vec{m}_a$ and $\vec{m}_b$. The heavy metal layer's current density travels in the x direction. The electrical current is polarized due to spin-orbit coupling. Since the spin current is polarized, the hall effect causes a spin current towards the antiferromagnetic layer. At the interface, spin-current is injected into the antiferromagnet. The amount of spin current injected depends on the orientation of the sublattice magnetization. If more spin current is injected, the charge current $\vec{J}_c$ is smaller, effectively increasing the resistance in

the heavy metal. If the polarized current backscatters on the interface, the current remains larger, and the resistance becomes smaller than the non-backscattering orientation. The benefit of this type of anisotropic magnetoresistance is that it does not need a metallic conducting magnetic layer. The magnetic material can be an insulator and can be both antiferro and ferromagnetic.

7.3.2 Tunneling magnetoresistance and Giant magnetoresistance

In addition to the above-mentioned anisotropic magnetoresistance, two more effects can be used to detect magnetization dynamics in the material. Those are the tunnelling magnetoresistance(TMR) and giant magnetoresistance(GMR) effects. These effects are usually of larger amplitude [50]. They are both an effect observed when adding multilayers of magnetic and non-magnetic materials on top of the phase angle to be detected. The TMR is observed when the middle layer is a thin film insulator, and GMR when it is a regular metallic material.

The derivation and discussion of these effects are not of interest in this thesis. The important thing here is that the resulting resistance is a function of the in-plane phase angle in the magnetic material

$$R = R(\phi) - R(0). \tag{7.16}$$

Therefore, in the following derivation and component tests, this phase angle is measured since this angle will enter the resistance measurements for a real system. No matter the measurement method.

7.4 Numerical setup

Now that the operating principles and concept have been established, the next step is to discuss the numerical setup. The structure of the nanoconstriction network is similar to that of source [50], but it differs in some key areas. Firstly, as mentioned previously, the work done in source [50] is in the field of ferromagnets. Here, the simulations performed are antiferromagnetic. Homogeneous DMI has also been included to see the effect of adding such a term. The homogeneous DMI vector $\vec{d}$ is along the hard axis anisotropy. In addition, it was found that it was prudent to widen the neuronal channels to increase the amount of torque on the synaptic islands. Lastly, tails were added to decrease the effect of backscattering on the system's edges. The step of adding tails is realistic, as no neuron is here meant to work as a single entity. The method of torque injection is similar to that of source [50], however, it was found that there should be a torque injection method for the middle of the synaptic region as well. This was in order to achieve fan-out behaviour. To reiterate, the free energy

of such an antiferromagnetic structure is

$$\begin{aligned} F = -\omega_{ex}\vec{m}_a \cdot \vec{m}_b + \frac{A^{(1)}}{2}((\nabla\vec{m}_a)^2 + (\nabla\vec{m}_b)^2) + A^{(2)}(\nabla\vec{m}_a \cdot \nabla\vec{m}_b) \\ + \frac{\omega^{(1)}}{2}((\vec{m}_a \cdot \hat{e})^2 + (\vec{m}_b \cdot \hat{e})^2) + \omega^{(2)}(\vec{m}_a \cdot \hat{e})(\vec{m}_b \cdot \hat{e}) \\ + \vec{d} \cdot \vec{m}_a \times \vec{m}_b. \end{aligned} \tag{7.17}$$

Where $\hat{e} = \hat{y} + \hat{x}$ and $\omega^{(1/2)}$ are matrices. More details of equation 7.17 can be found in section 2. Schematically, the geometry and setup is repeated in figure 7.2. Similar to the structure in source [50] the neuron is 300 nm, and widened to 80 nm in this case. The synaptic region is diamond shaped and 300 nm by 540 nm.

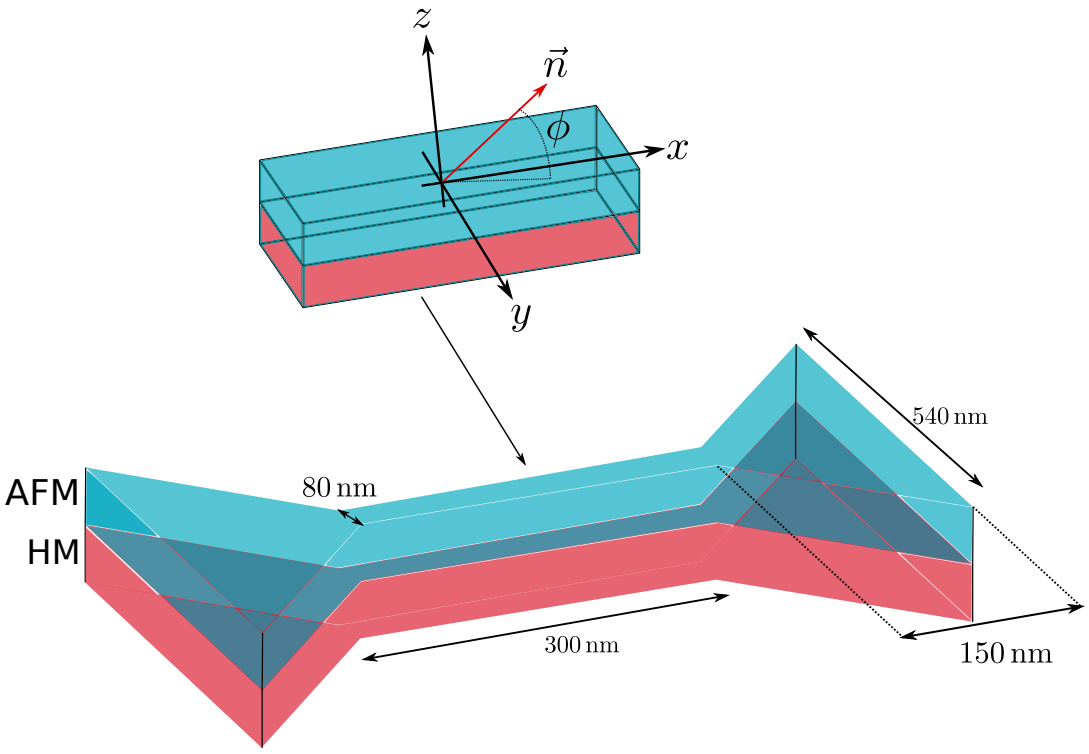

Figure 7.2: The figure shows the nano constriction setup with the antiferromagnet in blue and the heavy metal in red, with dimensions. The Néel vector is also shown in the neuronal structure, with phase angle ϕ from the x axis. There is a hard axis anisotropy in the y direction, and an easy axis in the x directions, the dynamics of ϕ follow equation 7.14.

7.4.1 Software

The software used is a program developed by myself and Viroshaan Uthayamoothy in collaboration with Alireza Qaiumzadeh [18]. The program implements arbitrary two-dimensional antiferromagnetic geometries and utilizes Neumann boundary conditions with

$$\dot{\vec{m}}_i(\Gamma) = 0. \tag{7.18}$$

Where Γ is the geometry's boundary coordinates, no current flow across the boundary is allowed in the system. The program also simulates the LLG equation in its normalized form, following the sublattice normalization of section 2, if the results are to be repeated. The system constants are summarized in table 2.

Variable	Value
ω_{ex}	6.4
$A^{(1)}$	1.2
$A^{(2)}$	0.4
ω_y	5.4×10^{-1}
ω_x	5.4×10^{-2}
d_x	2.7×10^{-2}
α	1×10^{-4}

Table 2: This table shows the values chosen for the parameters when simulating the nanoconstriction components found in this section. They are all normalized by a factor M_s to fit directly into the simulations program used here [18].

7.5 Spiking current threshold

For the biaxial nanoconstriction network, with the incident torque τ as in equation 2.56, some differing effect happens depending on the strength of J in equation 2.20. For now, denoting the current prefactor as I_0, the incident torque strength becomes $I_0 I = \tau$. As mentioned, the incident torque is due to an adjacent heavy metal with spin polarization in the x direction. Injecting torque in the system gives a tilt of each magnetization vector $\vec{m}_A$ and $\vec{m}_B$ away from the easy plane. When there is a non-zero tilting, the torque yields a precessional derivative contribution in the easy plane. Only when this contribution can overcome the easy axis anisotropy can the system be made to spike. The expected behaviour is the following: for low currents, the system stays close to the ground-state state, but when the current amplitude reaches a certain point, rotations of the order parameter start to happen. This effect is observed in figure 7.6.

7.6 Tuning signal propagation through discontinuity in magnetic properties

7.6.1 Anisotropic effects

In order to first establish that it is possible to tune magnetic transmission through modifying the magneto crystalline anisotropy, a two-neuron setup is used (i.e., the double of figure 7.2). First, the initial neuron is spiked using an incident polarization current in the y direction of the heavy metal. This causes precessional motion of the order parameter in the first neuron. The goal is that this precessional motion travels as a spin wave through the synaptic structure and spikes the second neuron. After this behaviour has been shown, the goal is to modify the synaptic anisotropy to see that it hinders the spike propagation.

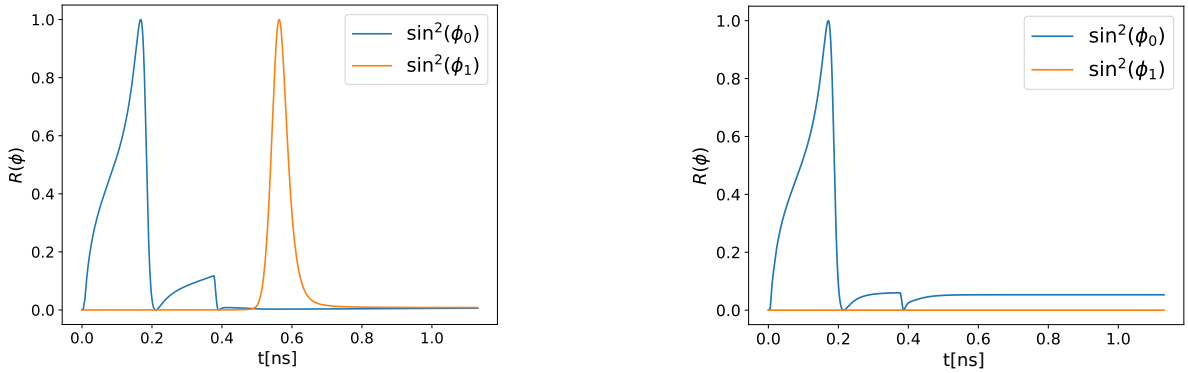

(a) Single spike transmission

(b) Single spike reflection

Figure 7.3: The figure shows the subsequent spiking of neuron 2 with phase angle ϕ_1 due to an incident spin current in neuron 1 with phase angle ϕ_0 and a spike time of 0.4 ns. This is altered when the anisotropic properties are changed in the synapse in figure 7.3a. In figure 7.3b the anisotropic easy axis in the synaptic region is changed, this disrupts the spin wave flow.

In figure 7.3a the input neuron rotates and causes a spike in the second neuron. From figure 7.3a it can be seen that the incident neuron is over-rotated slightly between 0.2 ns and 0.4 ns. During the numerical analysis, it was found that without doing so, the phase rotation induced in ϕ_0 unwinds after the current pulse rather than propagating completely to the output neuron. When modifying the easy axis local anisotropy in the synaptic region by 10%, the incident phase ϕ_0 completes a π rotation, but the signal does not propagate through the synaptic region. This is seen in figure 7.3b. As seen in figure 7.3b ϕ_0 does not completely relax to zero after the π rotation. This is due to some remnant structure in the

input neuron. It was found that it does not affect the next incoming torque pulse when "reusing" the same input. Then, by biasing the synaptic region with a different anisotropic constant, it is possible to tune the spike propagation in the system. Thereby tuning the sensitivity to incoming spikes.

It was also found numerically that numerous incoming spikes can be divided into a single outgoing spike, meaning that the outgoing pulse can be tuned to a point where it is dependent on the frequency of incoming pulses. As mentioned in section 3 this is close to biological spiking.

7.7 Signal summation

By connecting two artificial neurons into a single synaptic region, it is possible to show that the system can perform signal summation. As mentioned in the section's introduction, this is crucial to incorporate to use the structure in figure 7.2 as building blocks for spiking neural networks. In addition to summing two simple signals, it should be possible for the synaptic region not to spike when there is one incident signal and spike when there are two incoming signals, and by doing so, performing an integration over incoming signals. In order to test that these effects are present, the system is set up in the following way. Two neurons are connected into a single synaptic region with a single output neuron. First, the anisotropic easy axis in the synaptic region is tuned so that the output neuron does not spike when only one input neuron is spiked. Secondly, two input neurons are spiked with the same tuning in the synaptic region to see if the fact that they both simultaneously spike causes the output neuron to spike. The results are shown in figure 7.4.

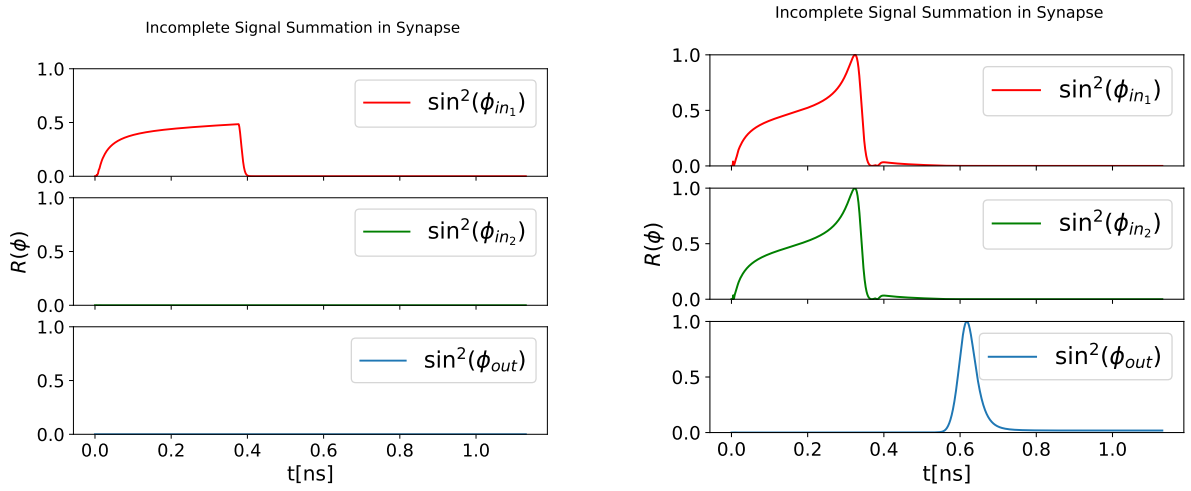

(a) Incomplete signal summation

(b) Complete signal summation

Figure 7.4: From figure 7.4a it is possible to see that when one input neuron ϕ_{in_1} is spiked the signal does not pass through the synaptic region to the output neuron ϕ_{out}, this holds true for a single spike in both input neurons. Only when both input neurons are spiked ϕ_{in_1} and ϕ_{in_2} causes a spike in the output neuron ϕ_{out}. This is shown in figure 7.4b.

As seen in figure 7.4a when a single signal is passed to ϕ_{in_1} it does not cause a spike in ϕ_{out}. The procedure was repeated for ϕ_{in_2} as well, but that is not included here. The results are equal to figure 7.4a. As seen in figure 7.4a the incoming signal lies close to the fix point of $\pi/4$ mentioned in equation 6.23. This was achieved with the signal spike modification of anisotropy found in the single spike experiment (figure 7.3a), 10%.

When leaving the synaptic region at the modified anisotropy of 10% and passing a torque to both input neurons, it was found that the output neuron ϕ_{out} spikes. This can be seen in figure 7.4b. If the signals are not close in time, they mimic the behaviour of figure 7.4a.

Numerically, the output neuron has been shown to only spike when two incoming signals are close in time, thus incorporating the leaky integrate and fire effect, which is crucial for time-dependent neural structures.

The fan-out structure is the subsequent important building block for an antiferromagnetic spiking neural network, which means the ability of one neuron to spike multiple neurons.

7.8 The fan out structure

In order for spintronic components to be able to represent neural network structures properly, it is important that nodes can be added to layers. In order for that to be possible, a single neuron needs to be able to expand its signal to multiple neurons. This mimics a neural network if there are more nodes in the hidden layer than the input layer. In order to show that this is possible, the effect is tested numerically here. The concept is as follows, a single input neuron is spiked, leading to two subsequent spikes in two neurons after passing the signal through a synaptic region.

Given the single spike transmission current used in figure 7.3a, some modification needs to be made to the synaptic region in order to ensure spike propagation to both output neurons. Therefore, the synaptic region is biased with a background current of 65% of the spiking threshold. If the bias is present in the synapse, the spiking of the two subsequent neurons occurs. Intuitively, this makes sense, as the threshold is placed precisely where it causes the spiking event of the output neuron. Spiking two neurons should require additional energy. This fact has been shown during numerical simulations.

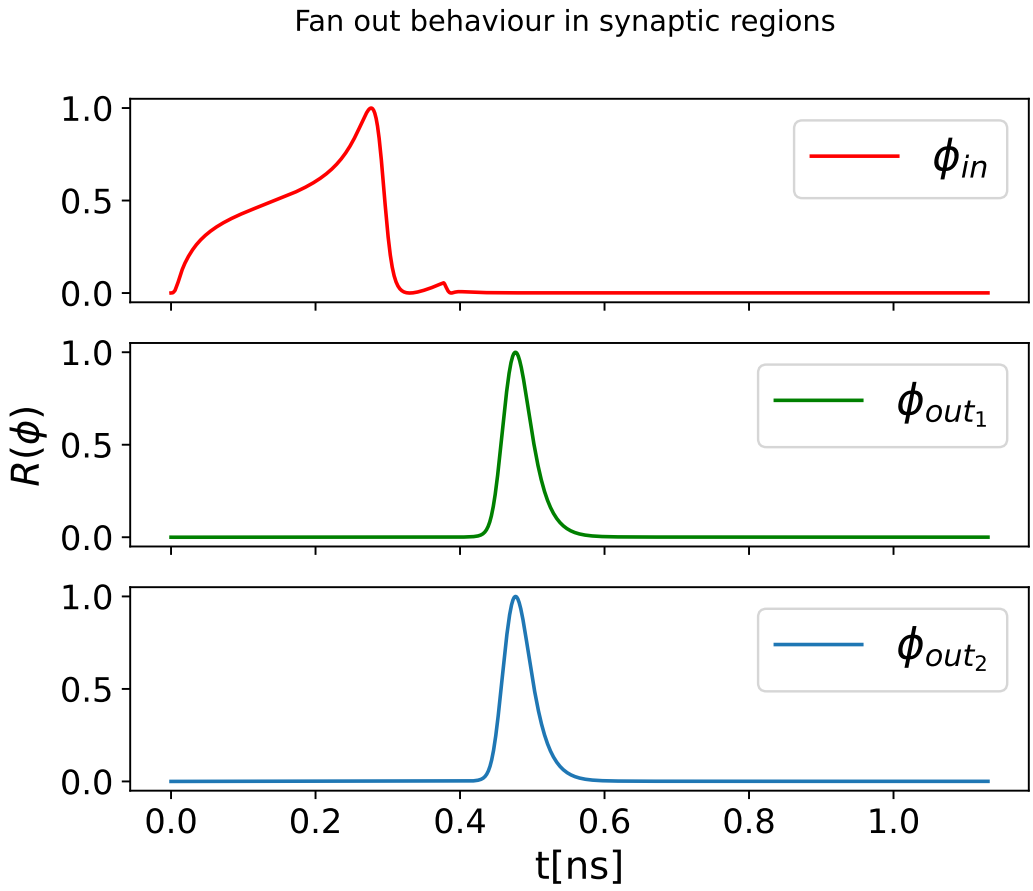

Figure 7.5: When biasing the synaptic region where an input neuron fans out to two neurons with a current below the spiking threshold of the system, it is evidently possible to divide the signal for further transport.

As seen in figure 7.5 the spike in ϕ_{in} causes spiking events in the two output neurons, ϕ_{out_1} and ϕ_{out_2}. The behaviour is crucial if the neuromorphic components found here are to be used for spiking neural networks.

7.9 Effects of DMI on spike propagation

Some antiferromagnetic materials, for example, Hematite, have a DMI at room temperature. As mentioned previously, DMI can give a net magnetization to the ground state of an antiferromagnetic system by tilting $\vec{m}_a$ and $\vec{m}_b$ away from its easy axis. In Hematite, above the Morin temperature, the DMI vector $\vec{d}$ is along the hard axis anisotropy. The tilt can occur when $\vec{d}$ points in the hard-axis direction. In neuromorphic systems, this effect becomes consequential for spike propagation by either easing or staggering spiking of biaxial neurons. This section aims to explain how this effect occurs.

In order to understand DMI caused spike easing or staggering properly, imagine that the LLG equation takes on the following effective field,

$$\vec{H}_i = H_h\hat{y} - H_e\hat{x} \pm \vec{d} \times m_i. \tag{7.19}$$

Where $\vec{d}$ is the homogeneous DMI vector containing its strength and direction, and $H_h \gg H_e$. The term differs in sign in the A and B sublattice. The system has a hard axis anisotropy H_h in the $\hat{y}$ direction and an easy axis H_e in the $\hat{x}$ direction. The exchange energy is not included at this point. Given the effective field in equation 7.19 the ground state is in the x direction with some correction due to DMI. In addition, there is an incident torque τ polarized along the y axis. As before, the torque term is

$$\tau\vec{m}_i \times \vec{m}_i \times \hat{p} \tag{7.20}$$

where the torque strength is τ and $\hat{p}$ the direction of polarization in the heavy metal layer. Given the angular variables introduced in equation 6.5 and assuming that the system is close to good ferromagnetic ordering, i.e. $\vec{m}_B \sim -\vec{m}_A$, the term in equation 7.20 becomes

$$\begin{aligned}\tau\dot{\vec{m}}_i \times \dot{\vec{m}}_i \times \hat{y} &= \tau\cos\phi\cos\epsilon\sin\epsilon\hat{x} - \tau(\sin^2\phi\cos^2\epsilon + \cos^2\phi\cos^2\epsilon)\hat{y} + \tau\sin\phi\cos\epsilon\sin\epsilon\hat{z} \\ &= \tau\cos\phi\epsilon\hat{x} - \tau\hat{y} + \tau\sin\phi\epsilon\hat{z},\end{aligned} \tag{7.21}$$

for both sublattices A and B. In the last line of equation 7.21, a small deviation from the ground state in ϵ is assumed, as the hard axis is dominating the free energy. Doing a similar derivation for the DMI contribution to the derivative $\dot{\vec{m}}_i$ yields to the dominating factor

$$\vec{m}_i \times \vec{H}_{DMI} = d_y\cos\phi\epsilon\hat{x} - d_y\hat{y} + d_y\sin\phi\epsilon\hat{z}. \tag{7.22}$$

Where the term $\alpha\vec{m}_i \times \vec{m}_i \times \vec{H}_{DMI}$ is presumed small and the DMI vector $\vec{d}$ is assumed to be along the y axis, $\vec{d} = (0, d_y, 0)$, as in Hematite. As seen from equation 7.21 the parameter ϵ enters the torque contribution to the local magnetization in the x and z directions. The torque form also appears in equation 7.22, when $\vec{d} \parallel \hat{y}$. The DMI vector effects spiking through two derivative contributions. Firstly it tilts the magnetization vectors $\vec{m}_A$ and $\vec{m}_B$ with some small angle ϵ, and secondly, the interaction gives a precessional motion through its contributions in $\hat{x}$ and $\hat{z}$. If $d_y > 0$, this contribution eases spiking since it tilts the Néel vector in the same direction as the input current, which increases the precessional contributions from the torque, and lowers the current threshold in the system. If $d_y < 0$, the opposite happens. The Néel vector is made to tilt oppositely to the incoming torque and thus increases the spiking threshold.

This is also verified in simulations in figure 7.6 where the threshold current with and without DMI is investigated.

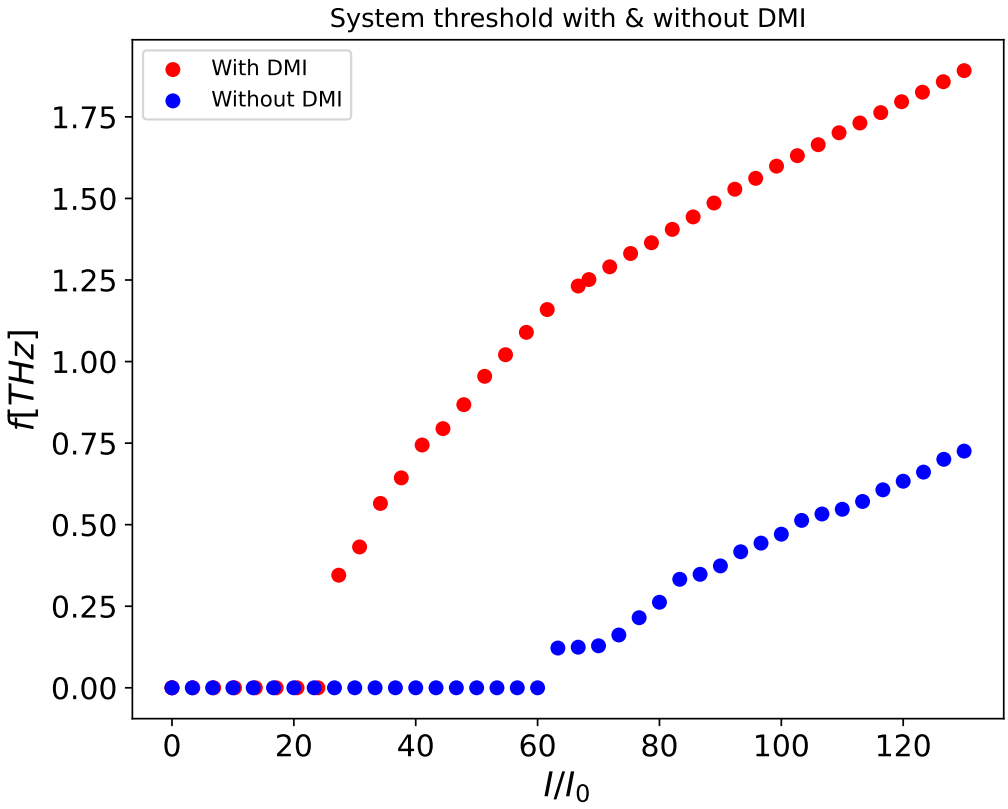

Figure 7.6: The figure shows the threshold currents of two systems with the same parameters, except for the DMI vector $\vec{d}$, which is set to zero in one case. The characteristic frequency is plotted along the y axis and is calculated through a Fourier transform.

As seen in figure 7.6 the spike propagation is severely altered when there is DMI present in the material. As mentioned, the DMI ensures a small magnetization by tilting the vectors $\vec{m}_A$ and $\vec{m}_B$. Therefore, tuning the system by either a magnetic field or an opposing current in the synaptic region might be possible. A magnetic field can effectively "kill" this magnetization, while an opposing (with $\hat{p} = -\hat{y}$) can cause the opposite tilt of the DMI vector and alter the spike propagation. Therefore the next step is to investigate what happens under magnetic field perutrbation.

7.10 Magnetic field perturbation

To see the effects of magnetic field perturbation, the same structure as in figure 7.3 was used. The magnetic field was made to vary with negative and positive values in the x, y and z directions. One simulation run was completed at that direction and strength when

keeping all other parameters equal. The effects of injecting a magnetic field in both the first neuron, synaptic region, the second neuron and the structure as a whole was investigated. It is unsure if it is feasible to inject narrow enough fields experimentally to only effect a single neuron or synapse. Therefore the whole structure was investigated as an alternative.

7.10.1 Easy-plane magnetic field perturbation

When magnetic fields are injected within the easy plane, the effect forms a hard-axis anisotropic effect. When the magnetic field is in the z direction, where no anisotropies are present, it simply "injects" a hard axis along this direction and cancels spike propagation. This happens both when perturbing the second synaptic region and the synaptic region. The resulting signal is shown in figure

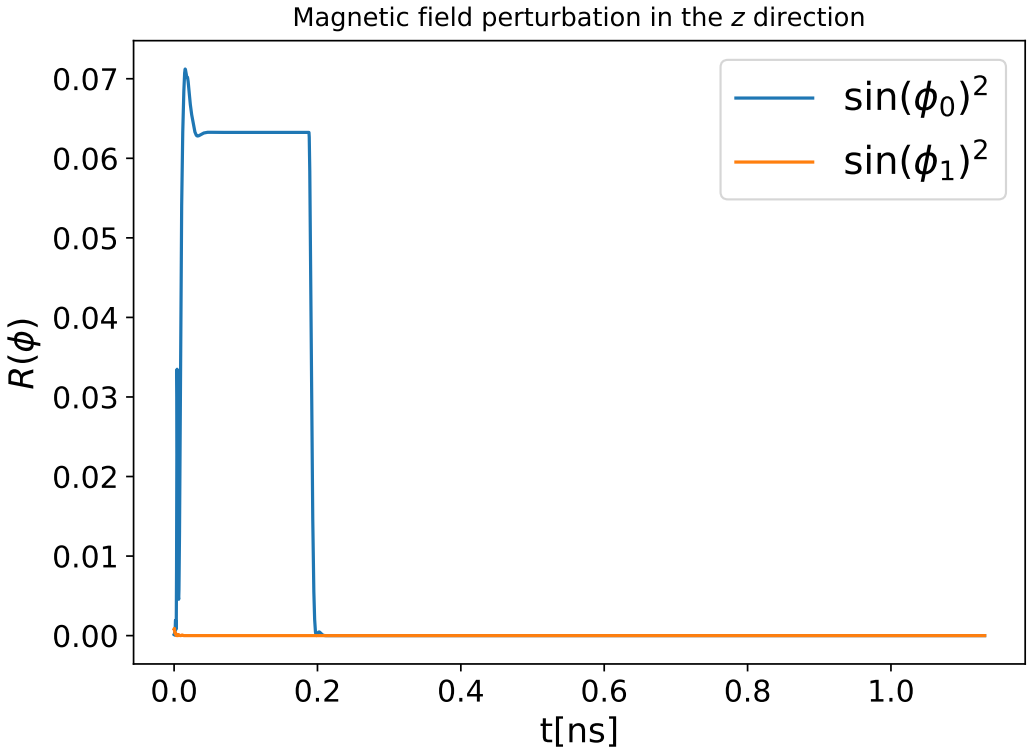

Figure 7.7: As seen in the figure when perturbing the system with a magnetic field in the z-direction, it simply cancels spike propagation in both neurons. The magnetic field is here induced in the entirety of the system, but the effect holds for perturbing only the first or second neuron.

The other alternative when injecting a magnetic field within the easy plane is in the x direction. The effect differs from that of the z direction by easing spike propagation. This

makes sense as a magnetic field in the x direction induces a hard-axis-like anisotropic effect. This essentially normalizes the easy-axis anisotropic constant. This is within a certain limit, namely the spin-flop limit. Above that limit, the magnetic field overcomes the easy-axis anisotropy and creates an effective hard-axis along x. This causes spike propagation to cancel. When injecting a field close to the spin-flop limit, the system can be made to spike several times at the same input current. This effect is shown in figure 7.8.

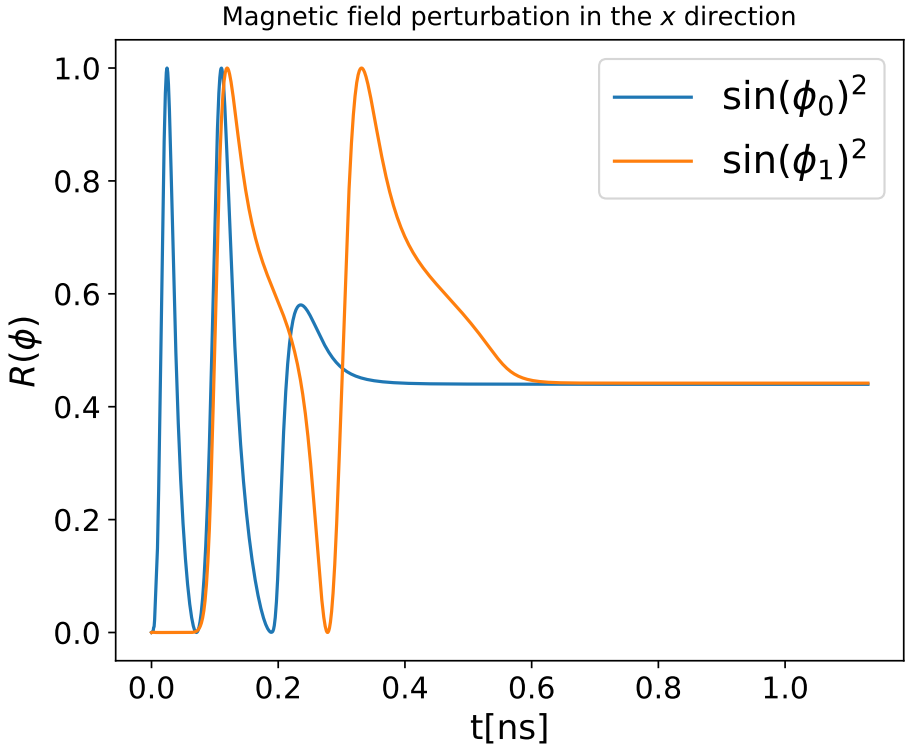

Figure 7.8: The figure shows that perturbing the structure with a magnetic field in the x direction. By tuning the system with a x direction field, multiple spikes can be produced for the same magnetic field.

7.10.2 Hard-axis magnetic field perturbation

Along the hard axis, the magnetic effect differs slightly. As usual, for large enough fields, it simply cancels spike propagation by dominating the free energy completely. The results for lower fields have however proven to be inconclusive as of now. There seems to be some modification to wave propagation speed, although the reasoning for this is unknown. It does not seem to hinder spike propagation significantly.

For fields five times larger the magnetic field cancellation strength in figure 7.7 along the

hard axis is able to cancel spike propagation. Given that the DMI interaction gives a small magnetization along the y axis, a magnetic field cancelling this magnetization seem able to cancel the propagation. This is sensible as it is essentially removing the DMI contribution to the spiking threshold.

7.11 Biological bursting

As mentioned in section 3 neurons are known to be able to burst. A burst in this context is a series of spikes from a single input at once. This effect is possible to arrive at in artificial neurons as well. The whole system enters an auto-oscillation regime by biasing the synaptic region with a close-to threshold and sending a regular spike current to the first neuron.

This is because when a close-to threshold current is present in the synaptic region, a small perturbation is needed to induce rotation, analogous to the macro spin approximation (equation 6.23). This means that when the rotation is initiated, it easily arrives at an auto oscillation regime. This result is shown in figure 7.9.

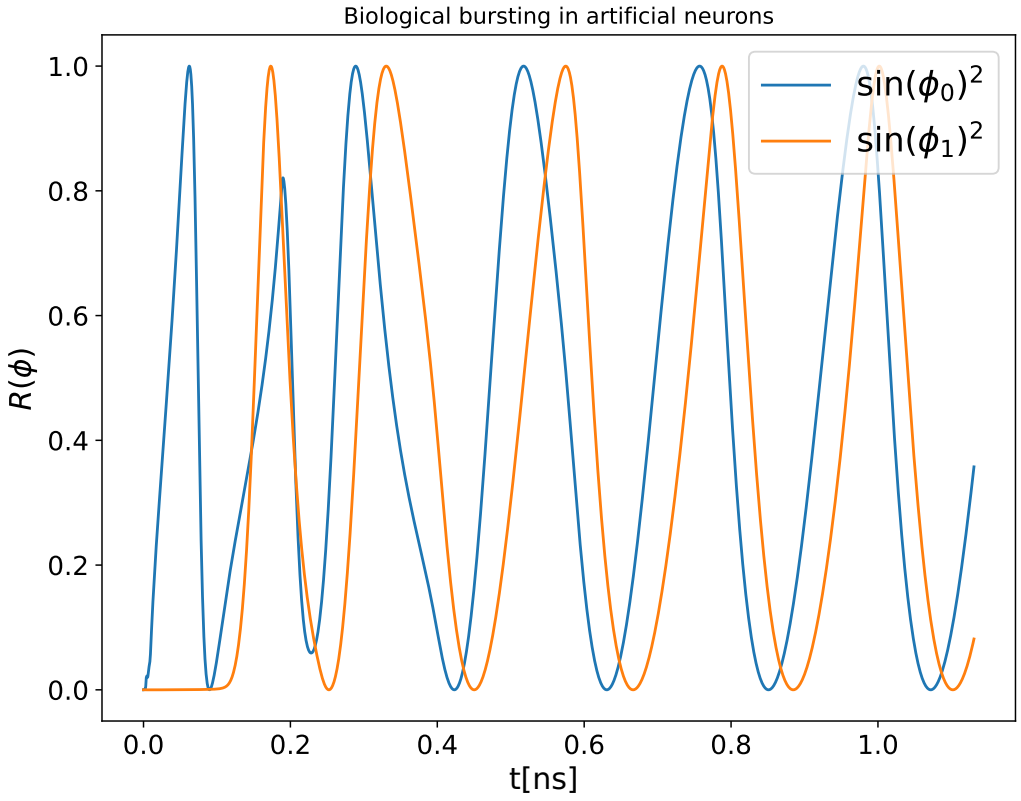

Figure 7.9: The figure shows an artificial antiferromagnetic bursting when the synaptic region is biased with a less than threshold current. ϕ_0 denotes the input neuron phase angle, and ϕ_1 the output neuron phase angle.

As seen in figure 7.9 the bursting of the two neurons is initiated after the first rotation of the input neuron(ϕ_0).

Although the system shows to be burstable, the bursting itself causes the input neuron to continue rotating as well. This, of course, causes problems for new incoming signals. The rotations do die out when the background current is turned off. Therefore, some method of limiting the signal propagation backwards might need to be implemented for this to work efficiently. Alternatively, to make a bursting system, one could perturb the system by a magnetic field at the flop transition, effectively removing the easy axis barrier.

8 Conclusion and Outlook

8.1 Conclusion

In this thesis, the theoretical background of antiferromagnetic neuromorphic systems was presented. Two concepts of neuromorphic computing with antiferromagnetic components were investigated from a theoretical and numerical standpoint. It was found that topological charges can be utilized as charge carriers in neuromorphic systems, where spike propagation is envisioned as phase transitions in one domain antiferromagnets. Secondly, an antiferromagnetic neuromorphic system was assessed from a previously found system in ferromagnets. It was found that this system incorporates the most important effects of the ferromagnetic counterpart numerically. In addition, the addition of homogeneous Dzyaloshinskii-Moriya interaction(DMI) was found to ease or stagger spike propagation in neuromorphic systems. The effects of perturbing the antiferromagnetic systems with magnetic fields were also examined.

Previous works have found that antiferromagnets can mimic spiking behaviour in superconducting Josephson junctions, a known candidate for neuromorphic computation. In this thesis, antiferromagnets are arranged as network components in nanoconstrictions. Further, these exhibit critical properties of neuromorphic systems vital for usage in spiking neural networks.

When injecting a spin-torque into the antiferromagnetic nanoconstriction, the threshold for spike propagation seems to be dependent on the presence of DMI when the homogeneous DMI vector $\vec{d}$ is parallel to the hard-axis anisotropy. This effect is believed to arise from tilting the order parameter towards the hard axis. It is shown that the input torque produces a similar tilt and a rotational contribution dependent on the amount of tilt present.

This project investigated antiferromagnetic usage in neuromorphic systems, a rapidly rising and essential field in a world where power usage of computation becomes increasingly important to tame. The thesis builds on already established concepts to arrive at conventional spintronic components.

As stated in the introduction, the end of Moore's law is nearing, and computational efficiency needs to be found elsewhere than cramming more semiconductors into chips. Antiferromagnetic spintronics and neuromorphic computing can be the answer for a faster and cleaner source of computation.

8.2 Outlook

The next step to build further on this thesis is to look at the components' temperature stability, see if they can be utilized in a more extensive network and find suitable materials for eventual production.

For a network to build on the concepts presented here, it is essential that the same dynamics can be found at finite temperatures. Finite temperature enters the equations of motion as a random Gaussian field and is believed not to cause an issue as long as there is good antiferromagnetic ordering in the material, however noise might cause some modifications to the signal propagation. The choice of material, therefore, becomes very important, as different materials exhibit different Néel temperatures(where antiferromagnetic ordering breaks down). Hematite is believed to possibly work as such a material, as the Néel temperature is high and the Hamiltonian is similar to the one used in this thesis. It remains actually to test for real Hematite systems.

In addition, it would be interesting to see how a network of these components performs on a data set. If these components are to be built, the predictability and power consumption must be small enough to compete with conventional networks. These numbers have not been tested here.

The results of this thesis are also to be made into a paper in the fall of 2022. The excact time and publication place is not yet determined.

References

[1] G. Moore, «Cramming more components onto integrated circuits, Reprinted from Electronics, volume 38, number 8, April 19, 1965, pp.114 ff», Solid-State Circuits Newsletter, IEEE **11**, 33–35 (2006) (cited on page 9).

[2] L. Néel, «Magnetism and Local Molecular Field», Science **174**, 985–992 (1971) (cited on page 9).

[3] M. B. Jungfleisch, W. Zhang, and A. Hoffmann, «Perspectives of antiferromagnetic spintronics», Physics Letters A **382**, 865–871 (2018) (cited on page 9).

[4] S. M. Rezende, A. Azevedo, and R. L. Rodríguez-Suárez, «Introduction to antiferromagnetic magnons», **126**, 151101 (2019) (cited on page 9).

[5] T. Kampfrath, A. Sell, G. Klatt, A. Pashkin, S. Mährlein, T. Dekorsy, M. Wolf, M. Fiebig, A. Leitenstorfer, and R. Huber, «Coherent terahertz control of antiferromagnetic spin waves», **5**, 31–34 (2010) (cited on page 9).

[6] L. Néel, «Antiferromagnetism and Ferrimagnetism», **65**, 869–885 (1952) (cited on page 13).

[7] P. Hemmer, *Kvantemekanikk* (Tapir akademisk forlag, 2005) (cited on pages 13–15, 18, 23).

[8] D. J. Griffiths, *Introduction to Electrodynamics*, 3rd edition (Prentice Hall, 1999) (cited on pages 15–16).

[9] M. Getzlaff, *Fundamentals of Magnetism* (Springer, 2008) (cited on page 16).

[10] P. W. Anderson, «Antiferromagnetism. Theory of Superexchange Interaction», Phys. Rev. **79**, 350–356 (1950) (cited on page 17).

[11] T. Moriya, «Anisotropic Superexchange Interaction and Weak Ferromagnetism», Phys. Rev. **120**, 91–98 (1960) (cited on page 17).

[12] J. Slonczewski, «Current-driven excitation of magnetic multilayers», Journal of Magnetism and Magnetic Materials **159**, L1–L7 (1996) (cited on pages 18–19).

[13] S. Zhang, P. M. Levy, and A. Fert, «Mechanisms of Spin-Polarized Current-Driven Magnetization Switching», Phys. Rev. Lett. **88**, 236601 (2002) (cited on page 18).

[14] Z. Xiao, X. Ma, P. Wu, J. Zhang, L. Chen, and S. Shi, «Micromagnetic simulations of current-induced magnetization switching in Co/ Cu/ Co nanopillars», Journal of Applied Physics **102**, 10.1063/1.2800999 (2007) (cited on page 19).

[15] E. G. Tveten, T. Müller, J. Linder, and A. Brataas, «Intrinsic magnetization of antiferromagnetic textures», Phys. Rev. B **93**, 104408 (2016) (cited on page 20).

[16] L. A. Kristiansen, «Spin-orbit-induced dynamics of magnetic textures», Master's thesis (Norwegian University of Science and Technology, Institute for Physics, 2017) (cited on page 21).

[17] T. L. Gilbert, «A phenomenological theory of damping in ferromagnetic materials», IEEE Transactions on Magnetics **40**, 3443–3449 (2004) (cited on page 24).

[18] E. Aksnes Tønseth, V. Uthayamoorthy, and A. Qaiumzadeh, *Antiferromagnetic-spin-simulations*, `https://github.com/evenat684/Antiferromagnetic-spin-simulations`, version 1.0.0, May 2022 (cited on pages 26, 88).

[19] S. Dasgupta and J. Zou, «Zeeman term for the Néel vector in a two sublattice antiferromagnet», Physical Review B **104** (2021) (cited on page 27).

[20] E. G. Tveten, «Manipulating Spins in Antiferromagnets with External Forces», PhD thesis (Norwegian University of Science and Technology, Institute for Physics, 2016) (cited on page 29).

[21] M. d'Aquino, C. Serpico, G. Coppola, I. Mayergoyz, and G. Bertotti, «Midpoint numerical technique for stochastic Landau-Lifshitz-Gilbert dynamics», Journal of Applied Physics **99**, 08B905–08B905 (2006) (cited on page 30).

[22] S. Ament, N. Rangarajan, A. Parthasarathy, and S. Rakheja, *Solving the stochastic Landau-Lifshitz-Gilbert-Slonczewski equation for monodomain nanomagnets : A survey and analysis of numerical techniques*, 2016 (cited on pages 30–31, 65).

[23] W. F. Brown, «Thermal Fluctuations of a Single-Domain Particle», Phys. Rev. **130**, 1677–1686 (1963) (cited on pages 30–31).

[24] R. Kubo and N. Hashitsume, «Brownian Motion of Spins», Progress of Theoretical Physics Supplement **46**, 210–220 (1970) (cited on page 31).

[25] Ivanov, Kosevich, and Kovalev, «Magnetic Solitons», Physics Reports **194**, 117–238 (1990) (cited on pages 33, 52).

[26] H.-B. Braun, «Topological effects in nanomagnetism: from superparamagnetism to chiral quantum solitons», Advances in Physics **61**, 1–116 (2012) (cited on pages 34–35).

[27] D. J. Thouless, *Introduction to Topological Quantum Numbers*, edited by A. Comtet, T. Jolicœur, S. Ouvry, and F. David (Springer Berlin Heidelberg, 1999), pages 767–841 (cited on page 34).

[28] A. S. Schwarz, *Topology for Physicists* (Springer Berlin Heidelberg, 1994) (cited on pages 34, 36).

[29] C. von Westenholz, «Topological and Noether-conservation laws», eng, Annales de l'I.H.P. Physique théorique **30**, 353–367 (1979) (cited on page 35).

[30] D. Marković, A. Mizrahi, D. Querlioz, and J. Grollier, «Physics for neuromorphic computing», Nat. Rev. Phys. **2**, 499–510 (2020) (cited on page 37).

[31] J. von Neumann, «First draft of a report on the EDVAC», IEEE Annals of the History of Computing **15**, 27–75 (1993) (cited on page 37).

[32] C. D. Schuman, S. R. Kulkarni, M. Parsa, J. P. Mitchell, P. Date, and B. Kay, «Opportunities for neuromorphic computing algorithms and applications», Nature Computational Science **2**, 10–19 (2022) (cited on page 37).

[33] S. Furber, «Large-scale neuromorphic computing systems», Journal of Neural Engineering **13** (2016) (cited on page 38).

[34] C. Mayr, S. Hoeppner, and S. Furber, «SpiNNaker 2: A 10 Million Core Processor System for Brain Simulation and Machine Learning», `10.48550/ARXIV.1911.02385` (2019) (cited on page 39).

[35] M. Davies, N. Srinivasa, T.-H. Lin, G. Chinya, Y. Cao, S. H. Choday, G. Dimou, P. Joshi, N. Imam, S. Jain, Y. Liao, C.-K. Lin, A. Lines, R. Liu, D. Mathaikutty, S. McCoy, A. Paul, J. Tse, G. Venkataramanan, Y.-H. Weng, A. Wild, Y. Yang, and H. Wang, «Loihi: A Neuromorphic Manycore Processor with On-Chip Learning», IEEE Micro **38**, 82–99 (2018) (cited on page 39).

[36] W. Gerstner, W. M. Kistler, R. Naud, and L. Paninski, *Neuronal Dynamics* (Cambridge University Press, 2014) (cited on page 40).

[37] D. O. Hebb, *The organization of behavior: A neuropsychological theory* (Wiley, 1949) (cited on pages 41, 45).

[38] H. Jang, O. Simeone, B. Gardner, and A. Gruning, «An Introduction to Probabilistic Spiking Neural Networks: Probabilistic Models, Learning Rules, and Applications», IEEE Signal Processing Magazine **36**, 64–77 (2019) (cited on page 43).

[39] J. Sjöström and W. Gerstner, «Spike-timing dependent plasticity», Scholarpedia **5**, 1362 (2010) (cited on page 45).

[40] S. Zhang and Y. Tserkovnyak, «Antiferromagnet-Based Neuromorphics Using Dynamics of Topological Charges», Phys. Rev. Lett. **125**, 207202 (2020) (cited on pages 47, 53, 55–56, 58, 60, 62, 64, 74–75).

[41] A. Kurenkov, S. Duttagupta, C. Zhang, S. Fukami, Y. Horio, and H. Ohno, «Artificial Neuron and Synapse Realized in an Antiferromagnet/Ferromagnet Heterostructure Using Dynamics of Spin–Orbit Torque Switching», Advanced Materials **31** (2019) (cited on pages 47, 58).

[42] Y. Tserkovnyak and J. Xiao, «Energy Storage via Topological Spin Textures», Physical Review Letters **121** (2018) (cited on page 53).

[43] D. Hill, S. K. Kim, and Y. Tserkovnyak, «Spin-Torque-Biased Magnetic Strip: Nonequilibrium Phase Diagram and Relation to Long Josephson Junctions», Phys. Rev. Lett. **121**, 037202 (2018) (cited on page 54).

[44] S. Takei and Y. Tserkovnyak, «Superfluid Spin Transport Through Easy-Plane Ferromagnetic Insulators», Phys. Rev. Lett. **112**, 227201 (2014) (cited on page 54).

[45] X. Zhou, Z. Zhang, and C.-Z. Hu, «Spin continuity equation and definition of spin current», (2009) (cited on page 54).

[46] M. Schiulaz, E. J. Torres-Herrera, and L. F. Santos, «Thouless and relaxation time scales in many-body quantum systems», Phys. Rev. B **99**, 174313 (2019) (cited on page 56).

[47] L. Mondaini, «The Rise of Solitons in Sine-Gordon Field Theory: From Jacobi Amplitude to Gudermannian Function», Journal of Applied Mathematics and Physics **02**, 1202–1206 (2014) (cited on page 59).

[48] R. Khoshlahni, A. Qaiumzadeh, A. Bergman, and A. Brataas, «Ultrafast generation and dynamics of isolated skyrmions in antiferromagnetic insulators», Physical Review B **99** (2019) (cited on page 65).

[49] S. K. Kim and Y. Tserkovnyak, «Landau-Lifshitz theory of thermomagnonic torque», Phys. Rev. B **92**, 020410 (2015) (cited on pages 68–69).

[50] D. Marković, M. W. Daniels, P. Sethi, A. D. Kent, M. D. Stiles, and J. Grollier, «Easy-plane spin Hall nano-oscillators as spiking neurons for neuromorphic computing», Physical Review B **105** (2022) (cited on pages 73–74, 78–79, 81, 83–87).

[51] P. Crotty, D. Schult, and K. Segall, «Josephson junction simulation of neurons», Phys. Rev. E **82**, 011914 (2010) (cited on page 73).

[52] M. Schneider, E. Toomey, G. Rowlands, J. Shainline, P. Tschirhart, and K. Segall, «SuperMind: a survey of the potential of superconducting electronics for neuromorphic computing», Superconductor Science and Technology **35**, 053001 (2022) (cited on page 73).

[53] R. Khymyn, I. Lisenkov, V. Tiberkevich, B. A. Ivanov, and A. Slavin, «Antiferromagnetic THz-frequency Josephson-like Oscillator Driven by Spin Current», Scientific Reports **7**, 43705 (2017) (cited on page 73).

[54] Y. Liu, I. Barsukov, Y. Barlas, I. N. Krivorotov, and R. K. Lake, «Synthetic antiferromagnet-based spin Josephson oscillator», Applied Physics Letters **116**, 132409 (2020) (cited on page 73).

[55] P. Evans, «Rotations and rotation matrices», Acta crystallographica. Section D, Biological crystallography **57**, 1355–9 (2001) (cited on page 76).

[56] W. Legrand, D. Maccariello, F. Ajejas, S. Collin, A. Vecchiola, K. Bouzehouane, N. Reyren, V. Cros, and A. Fert, «Room-temperature stabilization of antiferromagnetic skyrmions in synthetic antiferromagnets», Nature Materials **19**, 34–42 (2020) (cited on page 83).

[57] A. H. Morrish, *Canted Antiferromagnetism: Hematite* (WORLD SCIENTIFIC, Jan. 1995) (cited on page 83).

[58] M. Śl ęzak, H. Nayyef, P. Dró żd ż, W. Janus, A. Kozioł-Rachwał, M. Szpytma, M. Zając, T. O. Mente ş, F. Genuzio, A. Locatelli, and T. Śl ęzak, «Controllable magnetic anisotropy and spin orientation of a prototypical easy-plane antiferromagnet on a ferromagnetic support», Phys. Rev. B **104**, 134434 (2021) (cited on page 84).

[59] M. Zahedinejad, H. Fulara, R. Khymyn, A. Houshang, M. Dvornik, S. Fukami, S. Kanai, H. Ohno, and J. Åkerman, «Memristive control of mutual spin Hall nano-oscillator synchronization for neuromorphic computing», Nature Materials **21**, 81–87 (2021) (cited on page 84).

[60] S. Jiang, R. Khymyn, S. Chung, T. Le, L. Diez, A. Houshang, M. Zahedinejad, D. Ravelosona Ramasitera, and J. Åkerman, «Reduced spin torque nano-oscillator linewidth using He + irradiation», Applied Physics Letters **116**, 072403 (2020) (cited on page 84).

[61] H. Kurt, D. M. Venkatesan, and J. M. D. Coey, «Enhanced perpendicular magnetic anisotropy in Co/Ni multilayers with a thin seed layer», Journal of Applied Physics **108**, 073916–073916 (2010) (cited on page 84).

Even Aksnes Tønseth

Antiferromagnetic Neuromorphic Computing

NTNU
Norwegian University of
Science and Technology